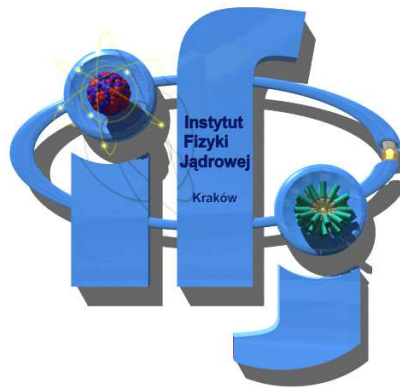


Hydrodynamic description of particle production in relativistic heavy-ion collisions

Mikołaj Chojnacki

The Henryk Niewodniczański
Institute of Nuclear Physics
Polish Academy of Sciences
Kraków, Poland



*Thesis submitted for the Degree of Doctor of Philosophy in Physics
Prepared under the supervision of Prof. Wojciech Florkowski*

Kraków, March 2009

STRESZCZENIE

Niniejsza praca prezentuje nowo opracowany model ewolucji hydrodynamicznej, który w połączeniu z modelem statystycznej hadronizacji **THERMINATOR** służy nam do opisu zachowania silnie oddziałującej materii wyprodukowanej w relatywistycznych zderzeniach ciężkich jonów. Nasze oryginalne podejście wykorzystano do wykonania dopasowań dla danych pochodzących z eksperymentów realizowanych na akceleratorze RHIC (Relativistic Heavy Ion Collider w Brookhaven National Laboratory) przy najwyższej jego energii $\sqrt{s_{NN}} = 200$ GeV, oraz do sformułowania przewidywań teoretycznych dla przyszłych eksperymentów ciężkojonowych przy wyższych energiach ($\sqrt{s_{NN}} = 5.5$ TeV, dla akceleratora LHC, skrót od Large Hadron Collider w CERN-ie).

Nasze wyniki odnoszą się do obserwabli jedno- i dwu-cząstkowych w zakresie miękkiej fizyki ($p_T \leq 2$ GeV). Opisujemy widma cząstek w pędzie poprzecznym, współczynnik przepływu eliptycznego v_2 , oraz promienie HBT dla identycznych pionów (HBT jest skrótem od nazwisk Hanbury-Brown i Twiss). W ramach prac nad rozprawą skonstruowaliśmy nowe równanie stanu dla materii silnie oddziałującej, które łączy model gazu hadronowego z wynikami symulacji QCD na siatkach. Całość programów tworzy platformę obliczeniową w skład której wchodzi kod hydrodynamiczny połączony z modelem statystycznej hadronizacji **THERMINATOR** (skrót od THERMal heavy IoN generATOR).

Stosując standardowy model optyczny Glaubera jako warunek początkowy dla ewolucji hydrodynamicznej, osiągnęliśmy bardzo dobry opis danych eksperymentalnych uzyskanych na akceleratorze RHIC. W szczególności osiągnęliśmy znacznie lepszy, od wcześniej uzyskanych w modelach hydrodynamicznych, opis promieni korelacyjnych. Dla przyszłych eksperymentów ciężkojonowych na LHC uzyskaliśmy przewidywania teoretyczne dotyczące miękkich obserwabli.

Zaproponowaliśmy również sposób rozwiązania tzw. zagadki HBT na RHIC-u. Sugerujemy zmodyfikowanie warunków początkowych i wprowadzenie Gaussowskiego profilu gęstości materii jako warunku początkowego dla hydrodynamiki. Taka modyfikacja prowadzi do szybszej formacji poprzecznego przepływu kolektywnego, co warunkuje uzyskanie wyjątkowo dobrej zgodności naszego modelu z danymi eksperymentalnymi.

Jako ostatni punkt, wprowadziliśmy do naszego modelu proces swobodnego strumieniowania cząstek, który w połączeniu z mechanizmem nagłej, chociaż opóźnionej w czasie termalizacji, tworzy nowe warunki początkowe dla kodu hydrodynamicznego. Wprowadzenie przedrównowagowej ewolucji pozwoliło nam na opóźnienie startu fazy hydrodynamicznej. Jest to pożądaný efekt, który ma na celu uniknięcie założenia o bardzo wczesnej termalizacji układu, które wydaje się bardzo trudne do uzasadnienia na gruncie mikroskopowym. Podkreśliśmy, iż włączenie swobodnego strumieniowania cząstek nie zmienia wysokiej zgodności uzyskanych wyników modelowych z danymi doświadczalnymi.

*I know that this defies the law of gravity,
but, you see, I never studied law.*

– Bugs Bunny

*Physics isn't a religion.
If it were, we'd have a much easier time raising money.*

– Leon Lederman

— *to my Parents* —

Acknowledgments

I would like to express my deepest thanks to my supervisor Prof. Wojciech Florkowski for his invaluable help, guidance and patience during the course of this Thesis. Furthermore I wish to thank Wojciech Broniowski, Adam Kisiel and Piotr Bożek for a chance of working with them and being part of the team and to everybody in the Department of Theory of Structure of Matter (NZ41).

I am very grateful to all of my family and friends for their support throughout my journey into obtaining this Degree. I thank you all.

Research was supported by the Polish Ministry of Science and Higher Education grant N202 153 32/4247 (2007-2009).

Contents

1	Introduction	11
2	Relativistic thermodynamics	17
2.1	Hadron gas	19
2.1.1	Pion gas	20
2.1.2	Classical gas	21
2.1.3	Massive hadron gas	21
2.2	Quark-Gluon Plasma	22
2.3	Modeling the crossover phase transition	23
3	Relativistic hydrodynamics of perfect fluid	27
3.1	Hydrodynamic equations for baryon free matter	27
3.2	Implementation of boost-invariance	29
3.3	Characteristic form of hydrodynamic equations	30
3.4	Boundary conditions	31
4	Initial conditions	35
4.1	Standard initial conditions	35
4.2	Gaussian initial conditions	37
4.3	Free streaming	38
5	Freeze-out prescription	43
5.1	Cooper-Frye formula	43
5.2	Calculation of observables	46
6	Soft-hadronic observables at RHIC	49
6.1	Central collisions	49
6.2	Non-central collisions	52
7	Predictions for LHC	55
7.1	Central collisions	56
7.2	Non-central collisions	58

8	Uniform description of the RHIC data	61
8.1	Early start of hydrodynamics	61
8.2	Hydrodynamics preceded by free-streaming	64
9	Summary	69
A	Relativistic thermodynamics of perfect gases	71
A.1	Grand canonical potential Ω	71
A.1.1	The grand canonical partition function	72
A.1.2	Quantum statistics	72
A.1.3	Boltzmann classical limit	73
A.1.4	Massive particles	73
A.1.5	Massless particles	74
A.1.6	Vanishing chemical potential	75
A.2	Other thermodynamic variables	76
B	Properties of hydrodynamic equations	79
B.1	Basic definitions	79
B.2	Covariant form	80
B.3	Non-covariant form	80
B.4	Temperature equation	81
B.4.1	Boost-invariance	83
B.4.2	Cylindrical symmetry	84
B.5	Entropy equation	84
B.5.1	Boost-invariance	84
B.5.2	Cylindrical symmetry	85
C	Notation	87
D	Mathematical supplement	89
D.1	Modified Bessel functions	89

Chapter 1

Introduction

Nowadays, the relativistic hydrodynamics is regarded as the best theoretical framework for description of the spacetime evolution of strongly interacting matter produced in ultra-relativistic heavy-ion collisions [1, 2, 3, 4, 5, 6, 7, 8, 9, 10, 11, 12, 13, 14, 15, 16, 17, 18, 19, 20, 20, 21, 22, 23, 24] , for a recent review see [25]. In particular, the soft hadronic one-particle data describing the transverse-momentum spectra and the elliptic flow coefficient v_2 , collected in the RHIC experiments (Relativistic Heavy-Ion Collider at the Brookhaven National Laboratory), have been successfully explained in various approaches based on the perfect-fluid hydrodynamics. In fact, the explanation of the large value of the elliptic flow by perfect hydrodynamics is regarded as the evidence of early thermalization and suggests that the quark-gluon plasma created at RHIC is a strongly interacting system [26].

On the other hand, the approaches based on the hydrodynamics cannot reproduce the two-particle observables such as the pion correlation radii. The latter are commonly called the HBT radii – after Hanbury-Brown and Twiss who in 1950s showed that it was possible to determine the angular sizes of astronomical radio sources and stars from the correlations of signal intensities, rather than amplitudes. The difficulty of the consistent description of the one- and two-particle observables picked up the name "HBT puzzle". The HBT puzzle and the problem of the microscopic explanation of very fast thermalization of the matter produced at RHIC represent two issues that challenge the hydrodynamic picture.

In this Thesis we present our recently developed hydrodynamic model and use it to describe the RHIC data. We address both the one- and two-particle observables: the transverse momentum spectra, the elliptic flow coefficient v_2 , and the pion HBT radii. We suggest how the HBT puzzle as well as the early thermalization problem may be solved. Similarly to other approaches, our model is based on the perfect fluid hydrodynamics and includes the symmetry against Lorentz boosts along the beam axis, the so called boost-invariance. This restriction means that our results may be applied only to the central regions of relativistic heavy-ion collisions. On the other hand, our framework differs from other approaches in several important aspects, in particular, in the use of a different equation of state, modification of the initial conditions, two-body method of the calculation of the correlation functions,

and different treatment of the final hadronic stage. The main achievements of the Thesis are the following:

1. *The construction of the realistic equation of state for strongly interacting matter which interpolates between the hadron gas model and the results of the QCD lattice simulations.* This equation of state describes the crossover phase transition, i.e., the transition where thermodynamic variables such as energy density or entropy density change very rapidly in the narrow range of the temperature, however, no real discontinuities in the behavior of the thermodynamic variables are present. Noticeably, our equation of state has no pronounced soft point where the sound velocity is very small and possibly drops to zero. It is known that the presence of such a soft point leads to the ratio of the HBT radii $R_{\text{out}}/R_{\text{side}}$ that is larger than unity – an effect which has not been confirmed by the experimental data.
2. *The boost-invariant hydrodynamic equations for baryon free matter have been rewritten in the very concise form which reduces the number of the independent equations to two.* This may be done in the formal way if the range of the variable r (the distance from the collision axis) is extended to the negative values. The applied procedure is a direct generalization of the formalism introduced earlier by Baym et al. in the studies of cylindrically symmetric systems with constant sound velocity. The new form of the hydrodynamic equations allows for the simple and natural inclusion of the boundary conditions at the origin of the system.
3. *The computational platform has been constructed which combines the hydrodynamic code with the statistical hadronization model THERMINATOR[27].* This is arranged in such a way that the information about the freeze-out hypersurface obtained from the hydrodynamic code is exported and treated as an input for THERMINATOR. We emphasize that our equation of state (in the region below the critical temperature $T_c \sim 170$ MeV) describes the hadron gas with the same set of the hadronic species as that included in THERMINATOR. Hence, there is a smooth change between the hydrodynamic and statistical description of the produced matter. THERMINATOR is a Monte Carlo program simulating the decays of resonances. The Monte-Carlo method allows for the direct comparison of our model results with the experimental data. In particular, one can easily include various experimental cuts.
4. *The successful description of the soft hadronic RHIC data has been achieved with the standard initial conditions obtained from the optical limit of the Glauber model.* By this we mean here that the use of the new equation of state helped to reduce the discrepancy between the theoretical and experimental ratio of the HBT radii R_{out} and R_{side} . In this version of our calculations we find $R_{\text{out}}/R_{\text{side}} \sim 1.25$, significantly closer to the experimental values than in earlier hydrodynamic studies.

5. *Predictions for the future heavy-ion collisions at LHC have been formulated.* In the studied by us central region we expect that the transition from the RHIC energy, $\sqrt{s_{NN}} = 200$ GeV, to the LHC energy, $\sqrt{s_{NN}} = 5.5$ TeV, results essentially in a higher initial central temperature T_i used as the input for the hydrodynamic calculation. Thus, one can make predictions for the collisions at the LHC energies using a set of values for T_i which are higher than those used at RHIC. At RHIC we found $T_i = 320$ MeV, hence for LHC we studied the cases $T_i = 400, 450,$ and 500 MeV. Our results for LHC indicate a moderate increase of the HBT radii and saturation of the pion elliptic flow (as compared to the RHIC experiments).
6. *The solution of the RHIC HBT puzzle has been proposed which suggests the use of the modified Gaussian-type initial conditions.* We find that the choice of the initial condition in the form of a two-dimensional Gaussian profile for the transverse energy leads to a complete and consistent description of soft observables measured at RHIC. The transverse-momentum spectra, the elliptic-flow, and the HBT correlation radii, including the ratio $R_{\text{out}}/R_{\text{side}}$ are very well described.
7. *The processes of the free streaming of partons followed by the sudden equilibration were incorporated in the model.* Those two processes deliver modified initial conditions for the hydrodynamics. In particular, the inclusion of the free-streaming stage allows for the delayed start of the hydrodynamic evolution, which is a desirable effect in the context of the early thermalization problem.

The Thesis is organized as follows. In Chapter 2 we describe the construction of our equation of state. In Chapter 3 we present the hydrodynamic equations and transform them to the form used in the numerical calculations. The initial conditions and the freeze-out prescription are introduced in Chapters 4 and 5, respectively. The fits to the RHIC data obtained with the standard initial conditions are presented in Chapter 6. The predictions for the LHC are given in Chapter 7. The solution of the RHIC HBT puzzle with modified Gaussian initial conditions is presented and discussed in Chapter 8. In that Section we also discuss the inclusion of the parton free-streaming as the pre-hydrodynamics stage. The Summary and four Appendices close the Thesis.

We use everywhere the natural units with $c = \hbar = k_B = 1$. The signature of the metric tensor is $(+ - - -)$.

The results discussed in this Thesis were published in the following articles:

1. M. Chojnacki, W. Florkowski, and T. Csörgő,
Formation of Hubble - like flow in little bangs,
Phys. Rev. **C71** (2005) 044902, (nucl-th/0410036).
2. M. Chojnacki and W. Florkowski,
Characteristic form of boost-invariant and cylindrically asymmetric hydrodynamic equations,
Phys. Rev. **C74** (2006) 034905, (nucl-th/0603065).
3. M. Chojnacki and W. Florkowski,
Temperature dependence of sound velocity and hydrodynamics of ultra - relativistic heavy-ion collisions,
Acta Phys. Pol. **B38** (2007) 3249, (nucl-th/0702030).
4. M. Chojnacki, W. Florkowski, W. Broniowski, and A. Kisiel,
Soft heavy-ion physics from hydrodynamics with statistical hadronization: Predictions for collisions at $\sqrt{s_{NN}} = 5.5$ TeV,
Phys. Rev. **C78** (2008) 014905, arXiv:0712.0947 [nucl-th].
5. W. Broniowski, M. Chojnacki, W. Florkowski, and A. Kisiel,
Uniform Description of Soft Observables in Heavy-Ion Collisions at $\sqrt{s_{NN}} = 200$ GeV,
Phys. Rev. Lett. **101** (2008) 022301, arXiv:0801.4361 [nucl-th].
6. A. Kisiel, W. Broniowski, M. Chojnacki, and W. Florkowski,
Azimuthally sensitive femtoscopy in hydrodynamics with statistical hadronization from the BNL Relativistic Heavy Ion Collider to the CERN Large Hadron Collider,
Phys. Rev. **C79** (2009) 014902, arXiv:0808.3363 [nucl-th].
7. W. Broniowski, W. Florkowski, M. Chojnacki, A. Kisiel,
Free-streaming approximation in early dynamics of relativistic heavy-ion collisions,
submitted to Phys. Rev. **C**, arXiv:0812.3393 [nucl-th].

They were also presented during various international conferences including:

1. M. Chojnacki,
Hubble-like Flows in Relativistic Heavy-Ion Collisions,
Acta Phys. Hung. **A27** (2006) 331, (nucl-th/0510092).
18th International Conference On Ultrarelativistic Nucleus-Nucleus Collisions: Quark Matter 2005 (QM 2005).
2. M. Chojnacki,
Cylindrically asymmetric hydrodynamic equations,
Acta Phys. Polon. **B37** (2006) 3391, (nucl-th/0609060).
Cracow School Of Theoretical Physics: 46th Course 2006.
3. M. Chojnacki,
Temperature-dependent sound velocity in hydrodynamic equations for relativistic heavy-ion collisions,

- J. Phys. **G35** (2008) 044074, arXiv:0709.1594 [nucl-th].
International Conference On Strangeness In Quark Matter (SQM 2007).
4. W. Florkowski, M. Chojnacki, W. Broniowski, A. Kisiel,
Soft-hadronic observables for relativistic heavy-ion collisions at RHIC and LHC,
Acta Phys. Polon. **B39** (2008) 1555, arXiv:0804.0974 [nucl-th].
Cracow Epiphany Conference On LHC Physics.
 5. W. Florkowski, W. Broniowski, M. Chojnacki, A. Kisiel,
Hydrodynamics and perfect fluids: Uniform description of soft observables in Au+Au collisions at RHIC,
arXiv:0811.3761 [nucl-th] and arXiv:0902.0377 [hep-ph].
38th International Symposium On Multiparticle Dynamics ISMD08.
 6. W. Florkowski, W. Broniowski, M. Chojnacki, A. Kisiel,
Solution of the RHIC HBT puzzle with Gaussian initial conditions,
arXiv:0812.4125 [nucl-th].
International Conference On Strangeness In Quark Matter (SQM 2008).
 7. W. Broniowski, W. Florkowski, M. Chojnacki, A. Kisiel,
Initial conditions for hydrodynamics: implications for phenomenology,
arXiv:0812.4935 [nucl-th].
IV Workshop on Particle Correlations and Femtoscopy.
 8. W. Florkowski, W. Broniowski, M. Chojnacki, A. Kisiel,
Consistent hydrodynamic description of one- and two-particle observables in relativistic heavy-ion collisions at RHIC,
arXiv:0901.1251 [nucl-th].
IV Workshop on Particle Correlations and Femtoscopy.

Chapter 2

Thermodynamics of relativistic baryon-free matter

In our approach we concentrate on the description of the mid-rapidity region of ultra-relativistic heavy-ion collisions. Statistical analysis applied to the highest-energy RHIC data indicates that the baryon chemical potential μ_B at the chemical freeze-out is of about 25 MeV in this region [28, 29, 30, 31, 32]. The predictions of the statistical models for LHC give even smaller values, $\mu_B \approx 0.8$ MeV [33]. On the other hand, the expected temperature is of about 150 - 170 MeV, hence the ratio μ_B/T is small and in the hydrodynamic equations we can approximately assume that the baryon chemical potential vanishes. In this situation, as discussed in Ref. [34], the whole information about the equation of state is encoded in the temperature-dependent sound velocity $c_s(T)$. We assume that at low temperatures the sound velocity is given by the hadron-gas model with a complete set of hadronic resonances. In this case the function $c_s^2(T)$ approaches zero as T/m_π , which is the characteristics of the pion gas (m_π is the pion mass). On the other hand, at high temperatures our equation of state coincides with the recent lattice simulations of QCD [35]. The thermodynamic properties of the hadron gas and the quark-gluon plasma are discussed below in more detail in Sects. 2.1 and 2.2, respectively.

In the transition region between the hadron gas and the plasma, whose position is characterized by the critical temperature T_c , different interpolations between the hadron gas result and the lattice result may be considered. In Ref. [36] we showed, however, that the most promising equation of state is based on the simplest interpolation between the hadron-gas model and the lattice data, see Fig. 2.1. This is so because the sound velocity function which does not exhibit a distinct minimum at the critical temperature leads to the relatively short evolution time and this effect helps to describe correctly the HBT data. The effects of different forms of the sound velocity are discussed in Sect. 2.3. Since the simplest interpolation is the best, most of the results presented in this Thesis are obtained with the sound velocity function shown in Fig 2.1.

The knowledge of the function $c_s(T)$ allows us to determine all other thermodynamic properties of our system. This is achieved with the help of the following

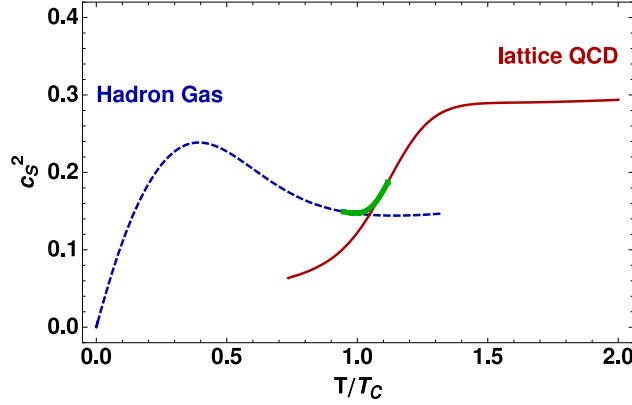


Figure 2.1: Temperature dependence of the square of the sound velocity at zero baryon density. The plot shows the result of the lattice simulations of QCD [35] (solid line) and the result obtained with the ideal hadron-gas model discussed in Sect. 2.1 (dashed line). A piece of the thick solid line describes the simplest interpolation between the two calculations. The critical temperature T_c equals 170 MeV. It is defined as the place where the sudden change of the thermodynamic variables occurs, see Fig. 2.2

thermodynamic identities

$$\varepsilon + P = Ts, \quad d\varepsilon = Tds, \quad dP = sdT, \quad c_s^2 = \frac{dP}{d\varepsilon}, \quad (2.1)$$

where ε is the energy density, P is the pressure, T is the temperature, and s is the entropy density. In Fig. 2.2 we display the entropy and energy densities as functions of T , and the pressure and sound velocity as functions of the energy density. These quantities follow directly from the assumed form of the function $c_s(T)$, shown in Fig. 2.1.

We note that other equations of state and their impact on the physical observables were recently studied in Ref. [37]. The result of that work was that the transverse-momentum spectra are quite insensitive to the assumed form of the equation of state. On the other hand, a noticeable dependence of the elliptic flow on the equation of state was observed. This dependence favored the strong first order phase transition. In Ref. [37] the effects concerning the HBT were not studied. Our recent work indicates that the constraints from the particle interferometry data exclude the strong first order phase transition since it leads to the unrealistically long evolution times.

We stress that by using the lattice results we take into account the non-perturbative aspects of the plasma behavior, which may be regarded as the effective inclusion of the strongly-interacting quark-gluon plasma; large deviations from the ideal-gas behavior directly indicate the non-negligible interactions present in the plasma. In particular, c_s^2 is significantly below the ideal-gas value of $1/3$ also at temperatures way above T_c . Note that in agreement with the present knowledge, no real phase transition is present in the system, but a *smooth cross-over*, therefore c_s does not drop to zero at T_c but remains a smooth function.

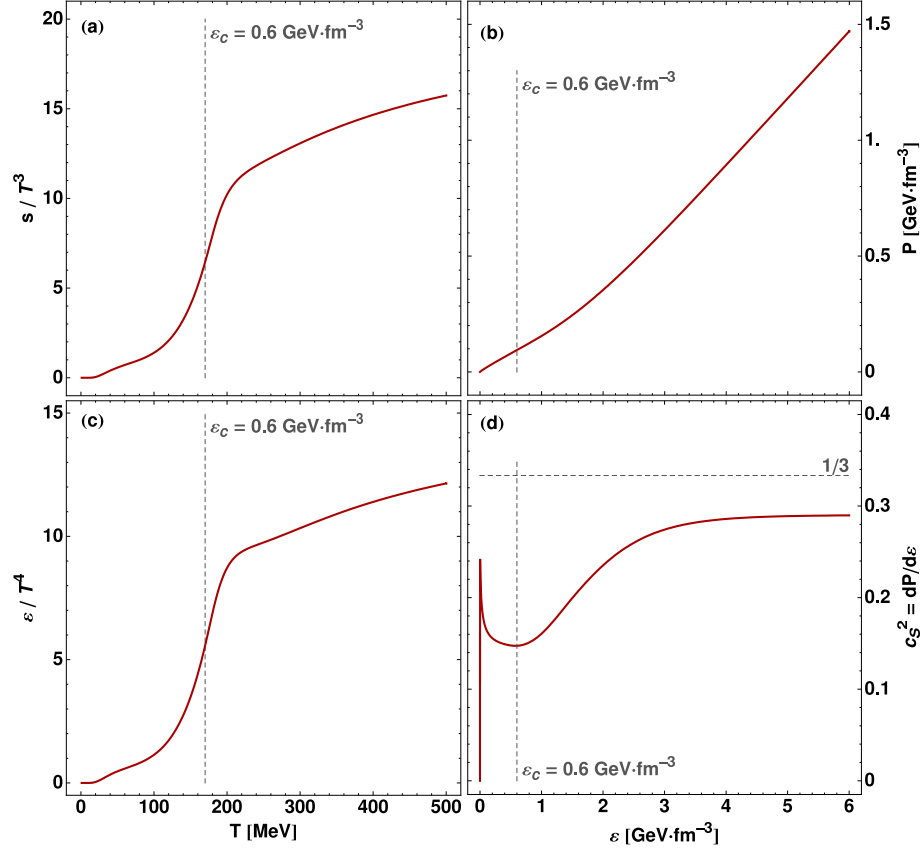


Figure 2.2: The two left panels: the entropy and energy densities, scaled by T^3 and T^4 , respectively, shown as functions of the temperature. The two right panels: the pressure and sound velocity shown as functions of the energy density. The presented thermodynamic functions follow directly from the temperature-dependent sound velocity shown in Fig. 2.1. We observe a sudden but smooth change of s/T^3 and ϵ/T^4 at $T \sim T_c$. The vertical line indicates in all cases the critical energy density corresponding to $T_c = 170$ MeV. With our equation of state one finds $\epsilon_c = 0.6$ GeV/fm³.

2.1 Hadron gas

The hadron-gas model is based on the assumption that all known hadrons (including hadronic resonances) form a multicomponent perfect gas. In this case, well known formulas for the thermodynamic variables of the relativistic perfect gases [38, 39] may be applied. Of course, the hadron-gas model is applicable in the temperature region below the critical temperature $T_c = 170$ MeV. With increasing temperature the density of hadrons becomes so large that they start overlapping and the very idea of hadrons breaks down. We note that only in the case of pions the quantum statistics is necessary. For other particles, which are much heavier and less abundant, the Boltzmann classical limit is sufficient [40].

2.1.1 Pion gas

Pions are the most abundant particles produced in heavy-ion collisions. Because of their large multiplicity the statistical quantum effects cannot be neglected and one should use the Bose-Einstein distributions to describe the pion spectra. Additionally, since pions do not carry the baryon number and strangeness, their chemical potential may be assumed to be zero (possible values of the isospin chemical potential are very small, $\mu_{I_3} < 1$ MeV, and are usually neglected). Therefore, in describing the thermodynamic properties of the pion gas (πG) we use the relations for a massive boson gas with zero chemical potential, which are worked out in Appendix A, namely

$$s_i^{\pi G}(T) = \frac{1}{2\pi^2} m_i^3 \sum_{\kappa=1}^{\infty} \frac{1}{\kappa} K_3\left(\frac{m_i}{T} \kappa\right), \quad (2.2)$$

$$P_i^{\pi G}(T) = \frac{1}{2\pi^2} T^2 m_i^2 \sum_{\kappa=1}^{\infty} \frac{1}{\kappa^2} K_2\left(\frac{m_i}{T} \kappa\right), \quad (2.3)$$

$$\varepsilon_i^{\pi G}(T) = \frac{1}{2\pi^2} T m_i^2 \sum_{\kappa=1}^{\infty} \frac{1}{\kappa^2} \left[3 T K_2\left(\frac{m_i}{T} \kappa\right) + m_i \kappa K_1\left(\frac{m_i}{T} \kappa\right) \right], \quad (2.4)$$

where the index i specifies the isospin (distinguishes between π^- , π^0 , π^+) and m_i is the mass of the appropriate pion. The infinite sum over κ is the technical way to include the Bose-Einstein statistics. In the numerical calculations it is sufficient to include only the first four terms – the inverse powers of κ reduce the higher-order terms fast enough.

Knowing the expression for the entropy density of the pion gas, we calculate the sound velocity from the last equation in (2.1). In the approximation that the pion masses are equal ($m_i = m_\pi$) we obtain

$$(c_s^2)^{\pi G}(T) = \frac{2T}{m_\pi} \frac{\sum_{\kappa=1}^{\infty} \frac{1}{\kappa} K_3\left(\frac{m_\pi}{T} \kappa\right)}{\sum_{\kappa=1}^{\infty} \left[K_2\left(\frac{m_\pi}{T} \kappa\right) + K_4\left(\frac{m_\pi}{T} \kappa\right) \right]}. \quad (2.5)$$

It is interesting to observe the behavior of the sound velocity in the limit when temperature approaches zero. The arguments of the Bessel functions $K_\nu(z)$ tend to infinity and we can use the power series expansion to find that

$$(c_s^2)^{\pi G}(T \rightarrow 0) = \frac{T}{m_\pi} \frac{\sum_{\kappa=1}^{\infty} \left[\kappa^{-\frac{3}{2}} e^{-\frac{m_\pi}{T} \kappa} + \dots \right]}{\sum_{\kappa=1}^{\infty} \left[\kappa^{-\frac{1}{2}} e^{-\frac{m_\pi}{T} \kappa} + \dots \right]} \rightarrow \frac{T}{m_\pi}, \quad (2.6)$$

see Eq. (D.8) from Appendix D. On the other hand, when temperature is large ($T \gg m_\pi$) we expand the modified Bessel functions according to (D.7) and get the

following expression

$$(c_s^2)^{\pi G}(T \rightarrow \infty) = \frac{1}{3} \frac{\sum_{\kappa=1}^{\infty} \left[\kappa^{-4} - \frac{1}{8} \left(\frac{m_\pi}{T} \kappa \right)^2 + \frac{1}{8} \left(\frac{m_\pi}{T} \kappa \right)^4 + \dots \right]}{\sum_{\kappa=1}^{\infty} \left[\kappa^{-4} - \frac{1}{24} \left(\frac{m_\pi}{T} \kappa \right)^2 + \frac{1}{96} \left(\frac{m_\pi}{T} \kappa \right)^4 + \dots \right]} \rightarrow \frac{1}{3}. \quad (2.7)$$

The last limit illustrates the expected result – at very high temperatures the massive pion gas behaves effectively like a massless gas with $P = \frac{1}{3}\varepsilon$ and its sound velocity squared equals $\frac{1}{3}$. (See Tables A.4 and A.5, where the complete formulas for pressure and energy density in various limits are given).

2.1.2 Classical gas

Strictly speaking, all particles produced in heavy-ion collisions obey the quantum statistics, however for all particles other than pions the effects of quantum statistics are numerically negligible. Thus, to calculate the thermodynamic functions of the hadrons other than pions we may use the following formulas

$$s_i^{CG}(T) = \frac{g_i}{2\pi^2} m_i^3 K_3 \left(\frac{m_i}{T} \right), \quad (2.8)$$

$$P_i^{CG}(T) = \frac{g_i}{2\pi^2} T^2 m_i^2 K_2 \left(\frac{m_i}{T} \right), \quad (2.9)$$

$$\varepsilon_i^{CG}(T) = \frac{g_i}{2\pi^2} T m_i^2 \left[3 T K_2 \left(\frac{m_i}{T} \right) + m_i K_1 \left(\frac{m_i}{T} \right) \right], \quad (2.10)$$

where $g_i = 2s_i + 1$ is the degeneration factor which holds the information about the spin degeneration of i -th particle. The sound velocity in the classical massive case is defined as follows

$$(c_s^2)_i^{CG}(T) = \frac{2T}{m_i} \frac{K_3 \left(\frac{m_i}{T} \right)}{K_2 \left(\frac{m_i}{T} \right) + K_4 \left(\frac{m_i}{T} \right)}, \quad (2.11)$$

and has the same asymptotic features as the pion gas, namely it tends to the value $\frac{1}{3}$ for very high temperatures and becomes proportional to T if the temperature tends to zero.

2.1.3 Massive hadron gas

The massive hadron gas (HG) model is the sum of both massive pion gas and massive classical gas of all other hadrons. In our study, the information on the mass and spin of individual particles comes from the input file to the **SHARE** program [41]. The table *particles.data* holds parameters for 371 particles consisting from u , d and s quarks. Thus, for all hadrons we may write

$$s^{HG}(T) = \sum_{i=1}^3 (s)_i^{\pi G}(T) + \sum_{i=4}^{371} (s)_i^{CG}(T), \quad (2.12)$$

$$(c_s^2)^{HG}(T) = \frac{s^{HG}}{T} \frac{dT}{d(s^{HG})}, \quad (2.13)$$

and all other thermodynamic quantities (s , P and ε) are expressed in the analogous way.

2.2 Quark-Gluon Plasma

In our approach we use the results of the lattice simulations of QCD at the finite temperature presented in Ref. [35], see Fig. 2.3. They were obtained for physical masses of the light quarks and the strange quark. The pressure data obtained from

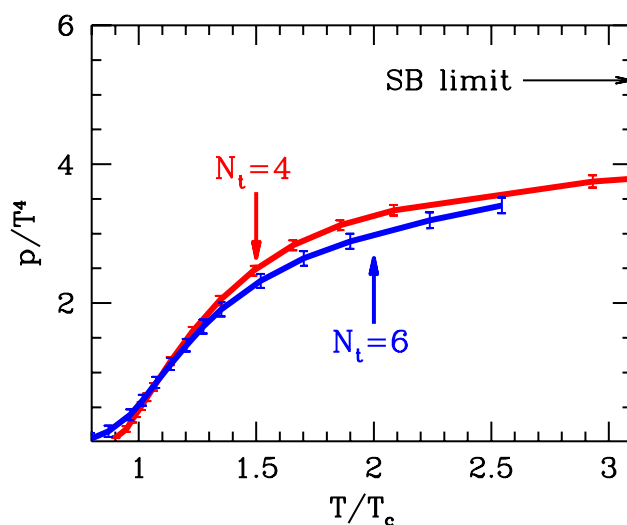


Figure 2.3: QCD pressure as a function of temperature normalized by T^4 [35]. Results are obtained for two lattice spacings $N_t = 4$ (red) and $N_t = 6$ (blue).

the QCD lattice calculation in Ref. [35] have been recently parameterized for the case of $N_t = 6$ in Ref. [42], see Fig. 2.4. The parameterization has the form

$$P = c T^4 \sigma(T_c/T), \quad \sigma(g) = \frac{1 + e^{-\frac{a}{b}}}{1 + e^{\frac{g-a}{b}}} e^{-\lambda g}, \quad (2.14)$$

where the dimensionless fit parameters equal: $a = 0.91$, $b = 0.11$, $c = 5.21$ and $\lambda = 1.08$. Taking the lattice result at the face value, one expects that the sound velocity significantly drops down in the region $T \approx T_c$. Similar behavior, with $c_s(T_c)$ reaching zero, is expected in the case of the first order phase transition where the changes of the energy happen at constant pressure. However, the lattice simulations suggest that for three massive quarks with realistic masses we deal with the cross-over rather than with the first order phase transition, hence the sound velocity remains finite, as is consistently shown in Fig. 2.1.

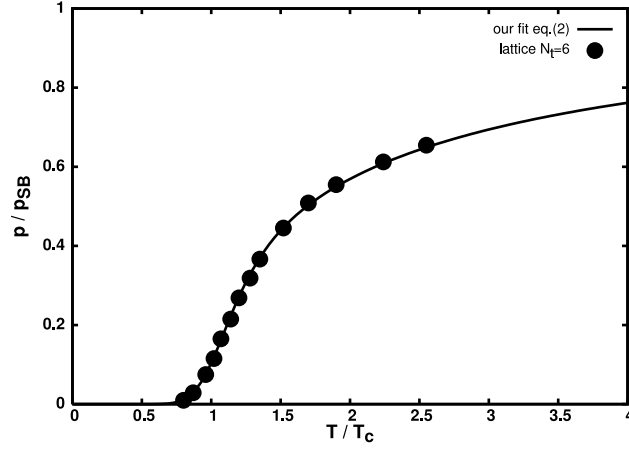


Figure 2.4: Pressure as a function of temperature normalized to the pressure corresponding to the Stefan-Boltzmann limit. Points represent results from the QCD lattice simulations [35], whereas the line is the data fit from Ref. [42].

2.3 Modeling the crossover phase transition

The exact values of the sound velocity in the region $T \approx T_c$ are poorly known. The lattice calculations are not very much reliable for $T < T_c$ and, at the same time, the use of the hadron gas model with vacuum parameters becomes unrealistic for large densities (temperatures). The authors of Ref. [35] state that in the hadronic phase the lattice spacing is larger than 0.3 fm and the lattice artifacts cannot be controlled in this region. In this situation, it is practical to consider different interpolations

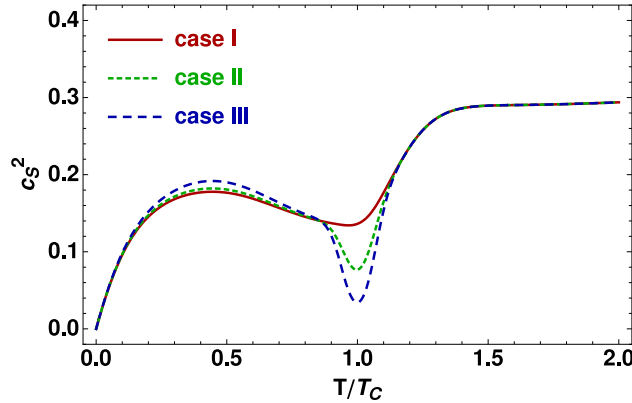


Figure 2.5: Three different forms of the sound-velocity function analyzed in Ref. [36]. The solid line describes the interpolation between the lattice and the hadron-gas results [34] with a shallow minimum where $c_s^2 = 0.14$ (case I), the dashed line describes the interpolation with a dip where $c_s^2 = 0.08$ (case II), finally the long-dashed line describes the interpolation with a deep minimum where $c_s^2 = 0.03$ (case III). Note that the case I is the *approximation* of the result shown previously in Fig. 2.1 – see discussion in the text.

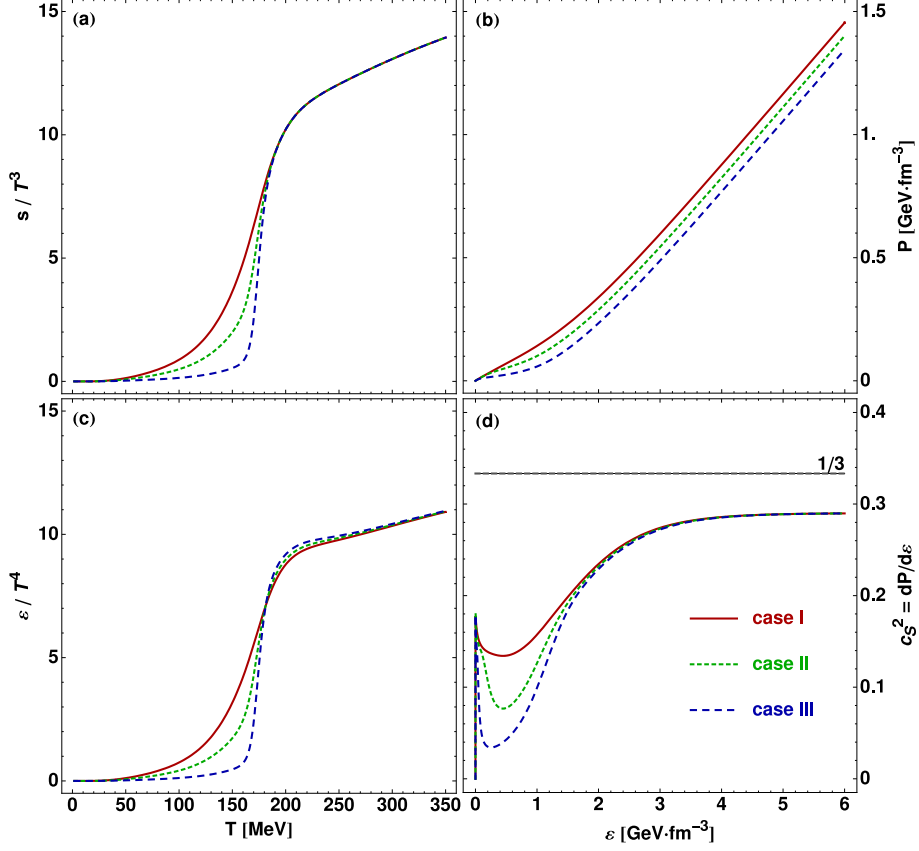


Figure 2.6: The temperature dependence of the entropy density and energy density, panels (a) and (c), as well as the energy density dependence of the pressure and sound velocity, panels (b) and (d). One can observe that the deeper is the minimum of the sound velocity function, the steeper is the increase of the entropy density and the energy density.

between the lattice and hadron-gas results and to analyze the physical effects of a particular choice of the interpolating function. This type of the study was performed in Ref. [36]. Here we shortly discuss the main conclusions of this analysis.

In Ref. [36] we considered three different sound-velocity functions $c_s(T)$. Below, we refer to these three options as to the cases I, II and III, see Fig. 2.5. In the case I, we use the sound-velocity function which agrees with the ideal hadron gas model of Ref. [34] in the temperature range $0 < T < 0.85 T_c$ and with the lattice result in the temperature range $T > 1.15 T_c$ ¹. In the region close to the critical temperature, $0.85 T_c < T < 1.15 T_c$, a simple interpolation between the two results is used. We have checked that such a simple interpolation yields directly the entropy density

¹Ref. [34] uses the approximation where the sum over hadronic states is replaced by the integral with the mass-density functions worked out in [43]. This leads to small differences between $c_s(T)$ used in [34, 36] and [44]

consistent with the lattice result. Namely, the use of the thermodynamic relation

$$s(T) = s(T_{\min}) \exp \left[\int_{T_{\min}}^T \frac{dT'}{T' c_s^2(T')} \right], \quad (2.15)$$

relating the entropy density with the sound velocity for zero baryon chemical potential, gives the function $s(T)$ which agrees with the lattice result at high temperatures, $s(T)/T^3 \approx 12$ at $T = 1.5 T_c$ [35].

In the cases II and III, the sound-velocity interpolating functions have a distinct minimum at $T = T_c$. Comparing to the case I [with $c_s(T_c) = 0.37$ and $c_s^2(T_c) = 0.14$], the value of the sound velocity at $T = T_c$ is reduced by 25 % in the case II [where $c_s(T_c) = 0.28$ and $c_s^2(T_c) = 0.08$], and by 50% in the case III [where $c_s(T_c) = 0.19$ and $c_s^2(T_c) = 0.03$]. From Eq. (2.15) one concludes that the decrease of the sound velocity at T_c leads to the increase of entropy density for high temperatures. Hence, in order to have the same value of the entropy density at high temperatures, a decrease of the sound velocity function in the region $T \approx T_c$ should be compensated by its increase in a different temperature range. For our interpolating functions in the cases II and III we assume that the values of $c_s(T)$ in the range $0.15 T_c < T < 0.85 T_c$ are slightly higher than in the case I, see Fig. 2.5. Such modifications may be regarded as the parameterization of the repulsive van der Waals forces in the hadron gas. The values of the maxima are chosen in such a way that the entropy densities for three considered cases are consistent with the lattice result, see the upper left panel of Fig. 2.6 where the functions $s(T)/T^3$ are shown. We stress that in the three considered cases the values of $c_s(T)$ in the temperature range $T_c < T < 1.25 T_c$ remain significantly below the massless limit $1/\sqrt{3}$. Such a limiting value is implicitly used in many hydrodynamic codes assuming the equation of state of non-interacting massless quarks and gluons for $T > T_c$, see for example the extended 3+1 hydrodynamic model of Ref. [23].

The studies of the hydrodynamic spacetime evolution of matter described by the equations of state I, II and III were performed in Ref. [36]. As expected, we found that the drop of c_s at $T = T_c$ leads to the prolonged time of the evolution, hence leads to the increase of the $R_{\text{out}}/R_{\text{side}}$ ratio of the HBT radii. This behavior is in contradiction with the observed data which indicate $R_{\text{out}}/R_{\text{side}} \sim 1$. Thus, we have decided to exclude the cases II and III from further analysis and to restrict our consideration to the case I.

Chapter 3

Relativistic hydrodynamics of perfect fluid

In this Chapter we present the main ingredients of our hydrodynamic model. We start with the general formulation of the relativistic hydrodynamics in the case of vanishing baryon number. Next, we implement the idea of boost-invariance that allows us to restrict our considerations to the plane $z = 0$. In the subsequent Sections of this Chapter we show that the hydrodynamic equations may be rewritten in the form where only two equations are independent (at the expense of the formal extension of the variable $r = \sqrt{x^2 + y^2}$ to negative values) and the boundary conditions at the origin are automatically fulfilled. Such a form, being the direct generalization of the approach introduced in Ref. [45], turned out to be very convenient in the numerical analyses.

3.1 Hydrodynamic equations for baryon free matter

As the system reaches local thermodynamic equilibrium its further evolution is governed by the conservation laws for energy and momentum, which can be expressed by the formula

$$\partial_\mu T^{\mu\nu} = 0, \quad (3.1)$$

where the energy-momentum tensor has the form

$$T^{\mu\nu} = (\varepsilon + P) u^\mu u^\nu - P g^{\mu\nu}. \quad (3.2)$$

Here ε is the energy density, P is the pressure, $g^{\mu\nu}$ is the metric tensor (we use the convention where $g^{00} = +1$) and u^μ is the four-velocity,

$$u^\mu = \gamma (1, \mathbf{v}). \quad (3.3)$$

In Eq. (3.3) \mathbf{v} is the local three-velocity of the fluid and γ is the Lorentz factor

$$\gamma = (1 - v^2)^{-\frac{1}{2}}. \quad (3.4)$$

In general situations, in the relativistic systems the energy density and pressure depend on the temperature and baryon number density. This requires that the baryon number conservation law,

$$\partial_\mu j_B^\mu = 0, \quad (3.5)$$

should be considered together with (3.1). However, in the case of the central rapidity region of ultra-relativistic heavy-ion collisions the dominating degrees of freedom are mesons (initially gluons), hence the net baryon number is very close to zero. In such a case the local value of baryon chemical potential is negligible, $\mu_B \approx 0$, and we can express the entropy density s , pressure P , and energy density ε by temperature alone. This allows us to use the thermodynamic identities (2.1) and write the conservation laws (3.1) in the form.

$$\partial_\mu (T s u^\mu u^\nu) = \partial^\nu P. \quad (3.6)$$

After performing simple transformations shown explicitly in Appendix B.2 Eq. (3.6) leads to the two formulas

$$u^\mu \partial_\mu (T u^\nu) = \partial^\nu T, \quad (3.7)$$

$$\partial_\mu (s u^\mu) = 0. \quad (3.8)$$

Eq. (3.7) is the acceleration equation and represents the relativistic analog of the Euler equation known from the classical hydrodynamics. Eq. (3.8) states that the evolution is adiabatic (entropy is conserved). In the non-covariant notation the hydrodynamic equations (3.7) and (3.8) are expressed by the following expressions [45]

$$\frac{\partial}{\partial t} (T \gamma \mathbf{v}) + \nabla (T \gamma) = \mathbf{v} \times [\nabla \times (T \gamma \mathbf{v})], \quad (3.9)$$

$$\frac{\partial}{\partial t} (s \gamma) + \nabla (s \gamma \mathbf{v}) = 0. \quad (3.10)$$

The four equations above can be written in the Cartesian coordinates in the equivalent form as

$$(v^2 - 1) \frac{\partial \ln T}{\partial t} + \frac{d \ln T}{dt} + \frac{1}{1 - v^2} v \frac{dv}{dt} = 0, \quad (3.11)$$

$$(1 - v^2) \left(v_y \frac{\partial \ln T}{\partial x} - v_x \frac{\partial \ln T}{\partial y} \right) + v_y \frac{dv_x}{dt} - v_x \frac{dv_y}{dt} = 0, \quad (3.12)$$

$$(1 - v^2) \frac{\partial \ln T}{\partial z} + v_z \frac{d \ln T}{dt} + \frac{dv_z}{dt} + \frac{v_z}{1 - v^2} v \frac{dv}{dt} = 0, \quad (3.13)$$

$$\frac{d \ln s}{dt} + \frac{v}{1 - v^2} \frac{dv}{dt} + \frac{\partial v_x}{\partial x} + \frac{\partial v_y}{\partial y} + \frac{\partial v_z}{\partial z} = 0, \quad (3.14)$$

where the total time derivative is defined by the equation

$$\frac{d}{dt} = \frac{\partial}{\partial t} + \mathbf{v} \cdot \nabla. \quad (3.15)$$

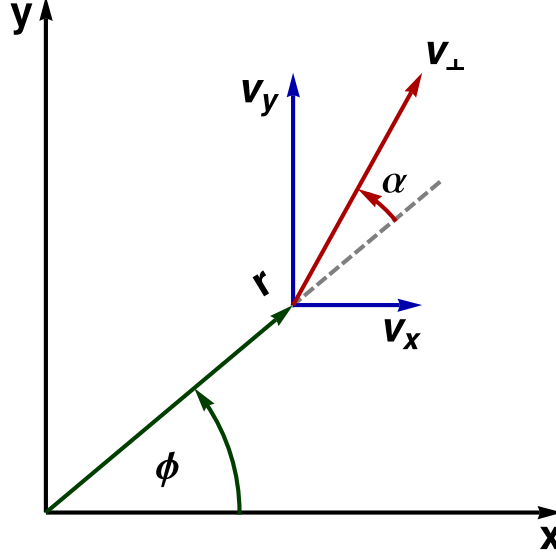


Figure 3.1: Decomposition of the flow velocity vector in the plane $z = 0$. In our approach we use the magnitude of the transverse flow $v_{\perp} = \sqrt{v_x^2 + v_y^2}$ and the angle α as two independent quantities, instead of v_x and v_y . The longitudinal component of the flow $v_z = z/t$, a consequence of boost-invariance.

The details of the transformations leading from (3.6) to (3.11) - (3.14) can be found in Appendix B.3. Equations (3.11) - (3.14) do not form a closed system of equations since they contain five independent variables T , s , v_x , v_y and v_z . An additional equation is needed to close them, i.e., the equation of state is required which introduces the relation between T and s . Alternatively, the equation of state may be included by the use of the temperature dependent sound velocity

$$c_s^2(T) = \frac{\partial P}{\partial \epsilon} = \frac{s}{T} \frac{\partial T}{\partial s}, \quad (3.16)$$

The temperature dependent sound velocity for strongly interacting matter that is used in our work was discussed thoroughly in Chapt. 2 and is plotted in Fig. 2.1.

3.2 Implementation of boost-invariance

The experimental data collected at RHIC by the BRAHMS Collaboration [46] suggests that in the midrapidity region the particle yields do not vary much with rapidity. Thus, we can assume that number of particles per unit rapidity in the range of $|y| \leq 1$ is essentially constant and the midrapidity region (central region) is boost-invariant. This symmetry demands that the longitudinal component of the velocity has the form of the Bjorken flow [47],

$$v_z = \frac{z}{t}, \quad (3.17)$$

and the thermodynamic scalar variables like temperature or entropy density are functions of the longitudinal proper time $\tau = \sqrt{t^2 - z^2}$ and the transverse coordinates x and y . *In practice, these properties mean that we can solve the hydrodynamic equations for $z = 0$ and by using the appropriate Lorentz transformations we obtain solutions for $z \neq 0$.*

Adopting the procedure outlined above and restricting our considerations to the plane $z = 0$ we observe that Eq. (3.13) is automatically fulfilled and we are left with only three independent equations

$$(v_\perp^2 - 1) \frac{\partial \ln T}{\partial t} + \frac{d \ln T}{dt} + \frac{1}{1 - v_\perp^2} v_\perp \frac{dv_\perp}{dt} = 0, \quad (3.18)$$

$$(1 - v_\perp^2) \left(v_y \frac{\partial \ln T}{\partial x} - v_x \frac{\partial \ln T}{\partial y} \right) + v_y \frac{dv_x}{dt} - v_x \frac{dv_y}{dt} = 0, \quad (3.19)$$

$$\frac{d \ln s}{dt} + \frac{v_\perp}{1 - v_\perp^2} \frac{dv_\perp}{dt} + \frac{\partial v_x}{\partial x} + \frac{\partial v_y}{\partial y} + \frac{1}{t} = 0, \quad (3.20)$$

where $v_\perp = \sqrt{v_x^2 + v_y^2}$ is the transverse velocity. The equations describing transverse evolution can be rewritten in the cylindrical coordinates which are convenient for further analysis [48] (details can be found in Appendix B.4.1 and B.5.1)

$$(v_\perp^2 - 1) \frac{\partial \ln T}{\partial t} + \frac{d \ln T}{dt} + \frac{1}{1 - v_\perp^2} v_\perp \frac{dv_\perp}{dt} = 0, \quad (3.21)$$

$$(1 - v_\perp^2) \left(v_\perp \sin \alpha \frac{\partial \ln T}{\partial r} - \frac{v_\perp \cos \alpha}{r} \frac{\partial \ln T}{\partial \phi} \right) - v_\perp^2 \left(\frac{d\alpha}{dt} + \frac{v_\perp \sin \alpha}{r} \right) = 0, \quad (3.22)$$

$$v_\perp \frac{d \ln s}{dt} + \frac{1}{1 - v_\perp^2} \frac{dv_\perp}{dt} - \frac{\partial v_\perp}{\partial t} - v_\perp^2 \sin \alpha \frac{\partial \alpha}{\partial r} + \frac{v_\perp^2 \cos \alpha}{r} \left(\frac{\partial \alpha}{\partial \phi} + 1 \right) + \frac{v_\perp}{t} = 0. \quad (3.23)$$

Here r is the distance from the beam axis, $r = \sqrt{x^2 + y^2}$, and ϕ is the azimuthal angle, $\phi = \tan^{-1}(y/x)$. These two coordinates parameterize the plane $z = 0$. The angle α is the function describing direction of the flow, $\alpha = \tan^{-1}(v_y/v_x) - \phi$, see Fig. 3.1. The differential operator d/dt used in Eqs. (3.21) - (3.23) is defined by the formula

$$\frac{d}{dt} = \frac{\partial}{\partial t} + v_\perp \cos \alpha \frac{\partial}{\partial r} + \frac{v_\perp \sin \alpha}{r} \frac{\partial}{\partial \phi}. \quad (3.24)$$

3.3 Characteristic form of hydrodynamic equations

In order to obtain the form of the hydrodynamic equations which is convenient for numerical studies we introduce new independent variables. In this respect we follow the method originally proposed by Baym et al. in Ref. [45] and the new form of

the equations will be called the characteristic form. We introduce the potential Φ defined as

$$d\Phi = \frac{1}{c_s} d\ln T = c_s d\ln s, \quad (3.25)$$

and the transverse rapidity $\eta_\perp = \tanh^{-1} v_\perp$. The new form of the hydrodynamic equations is expressed by the dimensionless auxiliary functions A_+ and A_- defined by the equations

$$A_\pm = \Phi \pm \eta_\perp. \quad (3.26)$$

The sum and difference of Eq. (3.21) and (3.23) together with Eq. (3.22) take the form

$$\begin{aligned} \frac{\partial A_\pm}{\partial t} + \frac{v_\perp \pm c_s}{1 \pm c_s v_\perp} \left[\cos \alpha \frac{\partial A_\pm}{\partial r} + \frac{\sin \alpha}{r} \frac{\partial A_\pm}{\partial \phi} \right] \\ - \frac{c_s}{1 \pm c_s v_\perp} \left[v_\perp \sin \alpha \frac{\partial \alpha}{\partial r} - \frac{v_\perp \cos \alpha}{r} \left(\frac{\partial \alpha}{\partial \phi} + 1 \right) - \frac{1}{t} \right] = 0, \end{aligned} \quad (3.27)$$

$$\begin{aligned} \frac{\partial \alpha}{\partial t} + v_\perp \cos \alpha \frac{\partial \alpha}{\partial r} + \frac{v_\perp \sin \alpha}{r} \left(\frac{\partial \alpha}{\partial \phi} + 1 \right) \\ - \frac{c_s(1 - v_\perp^2)}{v_\perp} \left[\sin \alpha \frac{\partial \Phi}{\partial r} - \frac{\cos \alpha}{r} \frac{\partial \Phi}{\partial \phi} \right] = 0, \end{aligned} \quad (3.28)$$

where the transverse velocity and the Φ potential are expressed through the auxiliary functions A_\pm as follows

$$v_\perp = \tanh \left(\frac{A_+ - A_-}{2} \right), \quad \Phi = \frac{A_+ + A_-}{2}. \quad (3.29)$$

Temperature and all other temperature dependent variables, e.g., the sound velocity, can be also calculated from the functions A_\pm ,

$$T = T_\Phi(\Phi) = T_\Phi \left(\frac{A_+ + A_-}{2} \right), \quad (3.30)$$

$$c_s(T) = c_s \left[T_\Phi \left(\frac{A_+ + A_-}{2} \right) \right]. \quad (3.31)$$

Here we have introduced the subscripts to make clear what kind of the argument is expected for a given function. For example, the temperature may be considered as a function of entropy density or Φ . In those two cases one should use the functions T_S or T_Φ , respectively. If the equation of state is known all such functions can be easily calculated and Eqs. (3.27) and (3.28) may be used to determine three unknown functions A_+ , A_- , and α .

3.4 Boundary conditions

Having in mind the heavy-ion collisions at RHIC and at LHC we consider the collisions of identical nuclei, Au+Au or Pb+Pb, which collide moving initially along

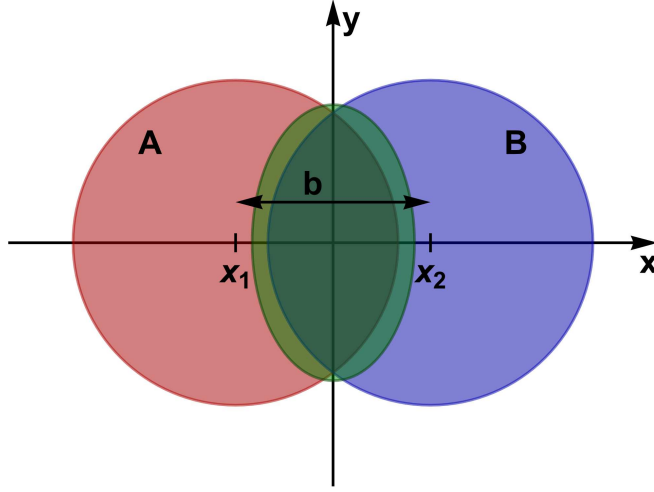


Figure 3.2: Non-central collision of two identical nuclei at the impact vector \mathbf{b} , viewed in the transverse plane. The nucleus A is located at $(x_1, y_1) = (-b/2, 0)$ and the nucleus B at $(x_2, y_2) = (b/2, 0)$. The overlapping region has the shape of an almond elongated in the direction of the y -axis.

the z -axis. The positions of the centers of nuclei depend on the impact parameter \mathbf{b} and for non-central collision they may be located in the transverse plane at $\mathbf{x}_1 = (x_1, y_1) = (-b/2, 0)$ and at $\mathbf{x}_2 = (x_2, y_2) = (b/2, 0)$, see Fig. 3.2. The distribution of matter created just after the collision is not cylindrically symmetric and has an ellipsoidal shape (one commonly speaks of an almond shape). With the use of the coordinate system explained above the transverse velocity must vanish at the origin of the system namely

$$v_{\perp}(t, r = 0, \phi) = 0. \quad (3.32)$$

Also the gradients with respect to the distance r of temperature and entropy density must converge to zero at $r = 0$

$$\frac{\partial T(t, r, \phi)}{\partial r} \xrightarrow{r \rightarrow 0} 0, \quad \frac{\partial s(t, r, \phi)}{\partial r} \xrightarrow{r \rightarrow 0} 0. \quad (3.33)$$

The boundary conditions (3.32) and (3.33) can be naturally fulfilled by the following Ansatz

$$\begin{cases} A_+(t, r, \phi) &= A(t, r, \phi), \\ A_-(t, r, \phi) &= A(t, -r, \phi), \\ \alpha(t, -r, \phi) &= \alpha(t, r, \phi). \end{cases} \quad r > 0 \quad (3.34)$$

The domain of the transverse distance r has been extended to the negative values of r . The two functions A_+ and A_- are replaced in this way by a single function A . At the same time the function α has been generalized to have negative arguments

by the condition that it is a symmetric function of r , see Fig. 3.3. With the help of the definitions (3.34), Eqs. (3.27) may be reduced to a single equation for the function $A(t, r, \phi)$,

$$\begin{aligned} \frac{\partial A}{\partial t} + \frac{v_{\perp} + c_s}{1 + c_s v_{\perp}} \left[\cos \alpha \frac{\partial A}{\partial r} + \frac{\sin \alpha}{r} \frac{\partial A}{\partial \phi} \right] \\ - \frac{c_s}{1 + c_s v_{\perp}} \left[v_{\perp} \sin \alpha \frac{\partial \alpha}{\partial r} - \frac{v_{\perp} \cos \alpha}{r} \left(\frac{\partial \alpha}{\partial \phi} + 1 \right) - \frac{1}{t} \right] = 0. \end{aligned} \quad (3.35)$$

The transverse velocity and Φ potential from Eq. (3.29) are now expressed as

$$v_{\perp}(t, r, \phi) = \tanh \left(\frac{A(t, r, \phi) - A(t, -r, \phi)}{2} \right), \quad (3.36)$$

$$\Phi(t, r, \phi) = \frac{A(t, r, \phi) + A(t, -r, \phi)}{2}. \quad (3.37)$$

In addition, the use of cylindrical coordinates implies the periodicity of all functions in angle ϕ thus creating another set of periodic boundary conditions

$$\begin{cases} A(t, r, \phi = 0) = A(t, r, \phi = 2\pi) \\ \alpha(t, r, \phi = 0) = \alpha(t, r, \phi = 2\pi) \end{cases}. \quad (3.38)$$

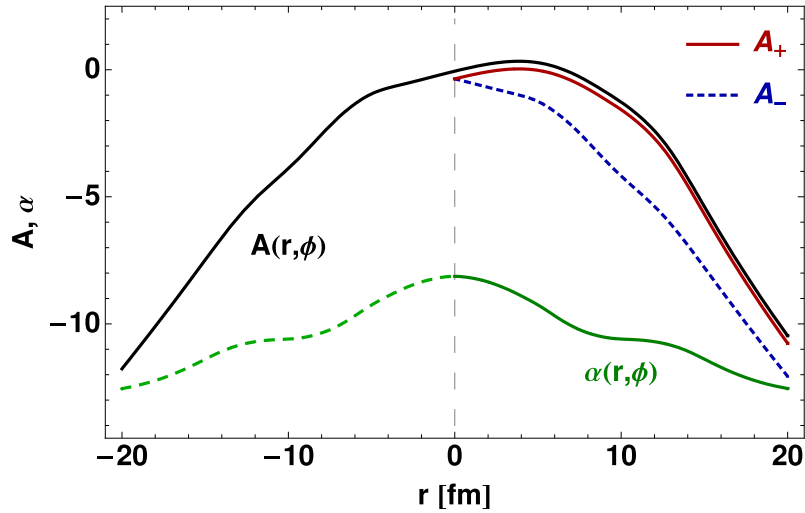


Figure 3.3: Construction of the functions $A_{\pm}(t, r, \phi)$ in terms of a single function $A(t, r, \phi)$, see Eq. (3.34). The function $\alpha(t, r, \phi)$ for negative values of r is obtained from the symmetry condition $\alpha(t, -r, \phi) = \alpha(t, r, \phi)$.

Chapter 4

Initial conditions

Along with the formulation of the hydrodynamic equations that govern the evolution of matter we must also specify a set of initial conditions that are required to unambiguously solve such equations – the hydrodynamic equations are first-order partial differential equations. The physical systems studied here are formed in the collisions of two identical gold nuclei (RHIC experiment) or two identical lead nuclei (the future heavy-ion program at LHC). In this Chapter we discuss in more detail the initial conditions used by us to analyze the collisions at RHIC and LHC. At first we discuss the most common form of the initial conditions that is based on the Glauber model. Next, we present the modified initial conditions where the initial energy density has a form of the two-dimensional Gaussian in the transverse plane. Finally, we present our method of including the parton free-streaming as a process which precedes the hydrodynamic evolution. In particular, we show how to match the free-streaming stage with the hydrodynamic stage.

4.1 Standard initial conditions

In the calculations presented in Chapter 6 and 7 we assume that the initial entropy density of the particles produced at the transverse position point \mathbf{x}_\perp is proportional to a source profile obtained from the Glauber approach. This is done in the similar way to other hydrodynamic calculations. Specifically, for the particle source profile we use a mixed model [49, 50], with a linear combination of the wounded-nucleon density $\rho_{\text{WN}}(\mathbf{x}_\perp)$ and the density of binary collisions $\rho_{\text{BC}}(\mathbf{x}_\perp)$, namely

$$s(\mathbf{x}_\perp) \propto \rho(\mathbf{x}_\perp) = \frac{1 - \kappa}{2} \rho_{\text{WN}}(\mathbf{x}_\perp) + \kappa \rho_{\text{BC}}(\mathbf{x}_\perp). \quad (4.1)$$

The case $\kappa = 0$ corresponds to the standard wounded-nucleon model [51], while $\kappa = 1$ would include the binary collisions only. The PHOBOS analysis [50] of the particle multiplicities yields $\kappa = 0.12$ at $\sqrt{s_{\text{NN}}} = 17$ GeV and $\kappa = 0.14$ at $\sqrt{s_{\text{NN}}} = 200$ GeV. Since the density profile from the binary collisions is steeper than from the wounded nucleons, increased values of κ yield steeper density profiles, which in turn result in steeper temperature profiles.

In our hydrodynamic code, the initial conditions are specified for the temperature profile which takes the form

$$T(\tau_i, \mathbf{x}_\perp) = T_S \left[s_i \frac{\rho(\mathbf{x}_\perp)}{\rho(0)} \right], \quad (4.2)$$

where $T_S(s)$ is the inverse function to the function $s(T)$, and s_i is the initial entropy at the center of the system. The initial central temperature T_i equals $T_S(s_i)$. Throughout this work, the initial time for the start of the hydrodynamic evolution is denoted by τ_i .

The wounded-nucleon and the binary-collisions densities in Eq. (4.2) are obtained from the optical limit of the Glauber model, which is a very good approximation for not too peripheral collisions [52]. The standard formulas are [51]

$$\begin{aligned} \rho_{\text{WN}}(\mathbf{x}_\perp) &= T_A \left(\frac{\mathbf{b}}{2} + \mathbf{x}_\perp \right) \left\{ 1 - \left[1 - \frac{\sigma_{\text{in}}}{A} T_A \left(-\frac{\mathbf{b}}{2} + \mathbf{x}_\perp \right) \right]^A \right\} \\ &+ T_A \left(-\frac{\mathbf{b}}{2} + \mathbf{x}_\perp \right) \left\{ 1 - \left[1 - \frac{\sigma_{\text{in}}}{A} T_A \left(\frac{\mathbf{b}}{2} + \mathbf{x}_\perp \right) \right]^A \right\} \end{aligned} \quad (4.3)$$

and

$$\rho_{\text{BC}}(\mathbf{x}_\perp) = \sigma_{\text{in}} T_A \left(\frac{\mathbf{b}}{2} + \mathbf{x}_\perp \right) T_A \left(-\frac{\mathbf{b}}{2} + \mathbf{x}_\perp \right). \quad (4.4)$$

In Eqs. (4.3) and (4.4) \mathbf{b} is the impact vector, σ_{in} is the nucleon-nucleon total inelastic cross section, and $T_A(x, y)$ is the nucleus thickness function

$$T_A(x, y) = \int dz \rho(x, y, z). \quad (4.5)$$

For RHIC energies we use the value $\sigma_{\text{in}} = 42$ mb, while for LHC we take $\sigma_{\text{in}} = 63$ mb. The function $\rho(r)$ in Eq. (4.5) is the nuclear density profile given by the Woods-Saxon function with the conventional choice of the parameters:

$$\begin{aligned} \rho_0 &= 0.17 \text{ fm}^{-3}, \\ r_0 &= (1.12A^{1/3} - 0.86A^{-1/3}) \text{ fm}, \\ a &= 0.54 \text{ fm}. \end{aligned} \quad (4.6)$$

The values of the atomic mass A are: 197 for RHIC (gold nuclei) and 208 for LHC (lead nuclei). The value of the impact parameter in Eqs. (4.3) and (4.4) depends on the considered centrality class.

Besides the initial temperature profile (4.2) we also specify the initial transverse flow profile,

$$\begin{aligned} v(\tau_i, r, \phi) &= \frac{H_0 r}{\sqrt{1 + H_0^2 r^2}}, \\ \alpha(\tau_i, r, \phi) &= 0. \end{aligned} \quad (4.7)$$

The results presented below are obtained with $H_0 = 0.001 \text{ fm}^{-1}$. The very small value of the parameter H_0 means that the system is practically at rest at the moment when the hydrodynamic evolution starts. However, nonzero H_0 improves the stability of the numerical method.

In our numerical calculations we use the adaptive method of lines in the way as it is implemented in the MATHEMATICA package. The ϕ and r directions are discretized, and the integration in time is treated as solving of the system of ordinary differential equations. Typically, we use grids with $\Delta r = 0.25 \text{ fm}$ in the r direction and $\Delta\phi = 6$ degrees in the ϕ direction. This method fails in the case where the shock waves are formed, however with our regular equation of state and the regular initial conditions such shocks are not present.

We stress that the shape of the initial condition (4.2) is important, as it determines the development of the radial and elliptic flow, thus affecting such observables as the p_T -spectra, v_2 , and the femtoscopic features. On qualitative grounds, sharper profiles lead to more rapid expansion. Several effects should be considered here. Firstly, as discussed in Ref. [3], hydrodynamics may start a bit later, when the profile is less eccentric than originally due to initial free-streaming of partons in the pre-hydro phase. On the other hand, statistical fluctuations in the distribution of the Glauber sources (wounded nucleons, binary collisions) [53, 54, 55, 56, 57, 58, 59] lead to a significant enhancement of the eccentricity, especially at low values of the impact parameter. Thus the initial eccentricity may in fact be smaller or larger than what follows from the application of the Glauber model. This contributes to the systematic model uncertainty at the level of about 10-20%. This uncertainty could only be reduced by the employment of a realistic model of the pre-hydrodynamic evolution. With this uncertainty in place, one should not expect or demand a better agreement with the physical observables than at the corresponding level of 10-20%.

The results obtained with the introduced here standard initial conditions are presented and discussed in Chapters 6 and 7.

4.2 Gaussian initial conditions

The situation described in the previous Section corresponds to the typical case where the hydrodynamic evolution is initiated from a source profile generated by the Glauber model, with the initial central temperature or energy serving as a free parameter. The initial density and possibly the initial flow profiles may be also provided by the early partonic dynamics, for instance by the Color Glass Condensate (CGC) [60, 61]. In practice, however, the theory of the partonic stage carries some uncertainty in its parameters, which influences our knowledge of the details of early dynamics. Having in mind such uncertainties we decided to try another class of the initial conditions, i.e., in our calculations we also include the case where the initial energy profiles in the transverse plane have the Gaussian shape.

The modified Gaussian parameterization of the initial energy density profile at

the initial proper time τ_i has the following form

$$\varepsilon(\mathbf{x}_\perp) = \varepsilon_i \exp\left(-\frac{x^2}{2a^2} - \frac{y^2}{2b^2}\right). \quad (4.8)$$

The energy density profile (4.8) determines the initial temperature profile that is used in the hydrodynamic code,

$$T(\tau_i, \mathbf{x}_\perp) = T_\varepsilon \left[\varepsilon_i \exp\left(-\frac{x^2}{2a^2} - \frac{y^2}{2b^2}\right) \right], \quad (4.9)$$

The initial central temperature $T(\tau_i, 0)$, which may depend on the centrality, is denoted by T_i and is a free parameter of our approach.

The results obtained with such initial conditions are presented and discussed in Sect. 8.1.

4.3 Free streaming

The very early start of hydrodynamics means that the matter equilibrates very fast. Such a short thermalization time is difficult to explain on the microscopical grounds and inspires hot discussion about the nature of matter produced at RHIC. To avoid the problem with the early thermalization we consider also the scenario where the hydrodynamic evolution is preceded by the free-streaming stage. In this version of our calculations we assume that partons behave as free particles in the proper time interval $0.25 \leq \tau \leq 1$ fm. At $\tau_i = 1$ fm the sudden equilibration takes place which is described with the help of the Landau matching conditions. The global picture is as follows: early phase (CGC) generating partons at time $\tau_0 = 0.25$ fm, partonic free streaming until $\tau_i = 1$ fm, hydrodynamic evolution until the freeze-out at temperature T_f , free streaming of hadrons and decay of resonances. We note that similar ideas have been described by Sinyukov et al. in Refs. [62, 63].

In the remaining part of this Section we describe in more detail the free-streaming stage. We assume that massless partons are formed at the initial proper time $\tau_0 = \sqrt{t_0^2 - z_0^2}$ and move along straight lines at the speed of light until the proper time when free streaming ends, $\tau = \sqrt{t^2 - z^2}$. We introduce the space-time rapidities

$$\eta_0 = \frac{1}{2} \log \frac{t_0 - z_0}{t_0 + z_0} \quad (4.10)$$

and

$$\eta_\parallel = \frac{1}{2} \log \frac{t - z}{t + z}. \quad (4.11)$$

Elementary kinematics [62] links the positions of a parton on the initial and final hypersurfaces and its four-momentum

$$p^\mu = (p_T \cosh y, p_T \cos \phi_p, p_T \sin \phi_p, p_T \sinh y), \quad (4.12)$$

where y and p_T are the parton's rapidity and transverse momentum:

$$\begin{aligned}\tau \sinh(\eta_{\parallel} - y) &= \tau_0 \sinh(\eta_0 - y), \\ x &= x_0 + \Delta \cos \phi_p, \quad y = y_0 + \Delta \sin \phi_p, \\ \Delta &= \tau \cosh(y - \eta_{\parallel}) - \sqrt{\tau_0^2 + \tau^2 \sinh^2(y - \eta_{\parallel})}.\end{aligned}\tag{4.13}$$

Thus the phase-space density of partons at the proper times τ_0 and τ are related

$$\begin{aligned}\frac{d^6 N}{dy d^2 p_T d\eta_{\parallel} dx dy} &= \int d\eta_0 dx_0 dy_0 \frac{d^6 N}{dy d^2 p_T d\eta_0 dx_0 dy_0} \times \\ &\delta\left(\eta_0 - y - \operatorname{arcsinh}\left[\frac{\tau}{\tau_0} \sinh(\eta_{\parallel} - y)\right]\right) \times \\ &\delta(x - x_0 - \Delta \cos \phi_p) \delta(y - y_0 - \Delta \sin \phi_p).\end{aligned}\tag{4.14}$$

In our approach we restrict ourselves to the boost-invariant systems, hence it is reasonable to assume the following factorized form of the initial distribution of partons,

$$\frac{d^6 N}{dy d^2 p_T d\eta_0 dx_0 dy_0} = n(x_0, y_0) F(y - \eta_0, p_T),\tag{4.15}$$

where n is the transverse density of partons obtained again from the GLISSANDO model, namely

$$n(x_0, y_0) = n_0 \exp\left(-\frac{x_0^2}{2a^2} - \frac{y_0^2}{2b^2}\right).\tag{4.16}$$

When the rapidity emission profile F is focused near $y = \eta_0$, for instance if we have $F \sim \exp[(y - \eta_0)^2 / (2\delta y^2)]$, with $\delta y \sim 1$, and if $\tau \gg \tau_0$, then the kinematic condition (4.13) effectively transforms it into

$$F \sim \exp\left(\frac{\operatorname{arcsinh}^2\left[\frac{\tau}{\tau_0} \sinh(y - \eta_{\parallel})\right]}{2\delta y^2}\right) \sim \delta(y - \eta_{\parallel}).\tag{4.17}$$

Then Eq. (4.14) yields

$$\frac{d^6 N}{dy d^2 p_T d\eta_{\parallel} dx dy} = n(x - \Delta\tau \cos \phi_p, y - \Delta\tau \sin \phi_p) \delta(y - \eta_{\parallel}) f(p_T),\tag{4.18}$$

where $\Delta\tau = \tau - \tau_0$ and $f(p_T)$ is the transverse momentum distribution. The energy-momentum tensor at the proper time τ , rapidity η_{\parallel} , and transverse position (x, y) is given by the formula

$$\begin{aligned}T^{\mu\nu} &= \int dy d^2 p_T \frac{d^6 N}{dy d^2 p_T d\eta_{\parallel} dx dy} p^{\mu} p^{\nu} \\ &= \frac{\varepsilon_0}{2\pi n_0} \int_0^{2\pi} d\phi_p n(x - \Delta\tau \cos \phi_p, y - \Delta\tau \sin \phi_p) \times \\ &\quad \begin{pmatrix} \cosh^2 \eta_{\parallel} & \cosh \eta_{\parallel} \cos \phi_p & \cosh \eta_{\parallel} \sin \phi_p & \cosh \eta_{\parallel} \sinh \eta_{\parallel} \\ \cosh \eta_{\parallel} \cos \phi_p & \cos^2 \phi_p & \cos \phi_p \sin \phi_p & \cos \phi_p \sinh \eta_{\parallel} \\ \cosh \eta_{\parallel} \sin \phi_p & \cos \phi_p \sin \phi_p & \sin^2 \phi_p & \sin \phi_p \sinh \eta_{\parallel} \\ \cosh \eta_{\parallel} \sinh \eta_{\parallel} & \cos \phi_p \sinh \eta_{\parallel} & \sin \phi_p \sinh \eta_{\parallel} & \sinh^2 \eta_{\parallel} \end{pmatrix},\end{aligned}\tag{4.19}$$

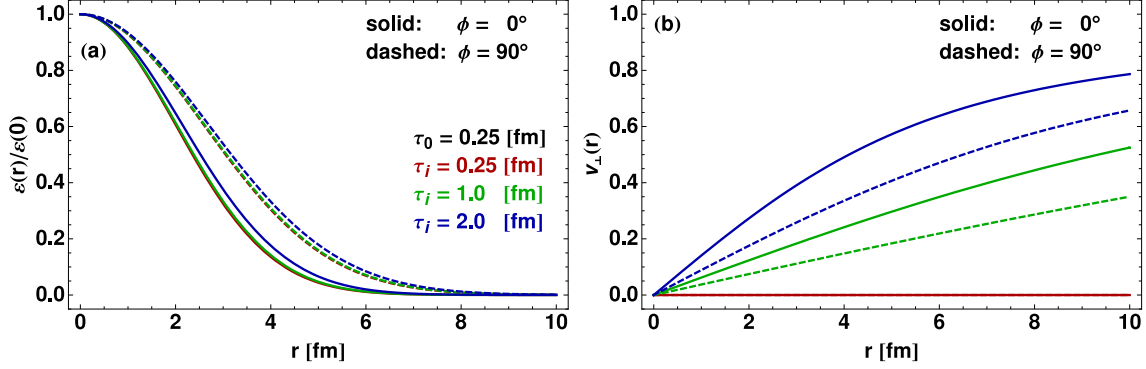


Figure 4.1: Sections of the energy-density profile ε (Gaussian-like curves) normalized to unity at the origin, and of the velocity profile $v_\perp = \sqrt{v_x^2 + v_y^2}$ (curves starting at the origin), cut along the x axis (solid lines) and y -axis (dashed lines). The initial profile is from Eq. (4.16) for centrality 20-40% at $\tau = \tau_0$. The ε profiles are for $\tau = \tau_0 = 0.25, 1$, and 2 fm, and the velocity profiles are for $\tau = 0.25, 1$ and 2 fm, all from bottom to top. We note that the flow is azimuthally asymmetric and stronger along the x axis.

where the factor $\varepsilon_0/(2\pi n_0)$ is a constant from the p_T integration¹ Due to boost invariance the further calculation may be carried for simplicity of notation at $\eta_\parallel = 0$. Next, we assume that at the proper time τ the system equilibrates rapidly. We thus use the Landau matching condition,

$$T^{\mu\nu}(x, y)u_\nu(x, y) = \varepsilon(x, y)g^{\mu\nu}u_\nu(x, y), \quad (4.20)$$

to determine the position dependent four-velocity of the fluid,

$$u^\mu(\tau, x, y) = \frac{1}{\sqrt{1 - v_\perp^2}}(1, v_x, v_y, 0) \quad (4.21)$$

and its position dependent energy density $\varepsilon(\tau, x, y)$, which is then identified with the energy-density profile. The obtained in this way the flow and energy profiles are used as an input for the hydrodynamic calculations. The time τ coincides with the starting time for hydrodynamics, $\tau = \tau_i$, and we again use the formula

$$T(\tau_i, \mathbf{x}_\perp) = T_\varepsilon[\varepsilon(\tau_i, 0, 0)] \quad (4.22)$$

to define the initial temperature profile in the hydrodynamic code. The initial central temperature $T_i = T_\varepsilon(\varepsilon_i)$ is again used as a free parameter (connected with the freedom of choosing ε_0).

The results of solving Eq. (4.20) with $T^{\mu\nu}$ from (4.19) for $\Delta\tau = 0.75$ fm and the initial profile (4.16) are shown in Fig. 4.1. The presented results correspond to the centrality class 20-40%. The curves normalized to unity at the origin, $r = 0$, show the sections along the x and y axes of the energy-density profile at the proper times τ_0

¹Note that the structure of Eq. (4.19) implies that for $\Delta = 0$ the initial energy density given by T^{00} and the initial parton density n have the same profiles in the transverse plane.

(no free streaming) and τ . Obviously, at τ_0 we find $\varepsilon(x, y) = \varepsilon_0 n(x, y)/n_0$. We note that the profile spreads out as the time progresses. Importantly, this effect is faster along the shorter axes, x . This is clearly indicated by the velocity profiles along the x and y axes (the curves starting from 0 at $r = 0$). Thus the flow generated by free streaming and sudden equilibration is azimuthally asymmetric. This asymmetry is also seen from the expansion in the parameters $\Delta\tau, x, y$, where straightforward algebra gives (for $x\Delta\tau \ll a^2$ and $y\Delta\tau \ll b^2$)

$$\mathbf{v}(x, y) = -\frac{\Delta\tau}{3} \frac{\nabla n(x, y)}{n(x, y)} = \frac{\Delta\tau}{3} \left(\frac{x}{a^2}, \frac{y}{b^2} \right). \quad (4.23)$$

The results of the hydrodynamic calculations preceded by the free-streaming stage are presented and discussed in Section 8.2.

Chapter 5

Freeze-out prescription

As the system expands, its density decreases and the mean free path of particles becomes larger and larger. When the average time between the collisions becomes compatible with the characteristic time of the system expansion, that is given approximately by the inverse of the divergence of four-velocity, $\tau_{\text{exp}} \sim (\partial_\mu u^\mu)^{-1}$, the hadrons decouple and may be regarded as free particles. The hydrodynamic stage of the evolution of matter is then changed into the free streaming of hadrons which are later registered by various detectors. The transition from strongly interacting hydrodynamic system into the non-interacting system of hadrons is called the freeze-out process. In fact one can distinguish two types of freeze-outs: the chemical freeze-out (when the inelastic processes stop and the hadronic abundances are frozen) and the kinetic freeze-out (when all interactions stop and the momentum spectra are frozen). Of course, the kinetic freeze-out may be regarded as the true freeze-out, after which all interactions cease. The concept of the chemical freeze-out is however very useful since this is the stage when the hadronic abundances are fixed (by definition, the subsequent evolution is dominated by elastic collisions which do not change the hadronic yields).

In our approach we use the simplification that the two freeze-outs discussed above happen at the same time. This approach is known as the single-freeze-out assumption and several earlier studies showed that it leads to the correct description of the data [30, 64, 65, 66, 67, 68]. Of course in the hydrodynamic approach the freeze-out happens locally, i.e., at different times for different space positions. In our studies we assume that freeze-out takes place at a given final temperature T_f . At the beginning of the evolution the hadrons are emitted usually from the edge (surface) of the system where the temperature is always low. At the end of the evolution, the hadrons are emitted mainly from the whole volume, since the temperature eventually drops down to T_f everywhere due to the hydrodynamic expansion.

5.1 Cooper-Frye formula

The collection of the spacetime points where the freeze-out process takes place is called the freeze-out hypersurface. This hypersurface is a three dimensional manifold

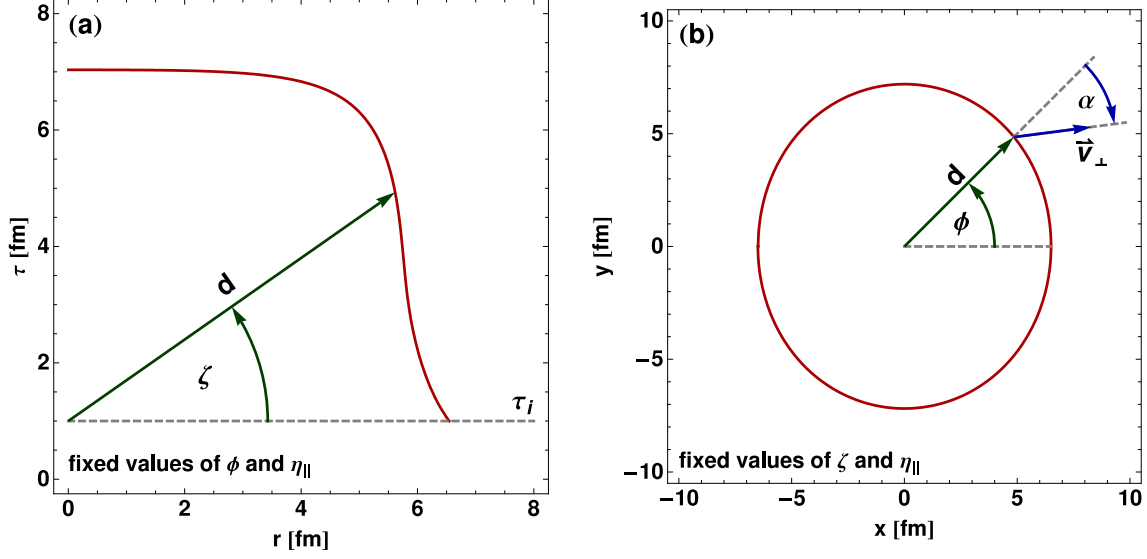


Figure 5.1: Parameterization of the freeze-out hypersurface. The part (a) represents the view in the $\tau - r$ plane with the fixed values of ϕ and η_{\parallel} . The part (b) shows the view in the $x - y$ plane with the fixed values of ζ and η_{\parallel} .

in the four-dimensional Minkowski space. The approach which is used to calculate the spectra of the emitted hadrons is based on the Cooper-Frye formula [69, 70]

$$\frac{dN}{dyd^2p_{\perp}} = \int d\Sigma_{\mu} p^{\mu} f(p \cdot u). \quad (5.1)$$

In Eq. (5.1) $d\Sigma_{\mu}$ is the element of the freeze-out hypersurface and f is the equilibrium distribution function depending on the scalar product of the particle four-momentum p^{μ} and the fluid four-velocity u^{μ} . In our approach the form of the freeze-out hypersurface is delivered by the hydrodynamic code. The criterion $T = T_f$ is used to find the appropriate space-time points, whose positions are parameterized in the following general way

$$\begin{aligned} t &= [\tau_i + d(\phi, \zeta, \eta_{\parallel}) \sin \zeta] \cosh \eta_{\parallel}, & z &= [\tau_i + d(\phi, \zeta, \eta_{\parallel}) \sin \zeta] \sinh \eta_{\parallel}, \\ x &= d(\phi, \zeta, \eta_{\parallel}) \cos \zeta \cos \phi, & y &= d(\phi, \zeta, \eta_{\parallel}) \cos \zeta \sin \phi. \end{aligned} \quad (5.2)$$

Here ϕ is the standard azimuthal angle in the $y - x$ plane, while the variable η_{\parallel} is the space-time rapidity defined as

$$\eta_{\parallel} = \frac{1}{2} \ln \frac{t + z}{t - z} = \tanh^{-1} \left(\frac{z}{t} \right). \quad (5.3)$$

The parameterization (5.2) yields the compact expressions for the proper time τ and the transverse distance r ,

$$\begin{aligned} \tau - \tau_i &= \sqrt{t^2 - z^2} - \tau_i = d(\phi, \zeta, \eta_{\parallel}) \sin \zeta, \\ r &= \sqrt{x^2 + y^2} = d(\phi, \zeta, \eta_{\parallel}) \cos \zeta. \end{aligned} \quad (5.4)$$

For fixed ϕ and η_{\parallel} the quantity $d(\phi, \zeta, \eta_{\parallel})$ is the distance between the hypersurface point with coordinates $(\phi, \zeta, \eta_{\parallel})$ and the spacetime point $(\tau = \tau_i, x = 0, y = 0)$, see Fig. 5.1. The variable ζ , restricted to the range $0 \leq \zeta \leq \pi/2$, is an angle in the $\tau - r$ space. We have introduced the angle ζ because in most cases the freeze-out curves in the $\tau - r$ plane may be treated as functions of this parameter. The use of the transverse distance r is inconvenient, since very often two freeze-out points correspond to one value of r .

If the parameterization of the freeze-out hypersurface in terms of the variables ϕ , ζ , and η_{\parallel} is given, then the element of the freeze-out hypersurface may be obtained from the formula known from the differential geometry

$$d\Sigma_{\alpha} = \epsilon_{\alpha\beta\gamma\delta} \begin{vmatrix} \frac{\partial x^{\beta}}{\partial \phi} & \frac{\partial x^{\beta}}{\partial \zeta} & \frac{\partial x^{\beta}}{\partial \eta_{\parallel}} \\ \frac{\partial x^{\gamma}}{\partial \phi} & \frac{\partial x^{\gamma}}{\partial \zeta} & \frac{\partial x^{\gamma}}{\partial \eta_{\parallel}} \\ \frac{\partial x^{\delta}}{\partial \phi} & \frac{\partial x^{\delta}}{\partial \zeta} & \frac{\partial x^{\delta}}{\partial \eta_{\parallel}} \end{vmatrix} d\phi d\zeta d\eta_{\parallel}, \quad (5.5)$$

where $\epsilon_{\alpha\beta\gamma\delta}$ is the totally antisymmetric tensor with $\epsilon_{0123} = +1$. The direct differentiation gives:

$$\begin{aligned} d\Sigma^0 &= d \cos \zeta \left[(\tau_i + d \sin \zeta) \left(d \sin \zeta - \frac{\partial d}{\partial \zeta} \cos \zeta \right) \cosh \eta_{\parallel} + \frac{\partial d}{\partial \eta_{\parallel}} \sinh \eta_{\parallel} \right], \\ d\Sigma^1 &= -d (\tau_i + d \sin \zeta) \left[\left(d \cos \zeta + \frac{\partial d}{\partial \zeta} \sin \zeta \right) \cos \zeta \cos \phi + \frac{\partial d}{\partial \phi} \sin \phi \right], \\ d\Sigma^2 &= -d (\tau_i + d \sin \zeta) \left[\left(d \cos \zeta + \frac{\partial d}{\partial \zeta} \sin \zeta \right) \cos \zeta \sin \phi + \frac{\partial d}{\partial \phi} \cos \phi \right], \\ d\Sigma^3 &= d \cos \zeta \left[(\tau_i + d \sin \zeta) \left(d \sin \zeta - \frac{\partial d}{\partial \zeta} \cos \zeta \right) \sinh \eta_{\parallel} + \frac{\partial d}{\partial \eta_{\parallel}} \cosh \eta_{\parallel} \right]. \end{aligned} \quad (5.6)$$

With Eqs. (5.6) and the standard definition of the four-momentum expressed in terms of the rapidity and transverse momentum,

$$p^{\mu} = (m_T \cosh y, p_T \cos \phi_p, p_T \sin \phi_p, m_T \sinh y), \quad (5.7)$$

where $m_T = \sqrt{m^2 + p_T^2}$ is the transverse mass, we find the explicit form of the Cooper-Frye integration measure [69]

$$\begin{aligned} d\Sigma_{\mu} p^{\mu} &= d (\tau_i + d \sin \zeta) \left[d \cos \zeta (m_T \sin \zeta \cosh (\eta_{\parallel} - y) + p_T \cos \zeta \cos (\phi - \phi_p)) \right. \\ &\quad + \frac{\partial d}{\partial \zeta} \cos \zeta (-m_T \cos \zeta \cosh (\eta_{\parallel} - y) + p_T \sin \zeta \cos (\phi - \phi_p)) \\ &\quad \left. + \frac{\partial d}{\partial \phi} p_T \sin (\phi - \phi_p) + \frac{\partial d}{\partial \eta_{\parallel}} m_T \cot \zeta \sinh (\eta_{\parallel} - y) \right] d\eta_{\parallel} d\phi d\zeta. \end{aligned} \quad (5.8)$$

This equation, when used in the Cooper-Frye formula [69], leads to the six- dimensional particle density at freeze-out

$$\begin{aligned}
& \frac{dN}{dy d\phi_p p_T dp_T d\eta_{\parallel} d\phi d\zeta} \\
&= \frac{g}{(2\pi)^3} d (\tau_i + d \sin \zeta) \left[d \cos \zeta (m_T \sin \zeta \cosh (\eta_{\parallel} - y) + p_T \cos \zeta \cos (\phi - \phi_p)) \right. \\
&+ \frac{\partial d}{\partial \zeta} \cos \zeta (-m_T \cos \zeta \cosh (\eta_{\parallel} - y) + p_T \sin \zeta \cos (\phi - \phi_p)) \\
&+ \left. \frac{\partial d}{\partial \phi} p_T \sin (\phi - \phi_p) \right] \\
&\times \left\{ \exp \left[\frac{\beta}{\sqrt{1 - v_{\perp}^2}} (m_T \cosh (y - \eta_{\parallel}) - p_T v_{\perp} \cos (\phi + \alpha - \phi_p)) - \beta \mu \right] \pm 1 \right\}^{-1}.
\end{aligned} \tag{5.9}$$

In the transition from (5.8) to (5.9) we used the assumption of boost-invariance and removed the term $\partial d / \partial \eta_{\parallel}$ – for boost-invariant systems the function d depends only on ϕ and ζ . The last line in (5.9) contains the equilibrium statistical distribution function, with -1 for bosons and $+1$ for fermions. The argument is the Lorentz-invariant product $p^{\mu} u_{\mu}$. The parameter $\beta = 1/T$ is the inverse temperature and g denotes the spin degeneracy factor. The four-velocity field has been expressed in terms of the transverse flow $v_{\perp}(\phi, \zeta)$ and the dynamical angle $\alpha(\phi, \zeta)$ which depend on the space-time positions on the freeze-out hypersurface.

Although in the hydrodynamic evolution we neglected the effects of the chemical potential μ , it is introduced in the generation of the particles at freeze-out. Thus, the equilibrium distributions include the term

$$\mu = \mu_B B + \mu_S S + \mu_{I_3} I_3, \tag{5.10}$$

with B , S , and I_3 denoting the baryon number, strangeness, and isospin of the particle. The baryonic, strange, and isospin chemical potentials assume the values: $\mu_B = 28.5$ MeV, $\mu_S = 9$ MeV, $\mu_{I_3} = -0.9$ MeV at the highest RHIC energies [30], and $\mu_B = 0.8$ MeV and $\mu_S = \mu_{I_3} = 0$ MeV at the LHC [33].

5.2 Calculation of observables

In order to calculate the physical observables we first run our hydrodynamic code and extract the functions describing the freeze-out hypersurface and flow: $d = d(\phi, \zeta)$, $v_{\perp} = v_{\perp}(\phi, \zeta)$, and $\alpha = \alpha(\phi, \zeta)$. In the next step these functions are used as input for the THERMINATOR[27] code, which generates, according to the formula (5.9), the distributions of the primordial particles. The primordial particles include the stable hadrons as well as all hadronic resonances. The resonances decay through

strong, electromagnetic, or weak interactions at the random proper time controlled by the particle life-time, and at the location following from the kinematics. As the final result we obtain the stable particle distributions including the feeding from the resonance decays. Since the memory on all decays is kept, one may apply the experimental cuts or the weak-decay feeding policy, which facilitates the more accurate comparison of the model to the data. For example, one may extract easily the model proton spectrum which does not include the feeding from the Λ decays. The momentum distribution functions are obtained by integrating over ϕ , η_{\parallel} , and ζ ,

$$\frac{dN}{dyd^2p_T} = \int_{-\infty}^{\infty} d\eta_{\parallel} \int_0^{2\pi} d\phi \int_0^{\pi/2} d\zeta \frac{dN}{dyd\phi_p p_T dp_T d\eta_{\parallel} d\phi d\zeta}. \quad (5.11)$$

For cylindrically asymmetric collisions and midrapidity, $y = 0$, the transverse-momentum spectrum has the following expansion in the azimuthal angle of the emitted particles

$$\frac{dN}{dyd^2p_T} = \frac{dN}{dy 2\pi p_T dp_T} (1 + 2v_2(p_T) \cos(2\phi_p) + \dots). \quad (5.12)$$

Equation (5.12) defines the elliptic flow coefficient v_2 .

The well-known problem of the freeze-out description in the Cooper-Frye formulation is that the hypersurface from hydrodynamics typically contains a non-causal piece, where particles are emitted back to the hydrodynamic region [71]. In our approach we follow the usual strategy of including only that part of the hypersurface where $d\Sigma_{\mu}p^{\mu} \geq 0$. To estimate the effect from the non-causal part we compute the ratio of particles flowing backwards (*i.e.* where $d\Sigma_{\mu}p^{\mu} < 0$) to all particles. For the cases studied in the following sections we find this ratio to be a fraction of a percent. Such very small values show that the known conceptual problem is not of practical importance for our study.

The correlation function for identical pions is obtained with the two-particle Monte-Carlo method discussed in detail in Ref. [72, 73]. In this approach the evaluation of the correlation function is reduced to the calculation of the following expression

$$C(\mathbf{q}, \mathbf{k}) = \frac{\sum_i \sum_{j \neq i} \delta_{\Delta}(\mathbf{q} - \mathbf{p}_i + \mathbf{p}_j) \delta_{\Delta}(\mathbf{k} - \frac{1}{2}[\mathbf{p}_i + \mathbf{p}_j]) |\Psi(\mathbf{k}^*, \mathbf{r}^*)|^2}{\sum_i \sum_{j \neq i} \delta_{\Delta}(\mathbf{q} - \mathbf{p}_i + \mathbf{p}_j) \delta_{\Delta}(\mathbf{k} - \frac{1}{2}[\mathbf{p}_i + \mathbf{p}_j])}, \quad (5.13)$$

where δ_{Δ} denotes the box function

$$\delta_{\Delta}(\mathbf{p}) = \begin{cases} 1, & \text{if } |p_x| \leq \frac{\Delta}{2}, |p_y| \leq \frac{\Delta}{2}, |p_z| \leq \frac{\Delta}{2} \\ 0, & \text{otherwise.} \end{cases} \quad (5.14)$$

In the numerator of Eq. (5.13) we include the sum of the squares of modules of the wave function calculated for all pion pairs with the relative momentum \mathbf{q} (we use

the bin resolution $\Delta = 5$ MeV) and the pair average momentum \mathbf{k} . For non-central collisions we only provide azimuthally integrated HBT radii. For each pair the wave function $\Psi(\mathbf{k}^*, \mathbf{r}^*)$, including the Coulomb interaction, is calculated in the rest frame of the pair; \mathbf{k}^* and \mathbf{r}^* denote the relative momentum and the relative distance in the pair rest frame, respectively. In the denominator of Eq. (5.13) we put the number of pairs with the relative momentum \mathbf{q} and the average momentum \mathbf{k} . The correlation function (5.13) is then expressed with the help of the Bertsch-Pratt coordinates $k_T, q_{\text{out}}, q_{\text{side}}, q_{\text{long}}$ and approximated by the Bowler-Sinyukov formula [74, 75]

$$C(\mathbf{q}, \mathbf{k}) = (1 - \lambda) + \lambda K_{\text{coul}}(q_{\text{inv}}) \times \\ \times \left[1 + \exp \left(-R_{\text{out}}^2 q_{\text{out}}^2 - R_{\text{side}}^2 q_{\text{side}}^2 - R_{\text{long}}^2 q_{\text{long}}^2 \right) \right], \quad (5.15)$$

where $K_{\text{coul}}(q_{\text{inv}})$ with $q_{\text{inv}} = 2k^*$ is the squared Coulomb wave function integrated over a static Gaussian source. We use, following the STAR procedure [76], the static Gaussian source characterized by the widths of 5 fm in all three directions. Four k_T bins, $(0.15 - 0.25)$, $(0.25 - 0.35)$, $(0.35 - 0.45)$, and $(0.45 - 0.60)$ GeV, are considered. The 3-dimensional correlation function with the exact treatment of the Coulomb interaction is then fitted with this approximate formula and the HBT radii R_{out} , R_{side} , and R_{long} are obtained. They can be compared directly to the experimental radii.

Chapter 6

Soft-hadronic observables at RHIC

In this Section we apply our model to describe soft hadron production in the relativistic heavy-ion collisions at the highest RHIC energy, $\sqrt{s_{NN}} = 200$ GeV. We analyze the data delivered by the PHENIX [77, 78] and STAR Collaborations [76]. We consider the most central events, defined by the centrality class $c = 0 - 5\%$, where we use the impact parameter $b = 2.26$ fm. We also use the data from the centrality classes $c = 20 - 30\%$ (transverse-momentum spectra and the HBT radii) and $c = 20 - 40\%$ (elliptic flow), for which we take (for simplicity) the same value of the impact parameter, $b = 7.16$ fm.

The link between the centrality class and the impact parameter involves the total Au+Au inelastic cross section. To a very good accuracy for not-too-peripheral collisions we may use the formula [79]

$$\langle c \rangle \simeq \frac{\pi b^2}{\sigma_{\text{in}}^{\text{AuAu}}}. \quad (6.1)$$

The total inelastic Au+Au cross section $\sigma_{\text{in}}^{\text{AuAu}}$ is not directly measured. Typically, it is obtained from Glauber simulations and carries model uncertainties [52]. With total inelastic pp cross section $\sigma_{\text{in}} = 42$ mb and for gold nuclei used at RHIC, the GLISSANDO Monte-Carlo Glauber simulation [57] gives $\sigma_{\text{in}}^{\text{AuAu}} \simeq 6.4$ b, so $b = 2.26$ fm for $\langle c \rangle = 2.5\%$ and $b = 7.16$ fm for $\langle c \rangle = 25\%$.

6.1 Central collisions

First, we consider the centrality class 0 - 5% with the corresponding value of the impact parameter $b = 2.26$ fm. The in-plane and out-of-plane freeze-out curves are defined as the intersections of the freeze-out hypersurface with the planes $y = 0$ ($\phi = 0^\circ$) and $x = 0$ ($\phi = 90^\circ$). They are obtained with the initial starting time for hydrodynamics $\tau_i = 1$ fm, the initial central temperature $T_i = 320$ MeV, the final (freeze-out) temperature $T_f = 150$ MeV, and are shown in Fig. 6.1. The two freeze-out curves practically overlap, indicating that the expansion of the system is almost azimuthally symmetric in the transverse plane. This feature is certainly expected for the almost

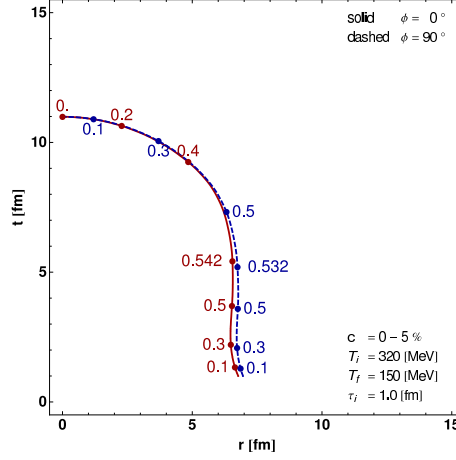


Figure 6.1: In-plane and out-of-plane freeze-out curves, i.e., the intersections of the freeze-out hypersurface with the planes $y = 0$ ($\phi = 0^\circ$) and $x = 0$ ($\phi = 90^\circ$), obtained for central RHIC collisions; $c = 0 - 5\%$, $b = 2.26$ fm, $\tau_i = 1.0$ fm, $T_i = 320$ MeV, and $T_f = 150$ MeV. The two curves overlap, indicating that the system at freeze-out is almost azimuthally symmetric in the transverse plane.

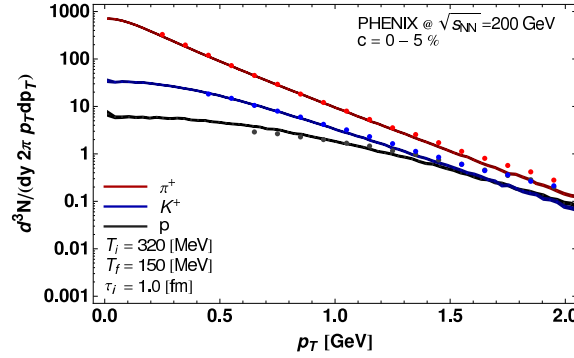


Figure 6.2: Transverse-momentum spectra of π^+ , K^+ , and protons. The PHENIX experimental results [77] for Au+Au collisions at $\sqrt{s_{NN}} = 200$ GeV and the centrality class 0-5% (points) are compared to the model calculations (solid lines) with the same parameters as in Fig. 6.1.

central collisions, where the impact parameter is very small. We note that the shape of the isotherms is consistent with the result presented in Fig. 2 of Ref. [80], where the same decoupling temperature of 150 MeV was considered.

In Fig. 6.2 we present our results for the hadron transverse-momentum spectra with the same values of the parameters. The dots show the PHENIX data [77] for positive pions, positive kaons, and protons, while the solid lines show the results obtained from our hydrodynamic code linked to THERMINATOR[27]. Our model describes the data well up to the transverse-momentum values of about 1.5 GeV. For larger values of p_T the model underpredicts the data. This effect may be explained

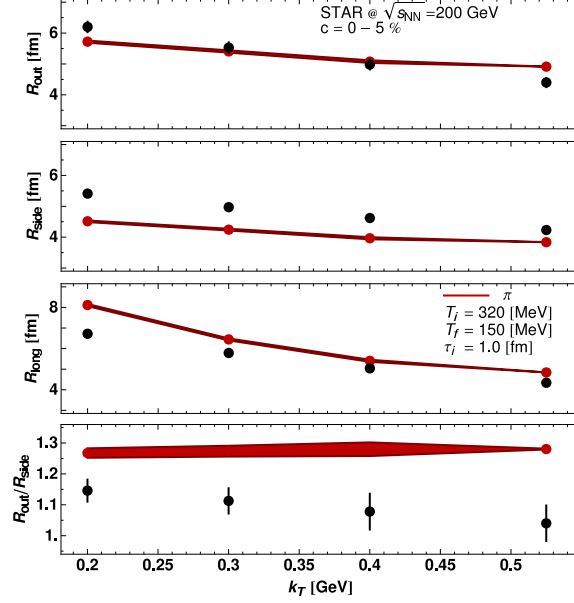


Figure 6.3: The pionic HBT radii plotted as functions of the average transverse momentum of the pair compared to the STAR data [76] at the centrality 0-5%. The calculation uses the two-particle method and includes the Coulomb effects. The values of the model parameters are the same as in Fig. 6.1.

by the presence of the semi-hard processes, not included in our approach.

In our approach, the values of T_i and b control the overall normalization. On the other hand, the value of the freeze-out temperature T_f determines mainly the relative normalization and the slopes of the spectra. We note that the correct slope for the pions and kaons is recovered at a relatively high value of T_f . This is possible, since the spectra of the observed hadrons contain the contributions from all well established hadronic resonances. This single-freeze-out picture [28, 64, 65], where the same temperature is used to describe the ratios of hadronic abundances and the spectra, was first tested for hadronic spectra in Ref. [64], see also [81, 66]. We note that the value $T_f = 150$ MeV agrees with the recent results obtained in the framework of the single-freeze-out model in Ref. [67]. In the calculation of the proton spectra, in order to be consistent with the PHENIX experimental procedure, we removed the protons coming from the Λ decays.

In Fig. 6.3 the model results and the STAR data [76] for the HBT radii are presented. Again, for the same values of the parameters, a quite reasonable agreement is found. Discrepancies at the level of 10-15% are observed in the behavior of the R_{side} , which is too small, and R_{long} , which is too large, probably due to the assumption of strict boost invariance. The ratio $R_{out}/R_{side} \simeq 1.25$ is larger than one, which is a typical discrepancy of hydrodynamic studies. Nevertheless, when compared to other hydrodynamic calculations, our ratio R_{out}/R_{side} is significantly closer to the experimental value. The ratio is almost constant as a function of k_T , contrary to the decrease observed in the data.

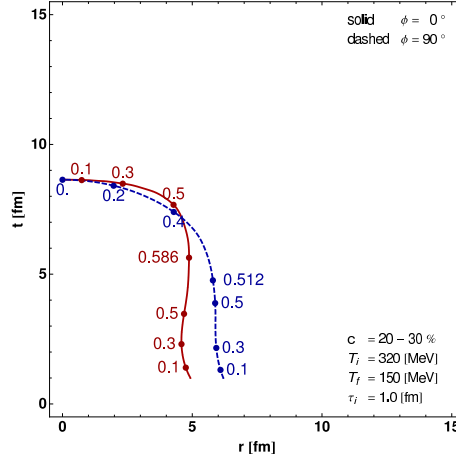


Figure 6.4: The freeze-out curves for $c = 20 - 30\%$, $\tau_i = 1.0$ fm, $T_i = 320$ MeV, $T_f = 150$ MeV, and $b = 7.16$ fm. The solid line describes the in-plane profile, while the dashed line describes the out-of-plane profile.

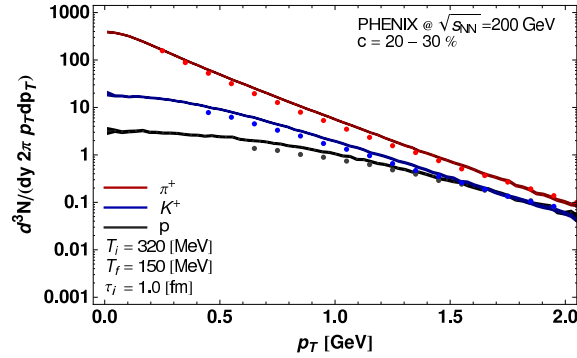


Figure 6.5: Transverse-momentum spectra of π^+ , K^+ , and protons. The PHENIX experimental results [77] for Au+Au collisions at $\sqrt{s_{NN}} = 200$ GeV and the centrality class 20-30% (points) are compared to the model calculations (solid lines). The values of the model parameters are the same as in Fig. 6.4.

6.2 Non-central collisions

Next, we consider the centrality classes 20 - 30% and 20 - 40%. The data are compared with the model results obtained with the impact parameter $b = 7.16$ fm. The values of the initial central temperature and the final temperature are the same as in the case of the central collisions, i.e., $T_i = 320$ MeV and $T_f = 150$ MeV. The two freeze-out curves are shown in Fig. 6.4. We observe that the out-of-plane profile is wider than the in-plane profile. This difference indicates that the system is elongated along the y axis at the moment of freeze-out. This feature is in qualitative agreement with the HBT measurements of the azimuthal dependence of R_{side} . The comparison of the experimental and model transverse-momentum spectra is

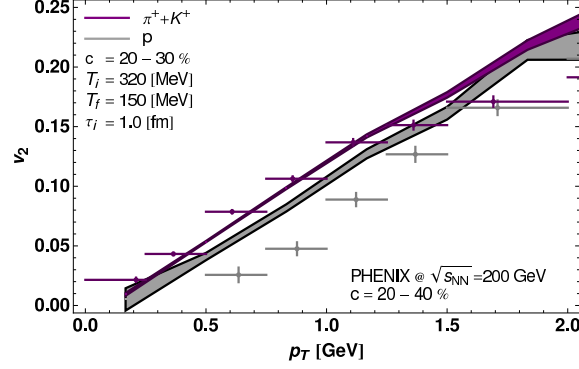


Figure 6.6: The elliptic flow coefficient v_2 . The values measured by PHENIX [78] at $\sqrt{s_{NN}} = 200$ GeV and the centrality class 20-40% are indicated by the upper (pions + kaons) and lower (protons) points, with the horizontal bars indicating the p_T bin. The corresponding model calculations are indicated by the solid lines, with the bands displaying the statistical error of the Monte-Carlo method. The parameters are the same as in Fig. 6.4.

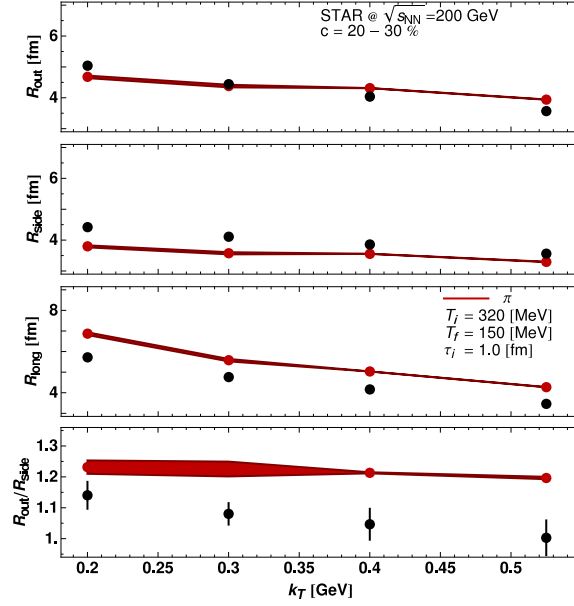


Figure 6.7: The pionic HBT radii plotted as functions of the average transverse momentum of the pair compared to the STAR data [76] at centrality 20-30%. As in the case of the central collisions, the calculation uses the two-particle method and includes the Coulomb effects. The values of the model parameters are the same as in Fig. 6.4.

presented in Fig. 6.5. In this case we also find a reasonable agreement between the data and the model results.

In Fig. 6.6 the model results and the PHENIX data [78] on the elliptic flow coefficient $v_2(p_T)$ are compared. We observe that the v_2 of pions+kaons agrees with

the data. Taking into account the uncertainty in the initial eccentricity, discussed in Sect. 4.1, which is at the level of 10-20%, the obtained agreement is reasonable. On the other hand, the model prediction for proton v_2 is too large. The discrepancy is probably caused by the final-state elastic interactions, not included in our approach [82].

The HBT radii for non-central RHIC collisions are shown in Fig. 6.7. Similarly to the central collisions, we observe that R_{side} is slightly too small and R_{long} is slightly too large. Still, the ratio $R_{\text{out}}/R_{\text{side}}$ is very close to the data. Comparing our values of R_{side} with other hydrodynamic calculations we find that our values are larger. This effect is caused by the halo of decaying resonances which increases the system size by about 1 fm, see Ref. [72].

Chapter 7

Predictions for LHC

We expect that the increase of the initial beam energy from $\sqrt{s_{NN}} = 200$ GeV at RHIC to $\sqrt{s_{NN}} = 5.5$ TeV at LHC results essentially in a higher initial temperature T_i used as the input for the hydrodynamic calculation (in the midrapidity region studied here). Therefore, to make predictions for the collisions at the LHC energies we use a set of values for T_i which are higher than those used at RHIC, namely, $T_i = 400, 450$, and 500 MeV. Of course, it is not obvious which value of T_i will be realized at LHC. Estimates based on extrapolations [83] suggest an increase of the multiplicity by a factor of 2 compared to the highest RHIC energies, which would favor T_i around 400 MeV. However, to investigate a broader range of possibilities, we take into account much higher temperatures as well. In the case of LHC we also use a larger value of the nucleon-nucleon cross section in the definition of the initial conditions ($\sigma_{in} = 63$ mb, $\kappa = 0.2$, $A = 208$) and different values of the chemical potentials in the hadronization made by **THERMINATOR** ($\mu_B = 0.8$ MeV and $\mu_s = \mu_{I_3} = 0$). The changes of σ_{in} and the nuclear profile imply that for LHC we use $b = 2.4$ fm for $c = 2.5\%$ and $b = 7.6$ fm for $c = 25\%$.

In Tables 7.1 and 7.2 we list our results for the following quantities: the total π^+ multiplicity dN/dy , the inverse-slope parameter for pions λ , the pion+kaon elliptic flow v_2 at $p_T = 1$ GeV, and the three HBT radii calculated at the pion pair momentum $k_T = 300$ MeV. The inverse-slope parameter given in Tables 7.1 and 7.2 is obtained from the formula

$$\lambda = - \left[\frac{d}{dp_T} \ln \left(\frac{dN_\pi}{2\pi p_T dp_T dy} \right) \right]^{-1}. \quad (7.1)$$

The tables show several expected qualitative features. Obviously, as the initial temperature increases, the multiplicity grows. This is due a larger initial entropy, which causes a larger size of the freeze-out hypersurface. We find that the following approximate parameterizations work very well for the multiplicity of π^+ at LHC for the two considered centrality cases:

$$\begin{aligned} \frac{dN}{dy} &= 12000 (T_i/\text{GeV})^{3.4}, \quad (b = 2.4 \text{ fm}) \\ \frac{dN}{dy} &= 6000 (T_i/\text{GeV})^{3.4}, \quad (b = 7.6 \text{ fm}). \end{aligned} \quad (7.2)$$

The power 3.4 works remarkably well. This behavior reflects the dependence of the initial entropy on T as shown in top left panel of Fig. 2.2 of Chapter 2, where for the relevant temperature range of 300 – 500 MeV we have the approximate scaling $s/T^3 \sim T^{0.4}$.

Similarly, for the slopes in the studied domain we have

$$\begin{aligned}\lambda(1 \text{ GeV}) &= 0.639 T_i + 0.033 \text{ GeV}, \quad (b = 2.4 \text{ fm}) \\ \lambda(1 \text{ GeV}) &= 0.661 T_i + 0.033 \text{ GeV}, \quad (b = 7.6 \text{ fm}).\end{aligned}\tag{7.3}$$

The HBT radii increase rather moderately with T_i , as can be seen from the tables.

T_i [MeV]	$\frac{dN}{dy}$	λ [MeV]	R_{side} [fm]	R_{out} [fm]	R_{long} [fm]
320	274	237	4.2	5.4	6.5
400	543	288	5.2	5.9	7.7
450	802	320	5.6	6.1	8.2
500	1136	352	6.0	6.2	8.8

Table 7.1: Central collisions at RHIC corresponding to the results from Chapter 6.1 (the second row) and LHC (the three lower rows): A set of our results obtained for four different values of the initial temperature: $T_i = 320, 400, 450$, and 500 MeV. The columns contain the following information: dN/dy – the total pion multiplicity (positive pions only), λ – the inverse-slope parameter for positive pions at $p_T = 1$ GeV, $R_{\text{side}}, R_{\text{out}}, R_{\text{long}}$ – the three HBT radii calculated at the average momentum $k_T = 300$ MeV.

T_i [MeV]	$\frac{dN}{dy}$	λ [MeV]	$v_2^{\pi+K}$	R_{side} [fm]	R_{out} [fm]	R_{long} [fm]
320	152	244	0.14	3.6	4.5	5.6
400	272	299	0.16	4.2	4.5	6.2
450	401	331	0.16	4.6	4.6	6.7
500	569	363	0.15	5.2	4.9	7.4

Table 7.2: Non-central collisions at RHIC corresponding to the results from Chapter 6.2 (the second row) and LHC (the three lower rows): The same quantities shown as in Table 7.1 with the additional information on the pion elliptic flow v_2 at $p_T = 1$ GeV.

7.1 Central collisions

In the following Sections we show more details, discussing the spectra, v_2 , and the HBT radii obtained for the initial temperature $T_i = 400, 450$ and 500 MeV.

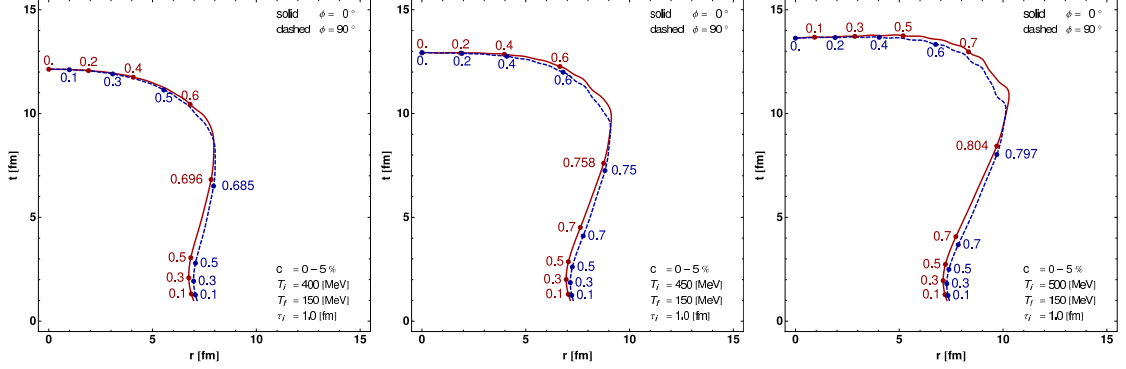


Figure 7.1: The freeze-out curves for central LHC collisions with $c = 0 - 5\%$, $b = 2.4$ fm, $\tau_i = 1.0$ fm for three initial temperatures $T_i = 400, 450$ and 500 MeV, and $T_f = 150$ MeV. Similarly to the central RHIC collisions, the two curves overlap indicating that the system at freeze-out is symmetric in the transverse plane.

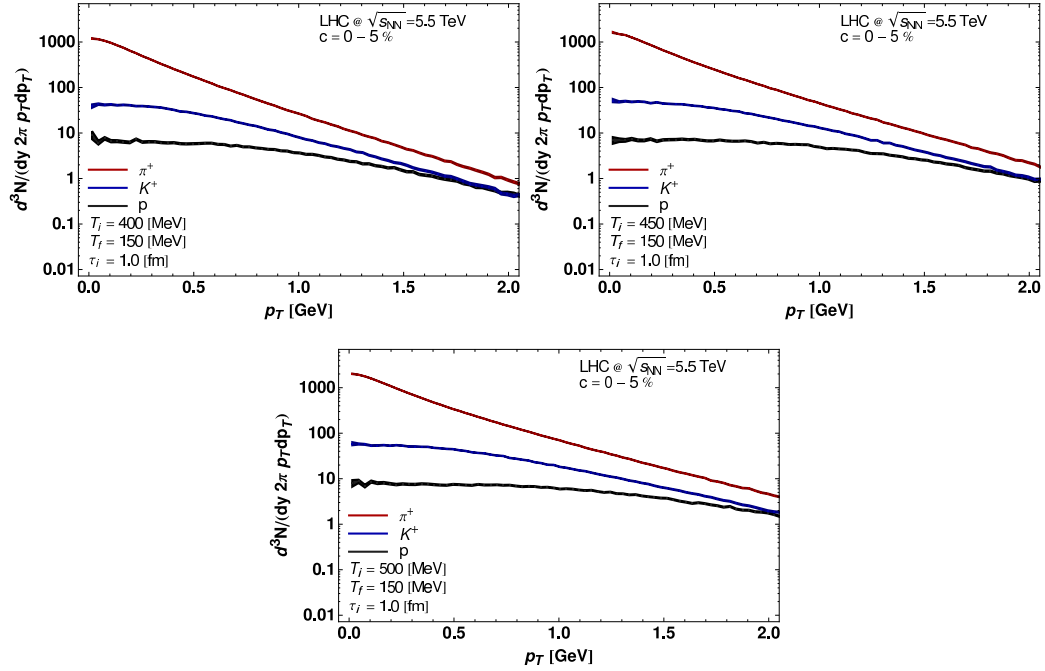


Figure 7.2: The model results for the transverse-momentum spectra of π^+ , K^+ , and protons. The values of the model parameters are the same as in Fig. 7.1.

In Fig. 7.1 we show the freeze-out curves obtained from our hydrodynamic code with $T_i = 400, 450$ and 500 MeV. Comparing to the corresponding central RHIC collisions with $T_i = 320$ MeV from Fig. 6.1, we observe that the difference in the initial temperature results in the longer time of the hydrodynamic expansion and a larger transverse size (both increase by about 3 fm). On the other hand, similarly to the RHIC results, we find that the two freeze-out profiles overlap, hence the system

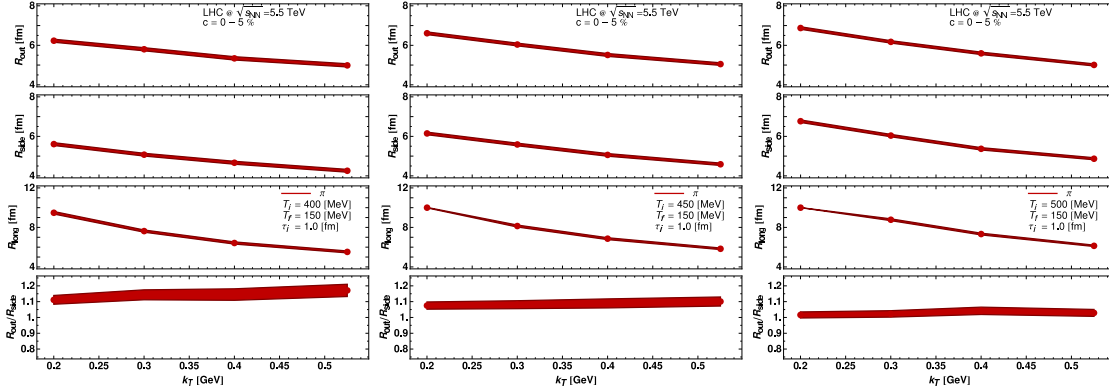


Figure 7.3: The model results for the pionic HBT radii. The calculation uses the two-particle method and includes the Coulomb effects. The values of the model parameters are the same as in Fig. 7.1.

at freeze-out is, as expected, azimuthally symmetric in the transverse plane. We also note that the shape of the isotherms is consistent with the result presented in Fig. 4 of Ref. [80].

In Fig. 7.2 we give the model transverse-momentum spectra of hadrons. Compared to the RHIC results from Fig. 6.2, we find much larger multiplicities of the produced hadrons and smaller slopes of the spectra, indicating the larger transverse flow that is caused by the larger initial temperature.

Our model calculations of the HBT radii are shown in Fig. 7.3. The increase of the central temperature from $T_i = 320$ MeV to $T_i = 400 - 500$ MeV makes all the radii moderately larger. The ratio R_{out}/R_{side} decreases by about 10% which is an effect of the larger transverse flow caused, in turn, by the larger initial temperature.

7.2 Non-central collisions

In this Section we present our results describing the peripheral collisions with $T_i = 400$, 450 and 500 MeV, $T_f = 150$ MeV, and $b = 7.6$ fm. In Fig. 7.4 we show the freeze-out curves. One can observe that the system is initially elongated along the y axis, but in the end of the evolution it becomes elongated along the x axis. This behavior is indicated by the crossing of the freeze-out curves. The change of shape is caused by the strong flow which transforms the initial “almond” into a “pumpkin” [11]. Azimuthally sensitive HBT probes such non-trivial behavior and can be used as a precise confirmation test for the existence of such effects in the data.

In Fig. 7.5 we show the model transverse-momentum spectra of hadrons for the same values of the parameters. Compared to the RHIC case with $T_i = 320$ MeV and the same values of T_f , we find flatter spectra with higher multiplicity. In Fig. 7.6 we show our results for the elliptic-flow coefficient. The stronger transverse flow generated in this case induces larger splitting between the pion+kaon v_2 and the proton v_2 , with the values of the pion+kaon elliptic flow very similar to those found

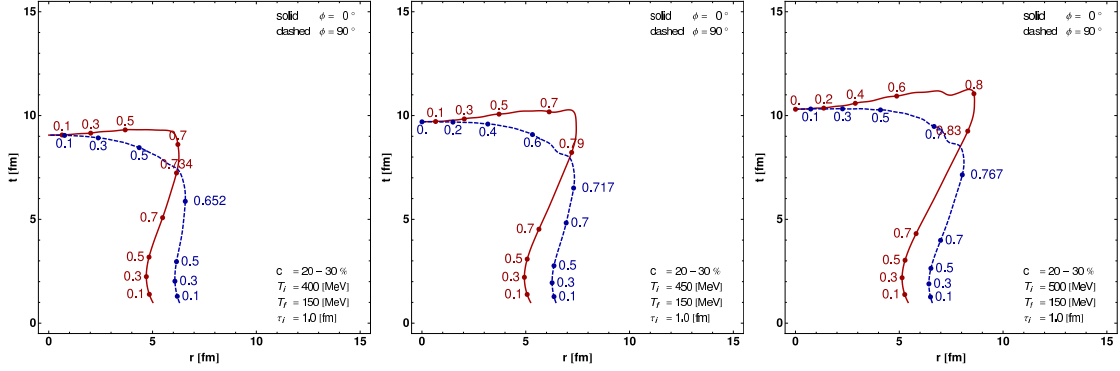


Figure 7.4: The freeze-out curves for peripheral collisions at LHC, $c = 20 - 30\%$, $b = 7.6$ fm, $\tau_i = 1.0$ fm, $T_i = 400, 450$ and 500 MeV, and $T_f = 150$ MeV. The solid (dashed) line shows the in-plane (out-of-plane) profile.

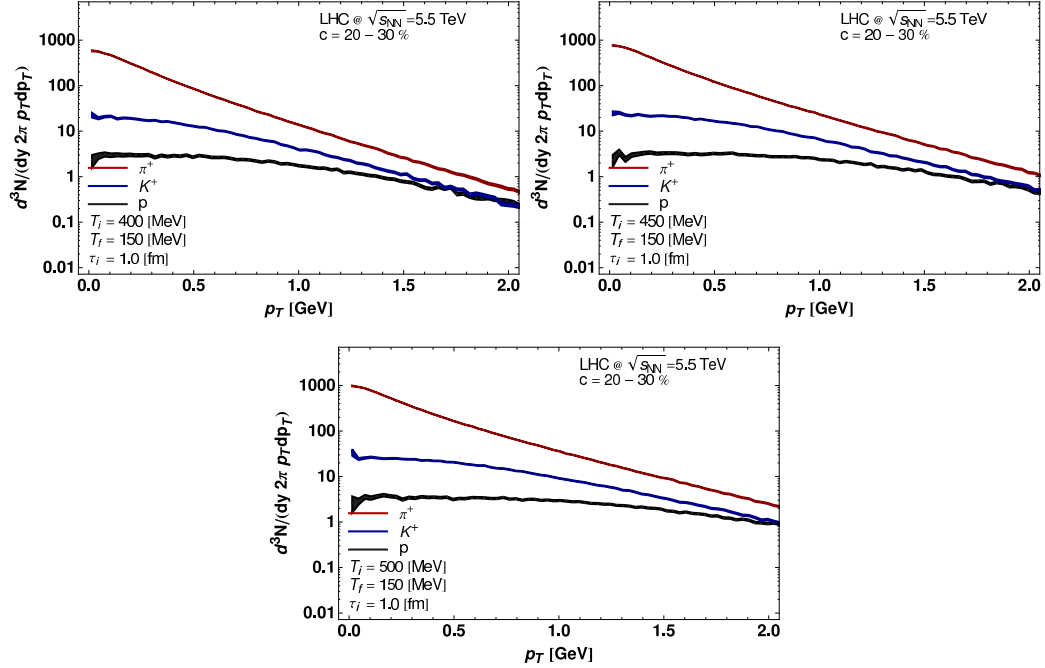


Figure 7.5: The model results for the transverse-momentum spectra of π^+ , K^+ , and protons. The values of the model parameters are the same as in Fig. 7.4.

in the case $T_i = 320$ MeV. This result indicates the saturation of the elliptic flow of light particles for a given initial space asymmetry. On the other hand, the proton elliptic flow is significantly reduced. This observation is consistent with the findings of Kestin and Heinz discussed in Ref. [83]. Finally, in Fig. 7.7 we show our model calculations of the HBT radii. We note that the ratio $R_{\text{out}}/R_{\text{side}}$ is very close to one.

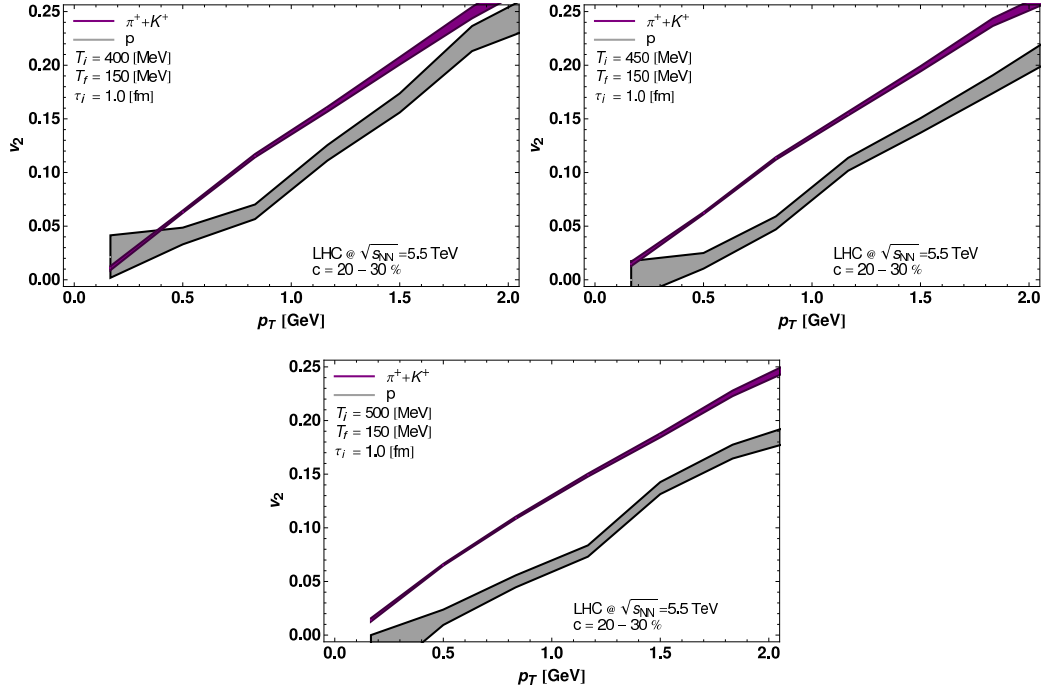


Figure 7.6: The elliptic flow coefficient v_2 . The parameters are the same as in Fig. 7.4.

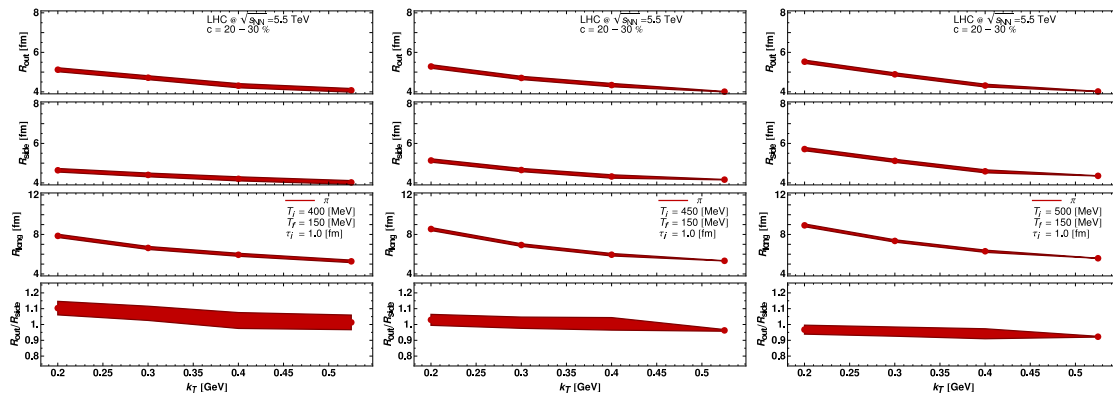


Figure 7.7: The pionic HBT radii. The values of the model parameters are the same as in Fig. 7.4.

Chapter 8

Uniform description of the RHIC data with Gaussian initial conditions

In this Chapter we return to the discussion of the RHIC results obtained at the top beam energy of $\sqrt{s_{NN}} = 200$ GeV. In the approach presented in Chapter 6 we used the standard initial conditions and were able to reproduce the experimental data with the accuracy of about 10-20%. In the following we are going to show that further improvement in the description of the data may be achieved if one uses modified initial conditions, namely, we suggest to use a two-dimensional Gaussian as an initial profile for the energy density in the transverse plane.

Of course, the elaboration of the precise initial conditions for hydrodynamics remains a challenge. Ideally, such initial conditions should be provided by the early-stage dynamics, for instance by the Color Glass Condensate [61, 60, 84]. In practice, the theory of the early stage carries some uncertainty in its parameters. Moreover, different phenomena may be present in the early stage, see e.g. [85, 86], so its precise modeling is difficult.

8.1 Early start of hydrodynamics

In the approach discussed in this Section we use a simple parameterization of the initial energy density profile in the transverse plane. At the proper time of $\tau_i = 0.25$ fm we assume that it may be described by a Gaussian

$$\varepsilon(\mathbf{x}_\perp) = \varepsilon_i \exp\left(-\frac{x^2}{2a^2} - \frac{y^2}{2b^2}\right), \quad (8.1)$$

where the values of the a and b width parameters depend on the centrality class and are obtained by matching to the results for $\langle x^2 \rangle$ and $\langle y^2 \rangle$ from GLISSANDO [57], which implements the eccentricity fluctuations of the system in the Glauber approach [87, 88]. The expression $(a^2 + b^2)/2$ describes the overall transverse size

Table 8.1: Initial central temperatures and shape parameters for various centrality classes.

c [%]	0 - 5	5 - 10	10 - 20	20 - 30	30 - 40	40 - 50
T_i [MeV]	500	490	475	460	430	390
a [fm]	2.696	2.536	2.284	2.000	1.771	1.577
b [fm]	2.925	2.849	2.738	2.591	2.448	2.305

c [%]	50 - 60	60 - 70	70 - 80	80 - 90	90 - 100	30 - 80
T_i [MeV]	345	303	260	—	—	330
a [fm]	1.401	1.224	1.040	0.841	0.511	1.592
b [fm]	2.164	2.019	1.854	1.649	1.228	2.307

of the system, whereas $(b^2 - a^2)/(b^2 + a^2)$ parameterizes its eccentricity. The use of the Gaussian profile (8.1) leads to a faster development of the transverse flow as compared to the Glauber initial conditions. This effect is crucial for the success of reproducing the HBT radii.

The values for centrality classes used in this work are collected in Table 8.1. Since the equation of state is known, the initial central temperature T_i defines the initial central energy density ε_i . It depends on centrality and has been adjusted to reproduce the total pion multiplicity. With the Gaussian initial conditions we continue the hydrodynamic evolution till the freeze-out temperature $T_f = 145$ MeV, where the system decouples and hadrons (stable and resonances) are generated according to the standard Cooper-Frye formalism [69] – see Chapters 6 and 7, Eq. 5.9. The lower value of T_f leads to larger sizes of the system and larger transverse flow. This in turn results in flatter p_T spectra and larger splitting of the v_2 of pions/kaons and protons.

The freeze-out hypersurfaces for two centrality classes are shown in Fig. 8.1. For comparison, in Figs. 6.1 and 6.4 in Chapter 6 we showed the hypersurfaces obtained in a calculation with the standard Glauber initial condition (and with same equation of state). We note that the Glauber initial condition results in hypersurfaces of a smaller transverse size and a longer evolution time, which translates into lower R_{side} and larger R_{out} . More generally, we note a quite different shape of the hypersurfaces in Fig. 8.1, however, the flow values are similar, which results from the fact that the model parameters are adjusted in such a way that the slopes of the p_T -spectra and the v_2 coefficient are reproduced. This leads to practically the same values of the flow velocity at freeze-out for the two compared calculations.

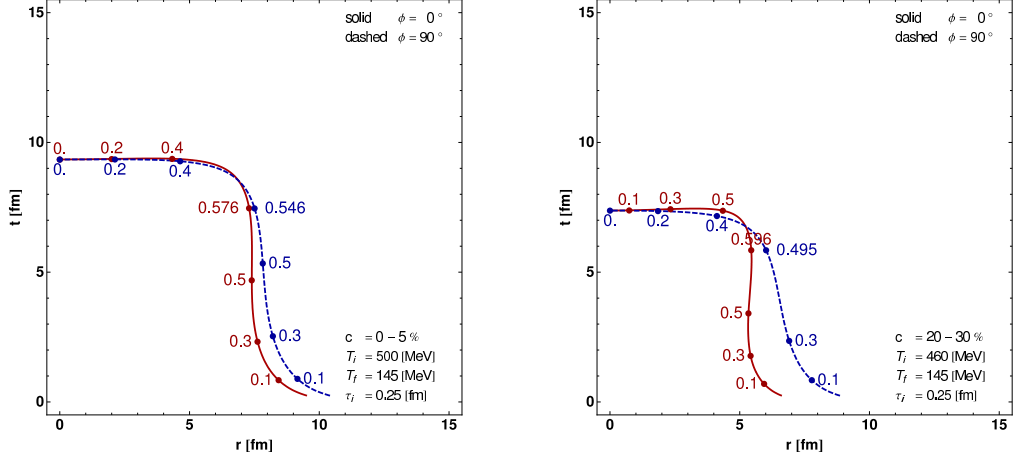


Figure 8.1: Freeze-out hypersurfaces for $c = 0 - 5\%$ (left) and $c = 20 - 30\%$ (right), obtained with the initial temperature $T_i = 500$ MeV and 460 MeV, for the central and semi-peripheral collisions, respectively, $\tau_i = 0.25$ fm and with the final temperature $T_f = 145$ MeV. The two curves show the in-plane and out-of-plane sections. The labels indicate the transverse flow velocity.

We should also stress out the similarity of the volume-emission parts (with time-like normal vectors) to the blast-wave parameterization [89], with a short lifetime: about 9 fm for central ($c = 0-5\%$) and 7 fm for mid-peripheral ($c = 20-30\%$) collisions. However, the freeze-out hypersurfaces contain also the surface emission parts (with space-like normal vectors), absent in the traditional blast-wave parameterizations. We have checked that the potential problems from the non-causal surface emission [90, 91, 92], are negligible, as less than 0.5% of particles are emitted back into the hydrodynamic region. The reason for this very small fraction is the sizable transverse flow velocity at large radii, as indicated by labels in Fig. 8.1, which pushes the particles outward, as well as the fact that the hypersurfaces are not bent back at low values of t . We have determined that about half of the produced particles comes from the volume part and about half from the surface part of the freeze-out hypersurface. The surface emission is crucial for fitting the HBT data from RHIC, as also advocated in [62, 63].

In Fig. 8.2 we present our results for the hadron transverse-momentum spectra for positive pions and kaons and protons in the central and semi-peripheral collisions with the experimental data from PHENIX [77]. The bottom plot of Fig. 8.2 represents the elliptic flow coefficient v_2 of joined pions + kaons and protons as a function of p_T together with the PHENIX [78] data points. We see a very good agreement of the one-particle observables. The v_2 description of protons is better than the one presented in the Chapter 6. The splitting between the summed v_2 of pions and kaons is larger which is a sign of a larger flow difference that developed on the hypersurface. This description can be further improved by including the elastic rescattering processes among hadrons after freeze-out.

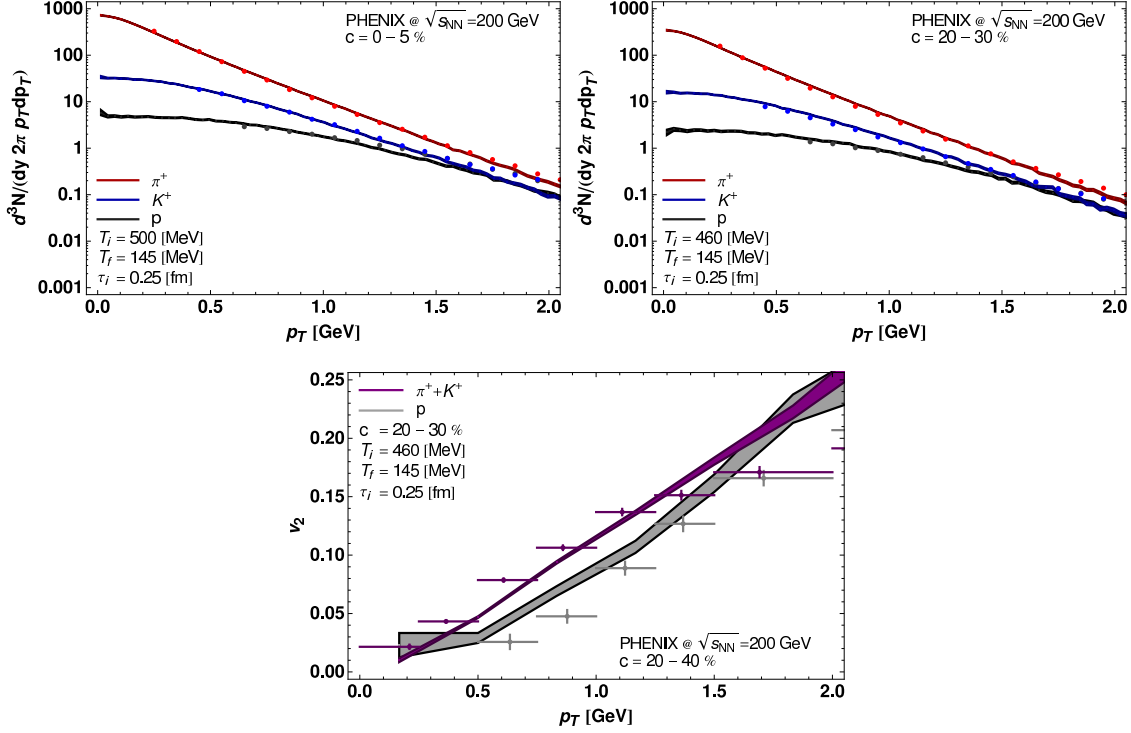


Figure 8.2: The transverse-momentum spectra of pions, kaons and protons for $c=0-5\%$ (left), $c=20-30\%$ (right), and the elliptic flow coefficient v_2 for $c=20-40\%$ (bottom), plotted as functions of the transverse momentum and compared to the data from [77, 78]. Model parameters same as in Fig. 8.1.

Figure 8.3 shows the HBT radii R_{side} , R_{out} , R_{long} and the ratio $R_{\text{out}}/R_{\text{side}}$. For the first time we can present a set of soft observables that are fully consistent with the experimental data. The most significant point is the correct description of the ratio $R_{\text{out}}/R_{\text{side}}$ in both central and non-central collisions. As in the previous calculation showed in Chapter 6, R_{long} exceeds the data which is most likely caused by the boost-invariance of our model and can be fixed by implementing a rapidity dependent initial distribution.

Although the success of the use of the Gaussian initial condition is evident, it is clear that a more detailed model describing the initial non-equilibrated stage of the evolution is necessary to address the issue of the microscopic validity of the initial Gaussian conditions. We leave this problem for our future investigations.

8.2 Hydrodynamics preceded by free-streaming

The very successful description of the soft observables that was presented in the previous Section demanded a very early start of the hydrodynamic evolution, $\tau_i = 0.25$ fm. Such short starting times have become now a common practice [93]. Nevertheless, the processes needed to thermalize the system require at least a few collisions

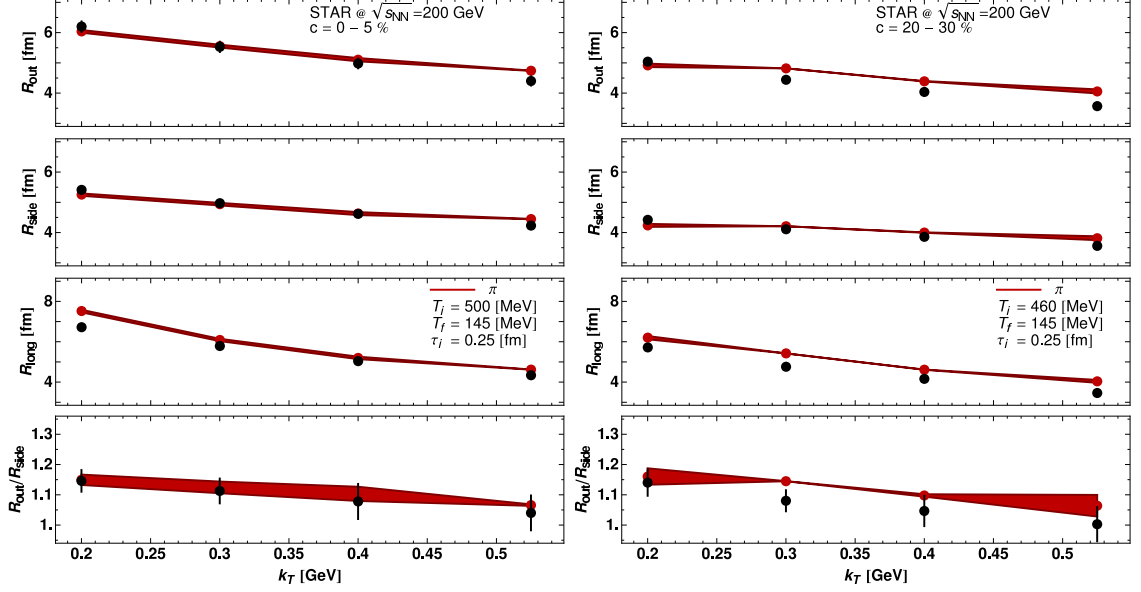


Figure 8.3: The pion HBT radii R_{side} , R_{out} , R_{long} , and the ratio $R_{\text{out}}/R_{\text{side}}$ for central collisions, compared to the data from [76]. Model parameters same as in Fig. 8.1.

to create local equilibrium. In this respect, the starting time of 0.25 fm seems to be very difficult to explain microscopically.

In Chapter 4.3 we have introduced the process of parton free-streaming. The basic idea behind it is the approximation of the early, stage evolution of a partonic system formed in heavy-ion collisions. In our approach the parton free streaming is followed by sudden equilibration (described by the Landau matching conditions), and then by hydrodynamics. This kind of a formalism was proposed by Kolb, Sollfrank, and Heinz [3] several years ago in the context of the development of azimuthally asymmetric flow. The approach assumes a sudden but delayed transition from a non-equilibrium initial state to a fully thermalized fluid.

The process of free-streaming decreases the spatial asymmetry of the density profile. This effect was the reason for not implementing the free streaming before hydrodynamics. The less asymmetric initial condition for the hydrodynamic stage produces smaller amounts of the elliptic flow. Free streaming itself cannot generate azimuthal asymmetry in the momentum distribution. Interactions among produced particles are needed to achieve this goal. But a sudden equilibration preceded by free-streaming is in fact capable of developing azimuthally asymmetric flow. The energy-momentum tensor of the system changes abruptly into a diagonal form (in the reference frame co-moving with the fluid element). In this way the space-flow correlations are induced, which results in a collective elliptic flow, further enhanced by the subsequent hydrodynamic evolution.

Our results presented in this Section were obtained with the free-streaming stage lasting from $\tau_0 = 0.25$ to $\tau_1 = 1.0$ fm, followed by a sudden equilibration and hydrodynamics. The initial hydrodynamic time was shifted to a later time of 1.0

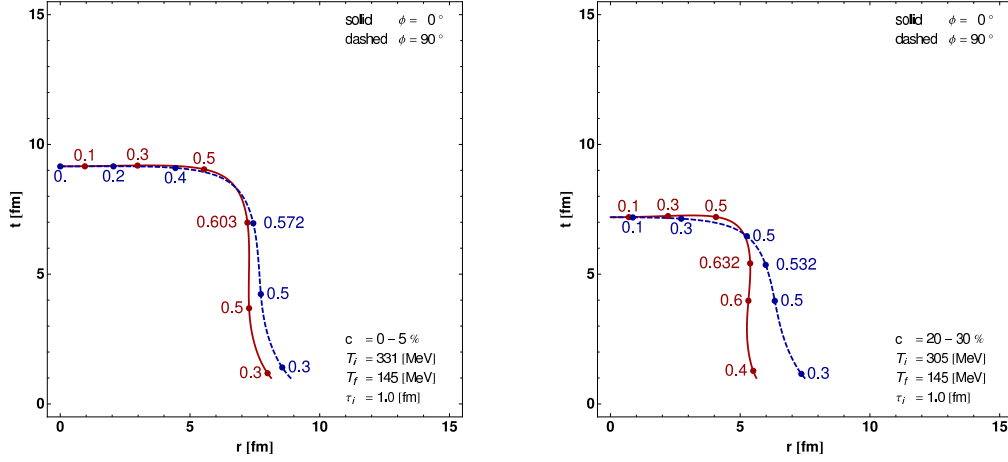


Figure 8.4: Freeze-out hypersurfaces for $c = 0 - 5\%$ (left) and $c = 20 - 30\%$ (right). Calculations include the free-streaming phase from $\tau_0 = 0.25$ fm to $\tau_1 = 1.0$ fm. The initial central temperature T_i equals 331 and 305 MeV, for central and non-central collisions, respectively. The freeze-out temperature is set to $T_f = 145$ MeV.

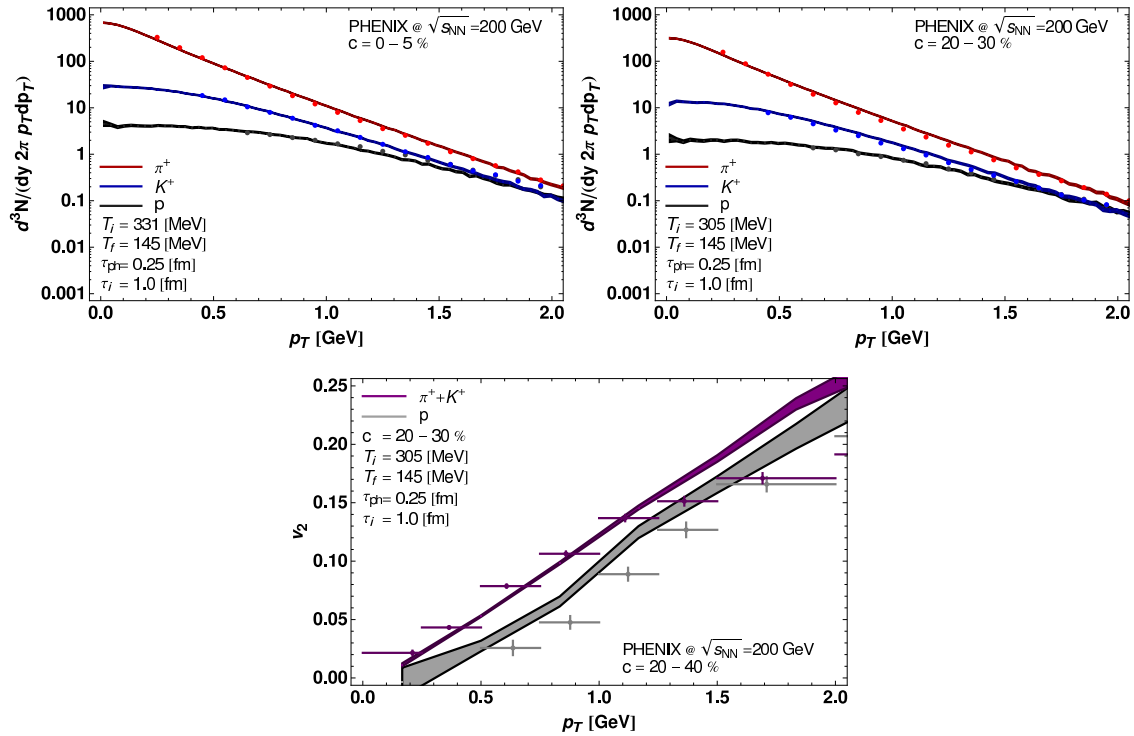


Figure 8.5: The transverse-momentum spectra of pions, kaons and protons for $c=0-5\%$ (upper left panel), $c=20-30\%$ (upper right panel) and the elliptic flow coefficient v_2 for $c=20-40\%$ (lower panel). Model parameters as in Fig. 8.4. Data from [77, 78].

fm. Such a change requires a different normalization of the energy density at the center of the fireball, since during the time of 0.75 fm the system expands and its density decreases. To make an estimate of the initial energy at a later starting time we use the Bjorken scaling for the entropy [47]. We calculate the entropy density s_0 at τ_0 from the energy density ε_0 and scale it by the following formula

$$s_0\tau_0 = s_i\tau_i = \text{const.} \quad \rightarrow \quad s_i = s_0 \frac{\tau_0}{\tau_i}. \quad (8.2)$$

As a result the initial central temperature for the most central collision ($c = 0 - 5\%$) is changed from $T_i = 500$ MeV down to 331 MeV and for the peripheral case ($c = 20 - 30\%$) the temperature is decreased from 460 MeV to 305 MeV. This type of scaling works surprisingly well as the method of construction the initial conditions at $\tau_i = 1.0$ fm. If we compare the hypersurfaces from the previous section, Fig. 8.1, with the new ones obtained with the free-streaming, Fig. 8.4, then one can notice that they are almost identical. Both the shapes (starting from $\tau = 1.0$ fm) and values of the velocity on the hypersurface are very similar.

The results of the calculations with a pre-hydrodynamics stage are shown in Figs. 8.5 and 8.6. As in Section 8.1 we have started from the Gaussian profile (8.1). We notice very similar results to the ones obtained in the previous Section, not to mention the very good description of the data. Larger free-streaming times ($\tau - \tau_0 \sim 1.5$ fm) spoil this agreement, as the flow becomes too strong. Again we have achieved a uniform agreement for soft physics at RHIC. In particular, the transverse-momentum spectra, the elliptic-flow, and the HBT correlation radii, including the notorious ratio $R_{\text{out}}/R_{\text{side}}$, are all properly described.

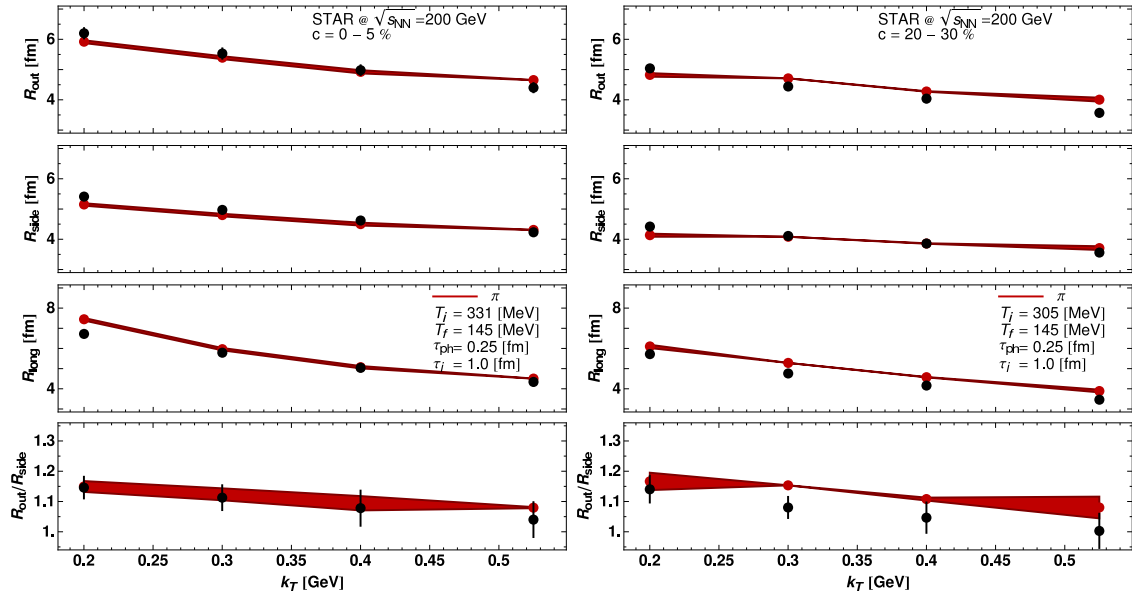


Figure 8.6: The pion HBT radii R_{side} , R_{out} , R_{long} , and the ratio $R_{\text{out}}/R_{\text{side}}$ for central collisions, compared to the data from [76]. Model parameters same as in Fig. 8.4.

Chapter 9

Summary

Our recently developed 2+1 (boost-invariant) hydrodynamic model has been presented and used to i) describe the soft hadronic data collected in the central region of the relativistic heavy-ion collisions at RHIC and ii) to make predictions for the heavy-ion collisions at the LHC energies. We have addressed both the one- and two-particle observables: the transverse momentum spectra, the elliptic flow coefficient v_2 , and the pion HBT radii. The realistic equation of state for strongly interacting matter has been constructed that interpolates between the hadron gas model and the results of the QCD lattice simulations. The computational platform has been constructed, which combines the results of our hydrodynamic code with the statistical hadronization model **THERMINATOR**. The satisfactory description of the soft hadronic RHIC data has been achieved with the standard initial conditions obtained from the optical limit of the Glauber model. Predictions for the future heavy-ion collisions at LHC have been formulated. The solution of the RHIC HBT puzzle has been proposed. It suggests the use of the modified Gaussian-type initial conditions for the energy density in the transverse plane. Finally, the processes of the free streaming of partons followed by the sudden equilibration have been incorporated in the model. The inclusion of the free-streaming stage allows for the delayed start of the hydrodynamic evolution, which is a desirable effect in the context of the early thermalization problem.

Appendix A

Relativistic thermodynamics of perfect gases

A.1 Grand canonical potential Ω

The first law of thermodynamics for systems described by the grand canonical ensemble reads

$$dE = T dS - P dV + \mu dN, \quad (\text{A.1})$$

where E is the energy, S is the entropy, P stands for pressure, and N is the number of particles in the system (for relativistic systems the number of particles is not conserved and N should be interpreted as the baryon number or any other conserved quantity, for example strangeness). Energy is an extensive function of three extensive variables, $E = E(S, V, N)$. By scaling the entropy, volume, and particle number by a factor λ , we obtain the energy rescaled by the same factor

$$E(\lambda S, \lambda V, \lambda N) = \lambda E(S, V, N). \quad (\text{A.2})$$

By calculating the total derivative with respect to the scaling parameter λ and using the relation (A.1) we find

$$\left. \frac{\partial E}{\partial S} \right|_{V,N} S + \left. \frac{\partial E}{\partial V} \right|_{S,N} V + \left. \frac{\partial E}{\partial N} \right|_{S,V} N = E, \quad (\text{A.3})$$

which leads to

$$T S - P V + \mu N = E. \quad (\text{A.4})$$

The grand canonical potential Ω is defined as

$$\Omega = E - T S - \mu N = -P V. \quad (\text{A.5})$$

To calculate the change of the potential Ω we calculate the total derivative from Eq. (A.5) and use (A.1). In this way we find

$$d\Omega = -S dT - P dV - N d\mu. \quad (\text{A.6})$$

A.1.1 The grand canonical partition function

It is useful to start our consideration with the introduction of the partition function for perfect gases. In this case the grand canonical partition function is defined in the following way

$$Z = \prod_{i=1}^{\infty} z_i = \prod_{i=1}^{\infty} \sum_{n_i=0}^{\infty} e^{\frac{n_i(\mu-\epsilon_i)}{T}}, \quad (\text{A.7})$$

where the index i runs over all microstates of the system and z_i is an individual partition function for that microstate. The index n_i is the number of particles with the energy ϵ_i in the state i . In the cases where the product is taken over the states with equal energy rather than over all microscopic states, we introduce the degeneration factor g_i giving the number of states with the same energy

$$Z = \prod_{i=1}^{\infty} (z_i)^{g_i}. \quad (\text{A.8})$$

For indistinguishable particles satisfying the Bose-Einstein or Fermi-Dirac statistics we are able to evaluate explicitly the sum in Eq. (A.7)

$$z_i = \sum_{n_i=0}^{\infty} e^{\frac{n_i(\mu-\epsilon_i)}{T}} = \frac{1}{1 - e^{\frac{\mu-\epsilon_i}{T}}} \quad (\text{Bose-Einstein}), \quad (\text{A.9})$$

$$z_i = \sum_{n_i=0}^1 e^{\frac{n_i(\mu-\epsilon_i)}{T}} = \left(1 + e^{\frac{\mu-\epsilon_i}{T}}\right) \quad (\text{Fermi-Dirac}). \quad (\text{A.10})$$

A.1.2 Quantum statistics

From the statistical physics we know the connection between Z and Ω ,

$$\Omega(T, V, \mu) = -T \ln Z, \quad (\text{A.11})$$

which gives

$$\Omega = -T \ln Z = -T \ln \prod_{i=1}^{\infty} (z_i)^{g_i} = -T \sum_{i=1}^{\infty} g_i \ln z_i. \quad (\text{A.12})$$

This formula can be further rewritten in the form including Bose-Einstein ($\epsilon = -1$) or Fermi-Dirac ($\epsilon = +1$) statistics, Eqs. (A.9) and (A.10),

$$\Omega = -T \epsilon \sum_{i=1}^{\infty} g_i \ln \left(1 + \epsilon e^{\frac{\mu-\epsilon_i}{T}}\right). \quad (\text{A.13})$$

In the classical approach we can replace the sum in Eq. (A.13) by the integration over the one-particle phase-space. This will lead us to the general form of the grand potential

$$\Omega(T, V, \mu) = -T V g \epsilon \int \frac{d^3 p}{(2\pi)^3} \ln \left(1 + \epsilon e^{\frac{\mu-E_p}{T}}\right). \quad (\text{A.14})$$

Here we assumed that all the degeneracies are equal $g_i = g$ – this is the typical case where g is related to the spin degeneracy where $g = 2s + 1$.

In the following we shall assume that the condition $\mu - E < 0$ is fulfilled. This condition is always true for bosons and it is also valid for fermions in the case $\mu < m$. In this case we use the series expansion of the logarithm,

$$\ln(1+x) = - \sum_{\kappa=1}^{\infty} \frac{(-1)^{\kappa}}{\kappa} x^{\kappa}, \quad (\text{A.15})$$

to rewrite Eq. (A.14) in the form

$$\Omega_{\text{QS}}(T, V, \mu) = T V g \epsilon \int \frac{d^3 p}{(2\pi)^3} \sum_{\kappa=1}^{\infty} \frac{(-\epsilon)^{\kappa}}{\kappa} e^{\frac{\mu - E_p}{T} \kappa}. \quad (\text{A.16})$$

A.1.3 Boltzmann classical limit

For particles which have small average occupation numbers one can use the approximation of the classical Boltzmann gas. This assumption is realized by using only the leading term in the expansion (A.16), that corresponds to $\kappa = 1$,

$$\Omega_{\text{BL}}(T, V, \mu) = -T V g \int \frac{d^3 p}{(2\pi)^3} e^{\frac{\mu - E_p}{T}}. \quad (\text{A.17})$$

We note that this approximation is independent of quantum statistics since in Eq. (A.16) we have always the term $\epsilon^{\kappa+1}$ which equals 1 for $\kappa = 1$.

A.1.4 Massive particles

The relativistic relation between the particle energy E_p , momentum p , and the rest mass m is $E_p = \sqrt{p^2 + m^2}$. Introducing this relation into Eq. (A.16) enables us to calculate the potential Ω for massive particles

$$\Omega(T, V, \mu) = T V g \epsilon \sum_{\kappa=1}^{\infty} \frac{(-\epsilon)^{\kappa}}{\kappa} \int \frac{d^3 p}{(2\pi)^3} e^{\frac{\mu - \sqrt{m^2 + p^2}}{T} \kappa}. \quad (\text{A.18})$$

Changing to the spherical coordinates and performing simple calculations we find

$$\Omega(T, V, \mu) = \frac{1}{2\pi^2} T V g \epsilon \sum_{\kappa=1}^{\infty} \frac{(-\epsilon)^{\kappa}}{\kappa} e^{\frac{\mu}{T} \kappa} \int_0^{\infty} dp p^2 e^{-\frac{\sqrt{m^2 + p^2}}{T} \kappa}. \quad (\text{A.19})$$

Let us now consider only the integral on the right-hand-side of Eq. (A.19). By changing the integration variables from p to x with the substitution $m^2 + p^2 = m^2 x^2$, this integral takes the following form

$$\int_0^{\infty} dp p^2 e^{-\frac{\sqrt{m^2 + p^2}}{T} \kappa} = m^3 \int_1^{\infty} dx x (x^2 - 1)^{\frac{1}{2}} e^{-\frac{m \kappa}{T} x}. \quad (\text{A.20})$$

Table A.1: Grand canonical potential Ω for various choices of m .

quantum statistics	
$m \neq 0$	$\frac{1}{2\pi^2} T^2 V g m^2 \epsilon \sum_{\kappa=1}^{\infty} \frac{(-\epsilon)^{\kappa}}{\kappa^2} e^{\frac{\mu}{T}\kappa} K_2\left(\frac{m}{T}\kappa\right)$
$m = 0$	$\frac{1}{\pi^2} T^4 V g \epsilon \text{Li}_4\left(-\epsilon e^{\frac{\mu}{T}}\right)$
classical limit	
$m \neq 0$	$-\frac{1}{2\pi^2} T^2 V g m^2 e^{\frac{\mu}{T}} K_2\left(\frac{m}{T}\right)$
$m = 0$	$-\frac{1}{\pi^2} T^4 V g e^{\frac{\mu}{T}}$

The formula above may be reduced to the integral definition of the modified Bessel function of the second kind $K_{\nu}(z)$, see Eq. (D.3) with $\nu = 2$ and $z = m\kappa/T$,

$$\frac{m^3}{3} \frac{m\kappa}{T} \int_1^{\infty} dx (x^2 - 1)^{2-\frac{1}{2}} e^{-\frac{m\kappa}{T}x} = m^2 \frac{T}{\kappa} K_2\left(\frac{m}{T}\kappa\right). \quad (\text{A.21})$$

Thus we write the final form of the grand canonical potential for massive particles with finite chemical potential and quantum statistics as follows

$$\Omega(T, V, \mu) = \frac{1}{2\pi^2} T^2 V m^2 g \epsilon \sum_{\kappa=1}^{\infty} \frac{(-\epsilon)^{\kappa}}{\kappa^2} e^{\frac{\mu}{T}\kappa} K_2\left(\frac{m}{T}\kappa\right) \quad (m > 0, \mu < m). \quad (\text{A.22})$$

A.1.5 Massless particles

Of the special interest is the case of massless particles. Such a limiting case is appropriate for gluons and also for quarks at sufficiently high temperatures¹. The thermodynamical properties of massless particles follow directly from the formula (A.14) where we set $m = 0$ and $\mu = 0$. The alternative way is to consider the limiting case of Eq. (A.22). For massless particles the modified Bessel function $K_{\nu}(z)$ in Eq. (A.22) may be expanded into a power series in the vicinity of the point $m = 0$ according to Eqs. (D.7). This leads us to the expression

$$\Omega(T, V, \mu) = \frac{1}{2\pi^2} T^2 V m^2 g \epsilon \sum_{\kappa=1}^{\infty} \frac{(-\epsilon)^{\kappa}}{\kappa^2} e^{\frac{\mu}{T}\kappa} \left(\frac{2}{\left(\frac{m}{T}\kappa\right)^2} - \frac{1}{2} + O(2) \right). \quad (\text{A.23})$$

¹Typically the light quarks u and d may be regarded as massless particles. If the temperature is sufficiently high, in addition the strange quark may be regarded as a massless particles.

Table A.2: Mean number of particles N for various choices of m .

quantum statistics	
$m \neq 0$	$-\frac{1}{2\pi^2} T V g m^2 \epsilon \sum_{\kappa=1}^{\infty} \frac{(-\epsilon)^{\kappa}}{\kappa} e^{\frac{\mu}{T}\kappa} K_2\left(\frac{m}{T}\kappa\right)$
$m = 0$	$-\frac{1}{\pi^2} T^3 V g \epsilon \text{Li}_3\left(-\epsilon e^{\frac{\mu}{T}}\right)$
classical limit	
$m \neq 0$	$\frac{1}{2\pi^2} T V g m^2 e^{\frac{\mu}{T}} K_2\left(\frac{m}{T}\right)$
$m = 0$	$\frac{1}{\pi^2} T^3 V g e^{\frac{\mu}{T}}$

Since only the first term of this expansion gives non zero contribution in the limit $m \rightarrow 0$, the grand potential for massless particles reads

$$\Omega(T, V, \mu) = \frac{1}{\pi^2} T^4 V g \epsilon \sum_{\kappa=1}^{\infty} \frac{(-\epsilon e^{\frac{\mu}{T}})^{\kappa}}{\kappa^4} = \frac{1}{\pi^2} T^4 V g \epsilon \text{Li}_4\left(-\epsilon e^{\frac{\mu}{T}}\right). \quad (\text{A.24})$$

Here we have introduced the polylogarithm function defined by the series

$$\text{Li}_n(z) = \sum_{k=1}^{\infty} \frac{z^k}{k^n}. \quad (\text{A.25})$$

In the limit of vanishing chemical potential the values $\text{Li}_4(1)$ (required for bosons) and $\text{Li}_4(+1)$ (required for fermions) should be obtained from the analytic continuation which gives $\text{Li}_4(1) = \pi^4/90$ and $\text{Li}_4(-1) = -7\pi^4/720$. In this way we obtain

$$\Omega(T, V, \mu = 0, m = 0) = -\frac{\pi^2}{90} g V T^4 \quad (\text{Bose-Einstein}) \quad (\text{A.26})$$

and

$$\Omega(T, V, \mu = 0, m = 0) = -\frac{7\pi^2}{720} g V T^4 \quad (\text{Fermi-Dirac}). \quad (\text{A.27})$$

A.1.6 Vanishing chemical potential

Sometimes one assumes that the chemical potential is very small and may be neglected. In this case the grand canonical potential, Eq. (A.16), takes the form

$$\Omega(T, V, \mu = 0) = -T V g \epsilon \int \frac{d^3 p}{(2\pi)^3} \sum_{\kappa=1}^{\infty} \frac{(-\epsilon)^{\kappa}}{\kappa} e^{-\frac{E_p}{T}\kappa}, \quad (\text{A.28})$$

or in the case of classical massless gas with no chemical potential

$$\Omega_{\text{BL}}(T, V, \mu = 0) = -\frac{1}{\pi^2} g V T^4. \quad (\text{A.29})$$

A.2 Other thermodynamic variables

Given the formula for the differential of the grand potential (A.6) we can evaluate the mean number of particles using the following expression

$$N = - \left. \frac{\partial \Omega}{\partial \mu} \right|_{T, V}. \quad (\text{A.30})$$

With the most general definition of Ω , valid for massive gas with quantum statistics, see Eq. (A.22), we find

$$N(T, V, \mu) = -\frac{1}{2\pi^2} T V m^2 g \epsilon \sum_{\kappa=1}^{\infty} \frac{(-\epsilon)^{\kappa}}{\kappa^2} e^{\frac{\mu}{T}\kappa} K_2\left(\frac{m}{T}\kappa\right). \quad (\text{A.31})$$

Neglecting the quantum statistics will lead to the Boltzmann classical approximation in the form

$$N_{\text{BL}}(T, V, \mu) = \frac{1}{2\pi^2} T V e^{\frac{\mu}{T}} m^2 g K_2\left(\frac{m}{T}\right). \quad (\text{A.32})$$

In the further step we can do the massless-gas assumption and following the same formalism as in subsection A.1.5 one gets

$$N_{\text{BL}}(T, V, \mu) = \frac{1}{\pi^2} T^3 g V e^{\frac{\mu}{T}}. \quad (\text{A.33})$$

The formula for the entropy follows from the equation

$$S = - \left. \frac{\partial \Omega}{\partial T} \right|_{\mu, V}, \quad (\text{A.34})$$

which for massive particles obeying the quantum statistics gives

$$S = -\frac{1}{2\pi^2} V m^2 g \epsilon \sum_{\kappa=1}^{\infty} \frac{(-\epsilon)^{\kappa}}{\kappa^2} e^{\frac{\mu}{T}\kappa} \left[(4T - \mu) K_2\left(\frac{m}{T}\kappa\right) + m \kappa K_1\left(\frac{m}{T}\kappa\right) \right]. \quad (\text{A.35})$$

Similarly, to calculate the pressure we use the formula

$$P = - \left. \frac{\partial \Omega}{\partial V} \right|_{T, \mu} \quad (\text{A.36})$$

and get

$$P = -\frac{1}{2\pi^2} T^2 m^2 g \epsilon \sum_{\kappa=1}^{\infty} \frac{(-\epsilon)^{\kappa}}{\kappa^2} e^{\frac{\mu}{T}\kappa} K_2\left(\frac{m}{T}\kappa\right). \quad (\text{A.37})$$

Table A.3: Entropy for various choices of m .

quantum statistics	
$m \neq 0$	$-\frac{1}{2\pi^2} V g m^2 \epsilon \sum_{\kappa=1}^{\infty} \frac{(-\epsilon)^{\kappa}}{\kappa^2} e^{\frac{\mu}{T}\kappa} \left[(4T - \mu \kappa) K_2\left(\frac{m}{T}\kappa\right) + m \kappa K_1\left(\frac{m}{T}\kappa\right) \right]$
$m = 0$	$-\frac{1}{\pi^2} T^2 V g \epsilon \left[4T \text{Li}_4\left(-\epsilon e^{\frac{\mu}{T}}\right) - \mu \text{Li}_3\left(-\epsilon e^{\frac{\mu}{T}}\right) \right]$
classical limit	
$m \neq 0$	$\frac{1}{2\pi^2} V g m^2 e^{\frac{\mu}{T}} \left[(4T - \mu) K_2\left(\frac{m}{T}\right) + m K_1\left(\frac{m}{T}\right) \right]$
$m = 0$	$\frac{1}{\pi^2} T^2 V g e^{\frac{\mu}{T}} (4T - \mu)$

Table A.4: Pressure for various choices of m .

quantum statistics	
$m \neq 0$	$-\frac{1}{2\pi^2} T^2 g m^2 \epsilon \sum_{\kappa=1}^{\infty} \frac{(-\epsilon)^{\kappa}}{\kappa^2} e^{\frac{\mu}{T}\kappa} K_2\left(\frac{m}{T}\kappa\right)$
$m = 0$	$-\frac{1}{\pi^2} T^4 g \epsilon \text{Li}_4\left(-\epsilon e^{\frac{\mu}{T}}\right)$
classical limit	
$m \neq 0$	$\frac{1}{2\pi^2} T^2 g m^2 e^{\frac{\mu}{T}} K_2\left(\frac{m}{T}\right)$
$m = 0$	$\frac{1}{\pi^2} T^4 g e^{\frac{\mu}{T}}$

Finally, the energy is obtained from the relation

$$E = T S - P V + \mu N \quad (\text{A.38})$$

which gives

$$E = -\frac{1}{2\pi^2} T V g m^2 \epsilon \sum_{\kappa=1}^{\infty} \frac{(-\epsilon)^{\kappa}}{\kappa^2} e^{\frac{\mu}{T}\kappa} \left[3T K_2\left(\frac{m}{T}\kappa\right) + m \kappa K_1\left(\frac{m}{T}\kappa\right) \right]. \quad (\text{A.39})$$

Table A.5: Energy for various choices of m .

quantum statistics	
$m \neq 0$	$-\frac{1}{2\pi^2} T V g m^2 \epsilon \sum_{\kappa=1}^{\infty} \frac{(-\epsilon)^{\kappa}}{\kappa^2} e^{\frac{\mu}{T} \kappa} \left[3 T K_2 \left(\frac{m}{T} \kappa \right) + m \kappa K_1 \left(\frac{m}{T} \kappa \right) \right]$
$m = 0$	$-\frac{3}{\pi^2} T^4 V g \epsilon \operatorname{Li}_4 \left(-\epsilon e^{\frac{\mu}{T}} \right)$
classical limit	
$m \neq 0$	$\frac{1}{2\pi^2} T V g m^2 e^{\frac{\mu}{T}} \left[3 T K_2 \left(\frac{m}{T} \right) + m K_1 \left(\frac{m}{T} \right) \right]$
$m = 0$	$\frac{3}{\pi^2} T^4 V g e^{\frac{\mu}{T}}$

Appendix B

Properties of relativistic hydrodynamic equations for $\mu_B = 0$

This Appendix presents the details of transformations of the relativistic hydrodynamic equations which were applied to obtain the final form used in the numerical calculations. It also introduces the basic hydrodynamic definitions that are used in our work.

B.1 Basic definitions

The fluid four-velocity is defined as

$$u^\mu = (u^0, u^i) = \gamma (1, \mathbf{v}) = \gamma (1, v_x, v_y, v_z), \quad (\text{B.1})$$

where γ is the Lorentz factor defined as

$$\gamma = u^0 = \frac{1}{\sqrt{1 - v^2}}. \quad (\text{B.2})$$

The derivative of γ equals

$$d\gamma = \gamma^3 v^i dv^i = \gamma^3 v dv, \quad (\text{B.3})$$

where

$$v dv = \gamma^{-3} d\gamma, \quad v = \sqrt{v_x^2 + v_y^2 + v_z^2} = \sqrt{v_\perp^2 + v_z^2}. \quad (\text{B.4})$$

Here v_\perp is the magnitude of the transverse velocity \mathbf{v}_\perp . The total time derivative in the Cartesian coordinates reads

$$\frac{d}{dt} = \frac{\partial}{\partial t} + v^j \frac{\partial}{\partial x^j} = \frac{\partial}{\partial t} + v_x \frac{\partial}{\partial x} + v_y \frac{\partial}{\partial y} + v_z \frac{\partial}{\partial z}, \quad (\text{B.5})$$

while in the cylindrical coordinates it has the form

$$\frac{d}{dt} = \frac{\partial}{\partial t} + v_\perp \cos \alpha \frac{\partial}{\partial r} + \frac{v_\perp \sin \alpha}{r} \frac{\partial}{\partial \phi} + v_z \frac{\partial}{\partial z}. \quad (\text{B.6})$$

Here α is the angle between the transverse velocity \mathbf{v}_\perp and radial velocity \mathbf{v}_r , $v_r = v_\perp \cos \alpha$, $v_\phi = v_\perp \sin \alpha$.

B.2 Covariant form

The conservation of the energy-momentum tensor of the perfect fluid in its most general form yields

$$\partial_\mu [(\varepsilon + P) u^\mu u^\nu - P g^{\mu\nu}] = 0. \quad (\text{B.7})$$

We transform Eq. (B.7) using thermodynamic identities $\varepsilon + P = T s$ and $dP = s dT$ to get

$$T u^\nu \partial_\mu (s u^\mu) + s u^\mu \partial_\mu (T u^\nu) = s \partial^\nu T. \quad (\text{B.8})$$

Multiplying both sides of Eq. (B.8) by u_ν and using the normalization condition for the four-velocity, $u^\nu u_\nu = 1$, we arrive at the following formula

$$T \partial_\mu (s u^\mu) + s u^\mu T u_\nu \partial_\mu u^\nu + s u^\mu \partial_\mu T = s u_\nu \partial^\nu T. \quad (\text{B.9})$$

The term that includes $u_\nu \partial_\mu u^\nu$ is equal to zero because of the four-velocity normalization condition. Thus, we find the expression

$$T \partial_\mu (s u^\mu) + s u^\mu \partial_\mu T = s u_\nu \partial^\nu T. \quad (\text{B.10})$$

This equation directly implies that

$$\partial_\mu (s u^\mu) = 0. \quad (\text{B.11})$$

Eq. (B.11) states that the entropy is conserved in the system – the hydrodynamic expansion is adiabatic.

In the next step we return to Eq. (B.8) and use Eq. (B.11) to rewrite it in the following form

$$u^\mu \partial_\mu (T u^\nu) = \partial^\nu T. \quad (\text{B.12})$$

Eq. (B.12) is the acceleration equation – a relativistic generalization of the Euler equation known from the classical fluid dynamics. Equation (B.12) includes only tree non-trivial equations. It is easy to check this property if we project this equation on the four-velocity u_ν . The final form of the hydrodynamic equations in the covariant form consists of a set of four equations

$$\begin{aligned} u^\mu \partial_\mu (T u^\nu) &= \partial^\nu T, \\ \partial_\mu (s u^\mu) &= 0, \end{aligned} \quad (\text{B.13})$$

which should be supplemented by the equation of state.

B.3 Non-covariant form

In this Section we show how to rewrite relativistic hydrodynamic equations in the non-covariant form. We start with the acceleration equation in the covariant form, Eq. (B.12), and show that the corresponding non-covariant form is

$$\frac{\partial}{\partial t} (T \gamma \mathbf{v}) + \nabla (T \gamma) = \mathbf{v} \times [\nabla \times (T \gamma \mathbf{v})]. \quad (\text{B.14})$$

In order to prove this property we write the i th (spatial) component of Eq. (B.14) as

$$\frac{\partial}{\partial t}(T\gamma v^i) + \nabla^i(T\gamma) = \epsilon^{ijk} v^j \epsilon^{klm} \nabla^l(T\gamma v^m). \quad (\text{B.15})$$

The next step is to contract the ϵ tensors with the help of the formula

$$\epsilon^{ijk} \epsilon^{klm} = \delta^{il} \delta^{jm} - \delta^{im} \delta^{jl}$$

and to carry out the sums with the Kronecker delta. In this way we find

$$\frac{\partial}{\partial t}(T\gamma v^i) + \nabla^i(T\gamma) = v^j \nabla^i(T\gamma v^j) - v^j \nabla^j(T\gamma v^i). \quad (\text{B.16})$$

We move the terms in Eq. (B.16) that include $T\gamma v^i$ to the left-hand-side and multiply both sides of this equation by the Lorentz γ factor. This procedure yields the equation whose sides are given by the expressions

$$\begin{aligned} \text{LHS} &= \gamma \frac{\partial}{\partial t}(T\gamma v^i) + \gamma v^j \nabla^j(T\gamma v^i) = u^0 \partial_0(Tu^i) + u^j \partial_j(Tu^i) = u^\mu \partial_\mu(Tu^i), \\ \text{RHS} &= \gamma v^j \nabla^i(T\gamma v^j) - \gamma \nabla^i(T\gamma) = \gamma^2(v^2 - 1) \nabla^i T + T \left[\gamma(v^2 - 1) + \frac{1}{\gamma} \right] \nabla^i \gamma \\ &= -\nabla^i T = \partial^i T. \end{aligned}$$

One observes that both sides of Eq. (B.12) are reproduced after those manipulations. The non-covariant form of the entropy conservation law, Eq. (B.11), may be written in the straightforward way as

$$\frac{\partial}{\partial t}(s\gamma) + \nabla(s\gamma \mathbf{v}) = 0. \quad (\text{B.17})$$

B.4 Temperature equation

In this section we study in more detail the temperature equation (B.14). We start with the i th component of Eq. (B.14), which in the tensor notation has the form

$$\frac{\partial}{\partial t}(T\gamma v^i) + \nabla^i(T\gamma) = v^j \nabla^i(T\gamma v^j) - v^j \nabla^j(T\gamma v^i). \quad (\text{B.18})$$

We expand separately the left- and the right-hand-side of Eq. (B.18) to find

$$\begin{aligned} \text{LHS} &= \gamma v^i \frac{\partial T}{\partial t} + T v^i \frac{\partial \gamma}{\partial t} + T \gamma \frac{\partial v^i}{\partial t} + \gamma \frac{\partial T}{\partial x^i} + T \frac{\partial \gamma}{\partial x^i} \\ &= \gamma v^i \frac{\partial T}{\partial t} + T v^i \gamma^3 v^k \frac{\partial v^k}{\partial t} + T \gamma \frac{\partial v^i}{\partial t} + \gamma \frac{\partial T}{\partial x^i} + T \gamma^3 v^k \frac{\partial v^k}{\partial x^i} \\ &= T \gamma \left[v^i \frac{\partial \ln T}{\partial t} + \gamma^2 v^i v^k \frac{\partial v^k}{\partial t} + \frac{\partial v^i}{\partial t} + \frac{\partial \ln T}{\partial x^i} + \gamma^2 v^k \frac{\partial v^k}{\partial x^i} \right], \end{aligned} \quad (\text{B.19})$$

RHS =

$$\begin{aligned}
&= v^j \gamma v^j \frac{\partial T}{\partial x^i} + v^j T v^j \frac{\partial \gamma}{\partial x^i} + v^j T \gamma \frac{\partial v^j}{\partial x^i} - v^j \gamma v^i \frac{\partial T}{\partial x^j} - v^j T v^i \frac{\partial \gamma}{\partial x^j} - v^j T \gamma \frac{\partial v^i}{\partial x^j} \\
&= \gamma v^2 \frac{\partial T}{\partial x^i} + T \gamma^3 v^2 v^k \frac{\partial v^k}{\partial x^i} + T \gamma v^j \frac{\partial v^j}{\partial x^i} - \gamma v^j v^i \frac{\partial T}{\partial x^j} - T \gamma^3 v^j v^i v^k \frac{\partial v^k}{\partial x^j} - T \gamma v^j \frac{\partial v^i}{\partial x^j} \\
&= T \gamma \left[v^2 \frac{\partial \ln T}{\partial x^i} + \gamma^2 v^2 v^k \frac{\partial v^k}{\partial x^i} + v^k \frac{\partial v^k}{\partial x^i} - v^i v^j \frac{\partial \ln T}{\partial x^j} - \gamma^2 v^i v^j v^k \frac{\partial v^k}{\partial x^j} - v^j \frac{\partial v^i}{\partial x^j} \right].
\end{aligned}$$

By comparing LHS with RHS we get

$$(1 - v^2) \frac{\partial \ln T}{\partial x^i} + v^i \left[\frac{\partial \ln T}{\partial t} + v^j \frac{\partial \ln T}{\partial x^j} \right] + \frac{\partial v^i}{\partial t} + v^j \frac{\partial v^i}{\partial x^j} + \gamma^2 v^i v^k \left[\frac{\partial v^k}{\partial t} + v^j \frac{\partial v^k}{\partial x^j} \right] = 0.$$

The final form of the temperature equations in the Cartesian coordinates is

$$(1 - v^2) \frac{\partial \ln T}{\partial x^i} + v^i \frac{d \ln T}{dt} + \frac{dv^i}{dt} + \gamma^2 v^i v^k \frac{dv^k}{dt} = 0, \quad (\text{B.20})$$

or

$$(1 - v^2) \frac{\partial \ln T}{\partial x} + v_x \frac{d \ln T}{dt} + \frac{dv_x}{dt} + \gamma^2 v_x v \frac{dv}{dt} = 0, \quad (\text{B.21})$$

$$(1 - v^2) \frac{\partial \ln T}{\partial y} + v_y \frac{d \ln T}{dt} + \frac{dv_y}{dt} + \gamma^2 v_y v \frac{dv}{dt} = 0, \quad (\text{B.22})$$

$$(1 - v^2) \frac{\partial \ln T}{\partial z} + v_z \frac{d \ln T}{dt} + \frac{dv_z}{dt} + \gamma^2 v_z v \frac{dv}{dt} = 0. \quad (\text{B.23})$$

For further use it is convenient to consider linear combinations of Eqs. (B.21) - (B.23). At first we multiply Eqs. (B.21) - (B.23) by the appropriate components of the velocity (for example, Eq. (B.21) is multiplied by v_x , etc.) and add them together. The second combination is obtained if we multiply Eq. (B.21) by v_y and subtract Eq. (B.22) multiplied by v_x . As the third independent equation we take the unchanged formula (B.23). In this way one finds

$$(v^2 - 1) \frac{\partial \ln T}{\partial t} + \frac{d \ln T}{dt} + \frac{1}{1 - v^2} v \frac{dv}{dt} = 0, \quad (\text{B.24})$$

$$(1 - v^2) \left(v_y \frac{\partial \ln T}{\partial x} - v_x \frac{\partial \ln T}{\partial y} \right) + v_y \frac{dv_x}{dt} - v_x \frac{dv_y}{dt} = 0, \quad (\text{B.25})$$

$$(1 - v^2) \frac{\partial \ln T}{\partial z} + v_z \frac{d \ln T}{dt} + \frac{dv_z}{dt} + \frac{v_z}{1 - v^2} v \frac{dv}{dt} = 0. \quad (\text{B.26})$$

These equations can be also rewritten in the cylindrical coordinates in the form

$$(v^2 - 1) \frac{\partial \ln T}{\partial t} + \frac{d \ln T}{dt} + \frac{1}{1 - v^2} v \frac{dv}{dt} = 0, \quad (\text{B.27})$$

$$(1 - v^2) \left(v_r \sin \alpha \frac{\partial \ln T}{\partial r} - \frac{v_r \cos \alpha}{r} \frac{\partial \ln T}{\partial \phi} \right) - v_r^2 \left(\frac{d\alpha}{dt} + \frac{v_r \sin \alpha}{r} \right) = 0, \quad (\text{B.28})$$

$$(1 - v^2) \frac{\partial \ln T}{\partial z} + v_z \frac{d \ln T}{dt} + \frac{dv_z}{dt} + \frac{v_z}{1 - v^2} v \frac{dv}{dt} = 0. \quad (\text{B.29})$$

We note that the total derivative in the above equations has the form of Eq. (B.6).

B.4.1 Boost-invariance

For the boost invariant systems the longitudinal velocity has the form $v_z = z/t$. We may insert this form into the hydrodynamic equations, calculate all the necessary derivatives and then set $z = 0$. In this way we obtain the hydrodynamic equations in the plane $z = 0$.

$$(v_r^2 - 1) \frac{\partial \ln T}{\partial t} + \frac{d \ln T}{dt} + \frac{1}{1 - v_r^2} v_r \frac{dv_r}{dt} = 0, \quad (\text{B.30})$$

$$(1 - v_r^2) \left(v_y \frac{\partial \ln T}{\partial x} - v_x \frac{\partial \ln T}{\partial y} \right) + v_y \frac{dv_x}{dt} - v_x \frac{dv_y}{dt} = 0. \quad (\text{B.31})$$

Again we can make use of the cylindrical coordinates to get

$$(v_r^2 - 1) \frac{\partial \ln T}{\partial t} + \frac{d \ln T}{dt} + \frac{1}{1 - v^2} v \frac{dv}{dt} = 0, \quad (\text{B.32})$$

$$(1 - v_r^2) \left(v_r \sin \alpha \frac{\partial \ln T}{\partial r} - \frac{v_r \cos \alpha}{r} \frac{\partial \ln T}{\partial \phi} \right) - v_r^2 \left(\frac{d\alpha}{dt} + \frac{v_r \sin \alpha}{r} \right) = 0. \quad (\text{B.33})$$

The total derivatives for the boost-invariant systems are reduced at $z = 0$ to the expressions

$$\frac{d}{dt} = \frac{\partial}{\partial t} + v_x \frac{\partial}{\partial x} + v_y \frac{\partial}{\partial y} \quad (\text{Cartesian}), \quad (\text{B.34})$$

$$\frac{d}{dt} = \frac{\partial}{\partial t} + v_r \cos \alpha \frac{\partial}{\partial r} + \frac{v_r \sin \alpha}{r} \frac{\partial}{\partial \phi} \quad (\text{cylindrical}). \quad (\text{B.35})$$

B.4.2 Cylindrical symmetry

In certain physical situations the system described by the relativistic hydrodynamics has cylindrical symmetry. In this case the hydrodynamic equations are reduced to the form

$$(v^2 - 1) \frac{\partial \ln T}{\partial t} + \frac{d \ln T}{dt} + \frac{1}{1 - v^2} v \frac{dv}{dt} = 0, \quad (\text{B.36})$$

$$(1 - v^2) \frac{\partial \ln T}{\partial z} + v_z \frac{d \ln T}{dt} + \frac{dv_z}{dt} + \frac{v_z}{1 - v^2} v \frac{dv}{dt} = 0. \quad (\text{B.37})$$

These equations have the same form in cylindrical coordinates. Combining both the boost-invariance and cylindrical symmetry gives us only one independent equation

$$v_r \frac{\partial \ln T}{\partial t} + \frac{\partial \ln T}{\partial r} + \frac{1}{1 - v_r^2} \frac{\partial v_r}{\partial t} + \frac{v_r}{1 - v_r^2} \frac{\partial v_r}{\partial r} = 0. \quad (\text{B.38})$$

B.5 Entropy equation

In this Section we discuss the entropy conservation law, Eq. (B.17). Following the same steps as in the previous Section we obtain

$$\begin{aligned} \gamma \frac{\partial s}{\partial t} + s \frac{\partial \gamma}{\partial t} + \gamma v^i \frac{\partial s}{\partial x^i} + s v^i \frac{\partial \gamma}{\partial x^i} + s \gamma \frac{\partial v^i}{\partial x^i} &= 0, \\ \gamma s \left[\frac{\partial \ln s}{\partial t} + v^i \frac{\partial \ln s}{\partial x^i} + \gamma^2 v^k \left(\frac{\partial v^k}{\partial t} + v^i \frac{\partial v^k}{\partial x^i} \right) + \frac{\partial v^i}{\partial x^i} \right] &= 0. \end{aligned}$$

The final form of the entropy equation has the form

$$\frac{d \ln s}{dt} + \frac{v}{1 - v^2} \frac{dv}{dt} + \frac{\partial v^i}{\partial x^i} = 0, \quad (\text{B.39})$$

which in the Cartesian and cylindrical coordinates has the form

$$\frac{d \ln s}{dt} + \frac{v}{1 - v^2} \frac{dv}{dt} + \frac{\partial v_x}{\partial x} + \frac{\partial v_y}{\partial y} + \frac{\partial v_z}{\partial z} = 0, \quad (\text{B.40})$$

and

$$\begin{aligned} \frac{d \ln s}{dt} + \frac{v}{1 - v^2} \frac{dv}{dt} + \cos \alpha \frac{\partial v_r}{\partial r} + \frac{\sin \alpha}{r} \frac{\partial v_r}{\partial \phi} \\ - v_r \sin \alpha \frac{\partial \alpha}{\partial r} + \frac{v_r \cos \alpha}{r} \left(\frac{\partial \alpha}{\partial \phi} + 1 \right) + \frac{\partial v_z}{\partial z} = 0. \end{aligned} \quad (\text{B.41})$$

B.5.1 Boost-invariance

The z component of velocity equals $v_z = z/t$, hence its derivative with the respect to that coordinate gives a term $\frac{1}{t}$. With this remark in mind we perform the rest of the calculations at $z = 0$ and find

$$\frac{d \ln s}{dt} + \frac{v_r}{1 - v_r^2} \frac{dv_r}{dt} + \frac{\partial v_x}{\partial x} + \frac{\partial v_y}{\partial y} + \frac{1}{t} = 0, \quad (\text{B.42})$$

or

$$v_r \frac{d \ln s}{dt} + \frac{1}{1 - v_r^2} \frac{dv_r}{dt} - \frac{\partial v_r}{\partial t} - v_r^2 \sin \alpha \frac{\partial \alpha}{\partial r} + \frac{v_r^2 \cos \alpha}{r} \left(\frac{\partial \alpha}{\partial \phi} + 1 \right) + \frac{v_r}{t} = 0. \quad (\text{B.43})$$

B.5.2 Cylindrical symmetry

For cylindrically symmetric systems entropy density and transverse velocities are independent of direction in transverse plane. The entropy equation with cylindrical symmetry has the form

$$\frac{d \ln s}{dt} + \frac{v_r}{1 - v_r^2} \frac{\partial v_r}{\partial t} + \frac{1}{1 - v_r^2} \frac{\partial v_r}{\partial r} + \frac{v_r}{r} + \frac{\partial v_z}{\partial z} = 0. \quad (\text{B.44})$$

where we have used the definition for the transverse velocity divergence

$$\frac{\partial v_x}{\partial x} + \frac{\partial v_y}{\partial y} = \frac{\partial v_r}{\partial r} + \frac{v_r}{r}. \quad (\text{B.45})$$

When both the boost-invariance and cylindrical symmetry is applied to the entropy equation we get

$$\frac{\partial \ln s}{\partial t} + v_r \frac{\partial \ln s}{\partial r} + \frac{v_r}{1 - v_r^2} \frac{\partial v_r}{\partial t} + \frac{1}{1 - v_r^2} \frac{\partial v_r}{\partial r} + \frac{v_r}{r} + \frac{1}{t} = 0. \quad (\text{B.46})$$

Appendix C

Notation

In this Appendix we collect the symbols used in the Thesis.

Thermodynamics

Ω	grand canonical potential,
Z or z	grand canonical partition function,
T	temperature,
V	volume,
E	energy,
$\varepsilon = \frac{E}{V}$	energy density,
S	entropy,
$s = \frac{S}{V}$	entropy density,
P	pressure,
N	particle number,
μ	chemical potential,
μ_B	baryon chemical potential,
μ_S	strange chemical potential,
μ_{I_3}	isospin chemical potential,
ϵ	statistics identifier (+1 for FD, -1 for BE),
g	degeneration factor,
c_s	sound velocity,
T_c	critical temperature,
m_π	pion mass.

Hydrodynamics

$T^{\mu\nu}$	energy momentum tensor,
$u^\mu = \gamma(1, \mathbf{v})$	four-velocity,
$\mathbf{v} = (v_x, v_y, v_z)$	velocity,
\mathbf{v}_r	radial velocity,
\mathbf{v}_\perp	transverse velocity,
$\alpha = \tan^{-1}(v_y/v_x) - \phi$	angle between transverse velocity \mathbf{v}_\perp and the radial velocity \mathbf{v}_r ,
$\eta_\perp = \tanh^{-1} v_\perp$	transverse fluid rapidity,
$\gamma = (1 - v^2)^{-\frac{1}{2}}$	Lorentz factor,
j_B^μ	baryon four-current,
τ	proper time,
Φ	thermodynamic potential used in the Baym formalism,
A_+, A_-, A	auxiliary functions used in the Baym formalism.

Initial conditions for hydrodynamics

ρ	nuclear profile,
ρ_0, r_0, a	parameters for Woods-Saxon nuclear profile,
ρ_{WN}	wounded nucleon profile,
ρ_{BC}	binary collisions profile,
T_A	thickness function,
σ_{in}	total inelastic pp cross-section,
$\sigma_{\text{in}}^{\text{AuAu}}$	total inelastic cross-section in Au Au,
κ	mixing factor between WN and BC nuclear profiles,
\mathbf{b}	impact vector,
τ_i	initial proper time,
s_i	initial entropy density at $r = 0$,
ε_i	initial energy density at $r = 0$,
T_i	initial temperature at $r = 0$,
H_0	initial Hubble flow.

Freeze-out

ϕ	spatial azimuthal angle,
ζ	angle in the $\tau - \rho$ plane,
$\eta_\parallel = \frac{1}{2} \ln \frac{t+z}{t-z}$	spacetime rapidity,
$d(\phi, \zeta)$	distance from the point $(\tau = \tau_i, x = 0, y = 0)$ to the hypersurface point with coordinates (ϕ, ζ) ,
\mathbf{v}_\perp	transverse velocity on the hypersurface,
α	angle between v_\perp and v_r on the hypersurface,
p_T or p_\perp	particle's transverse momentum,
ϕ_p	particle's azimuthal transverse momentum angle,
y	particle's rapidity,
m	particle's mass,
$d\Sigma$	three-dimensional element of the hypersurface.

Appendix D

Mathematical supplement

D.1 Modified Bessel functions

The second-order ordinary differential equation

$$z^2 \frac{d^2 w(z)}{dz^2} + z \frac{dw(z)}{dz} - (z^2 + \nu^2) w(z) = 0 \quad (\text{D.1})$$

has a solution in form of the modified Bessel function of the first kind $I_\nu(z)$ and second kind $K_\nu(z)$

$$w(z) = c_1 I_\nu(z) + c_2 K_\nu(z). \quad (\text{D.2})$$

Modified Bessel function $K_\nu(z)$ has a simple integral representations through the exponential function and power functions in the integrand

$$K_n(z) = \frac{\sqrt{\pi} z^\nu}{2^\nu \Gamma(\nu + \frac{1}{2})} \int_1^\infty e^{-zt} (t^2 - 1)^{\nu - \frac{1}{2}} dt; \quad \text{Re}(\nu) > -\frac{1}{2} \wedge \text{Re}(z) > 0. \quad (\text{D.3})$$

The Bessel function $K_\nu(z)$ satisfies the following recurrence identities

$$\begin{aligned} K_\nu(z) &= K_{\nu+2}(z) - \frac{2(\nu+1)}{z} K_{\nu+1}(z), \\ K_\nu(z) &= K_{\nu-2}(z) + \frac{2(\nu-1)}{z} K_{\nu-1}(z). \end{aligned} \quad (\text{D.4})$$

The derivative of the Bessel function $K_\nu(z)$ has a rather simple and symmetrical representation that can be expressed through other Bessel $K_\nu(z)$ functions with different indices

$$\frac{\partial K_\nu(z)}{\partial z} = -\frac{1}{2} (K_{\nu-1}(z) + K_{\nu+1}(z)), \quad (\text{D.5})$$

this derivative can also be represented in other form

$$\frac{\partial K_\nu(z)}{\partial z} = -K_{\nu-1}(z) - \frac{\nu}{z} K_\nu(z) = \frac{\nu}{z} K_\nu(z) - K_{\nu+1}(z). \quad (\text{D.6})$$

Series representations of the modified Bessel function $K_\nu(z)$ about the point $z = 0$ is very complex. We will limit ourselves to those series expansions useful in our calculations

$$\begin{aligned}
K_1(z) &= \frac{1}{z} + O(z^1), \\
K_2(z) &= \frac{2}{z^2} - \frac{1}{2} + O(z^2), \\
K_3(z) &= \frac{8}{z^3} - \frac{1}{z} + \frac{z}{8} + O(z^3), \\
K_4(z) &= \frac{48}{z^4} - \frac{4}{z^2} + \frac{1}{4} - \frac{z^2}{48} + O(z^4)
\end{aligned} \tag{D.7}$$

The asymptotic expansion of the modified Bessel function $K_\nu(z)$ about $z \rightarrow \infty$ has the form

$$K_\nu(z) = e^{-z} \left(\sqrt{\frac{\pi}{2}} z^{-\frac{1}{2}} + O\left(z^{-\frac{3}{2}}\right) \right) \tag{D.8}$$

Bibliography

- [1] P. F. Kolb, J. Sollfrank, and U. W. Heinz, “Elliptic and hexadecupole flow from AGS to LHC energies,” *Phys. Lett.* **B459** (1999) 667–673, [arXiv:nucl-th/9906003](#).
- [2] D. Teaney and E. V. Shuryak, “An unusual space-time evolution for heavy ion collisions at high energies due to the QCD phase transition,” *Phys. Rev. Lett.* **83** (1999) 4951–4954, [arXiv:nucl-th/9904006](#).
- [3] P. F. Kolb, J. Sollfrank, and U. W. Heinz, “Anisotropic transverse flow and the quark-hadron phase transition,” *Phys. Rev.* **C62** (2000) 054909, [arXiv:hep-ph/0006129](#).
- [4] D. Teaney, J. Lauret, and E. V. Shuryak, “Flow at the SPS and RHIC as a quark gluon plasma signature,” *Phys. Rev. Lett.* **86** (2001) 4783–4786, [arXiv:nucl-th/0011058](#).
- [5] P. F. Kolb, P. Huovinen, U. W. Heinz, and H. Heiselberg, “Elliptic flow at SPS and RHIC: From kinetic transport to hydrodynamics,” *Phys. Lett.* **B500** (2001) 232–240, [arXiv:hep-ph/0012137](#).
- [6] P. Huovinen, P. F. Kolb, U. W. Heinz, P. V. Ruuskanen, and S. A. Voloshin, “Radial and elliptic flow at RHIC: further predictions,” *Phys. Lett.* **B503** (2001) 58–64, [arXiv:hep-ph/0101136](#).
- [7] P. F. Kolb, U. W. Heinz, P. Huovinen, K. J. Eskola, and K. Tuominen, “Centrality dependence of multiplicity, transverse energy, and elliptic flow from hydrodynamics,” *Nucl. Phys.* **A696** (2001) 197–215, [arXiv:hep-ph/0103234](#).
- [8] D. Teaney, J. Lauret, and E. V. Shuryak, “Hydro + Cascade, flow, the equation of state, predictions and data,” *Nucl. Phys.* **A698** (2002) 479–482, [arXiv:nucl-th/0104041](#).
- [9] D. Teaney, J. Lauret, and E. V. Shuryak, “A hydrodynamic description of heavy ion collisions at the SPS and RHIC,” [arXiv:nucl-th/0110037](#).
- [10] U. W. Heinz and P. F. Kolb, “Early thermalization at RHIC,” *Nucl. Phys.* **A702** (2002) 269–280, [arXiv:hep-ph/0111075](#).

- [11] U. W. Heinz and P. F. Kolb, “Emission angle dependent pion interferometry at RHIC and beyond,” *Phys. Lett.* **B542** (2002) 216–222, [arXiv:hep-ph/0206278](#).
- [12] P. F. Kolb and U. W. Heinz, “Emission angle dependent HBT at RHIC and beyond,” *Nucl. Phys.* **A715** (2003) 653–656, [arXiv:nucl-th/0208047](#).
- [13] P. F. Kolb and R. Rapp, “Transverse flow and hadro-chemistry in Au + Au collisions at $\sqrt{s_{NN}} = 200$ GeV,” *Phys. Rev.* **C67** (2003) 044903, [arXiv:hep-ph/0210222](#).
- [14] P. F. Kolb, “Expansion rates at RHIC,” *Heavy Ion Phys.* **21** (2004) 243–248, [arXiv:nucl-th/0304036](#).
- [15] P. F. Kolb and U. W. Heinz, “Hydrodynamic description of ultrarelativistic heavy-ion collisions,” [arXiv:nucl-th/0305084](#).
- [16] C. Nonaka, E. Honda, and S. Muroya, “(3+1)-dimensional relativistic hydrodynamical expansion of hot and dense matter in ultra-relativistic nuclear collision,” *Eur. Phys. J.* **C17** (2000) 663–673, [arXiv:hep-ph/0007187](#).
- [17] T. Hirano, “Is early thermalization achieved only near midrapidity in Au + Au collisions at $\sqrt{s_{NN}} = 130$ GeV?,” *Phys. Rev.* **C65** (2002) 011901, [arXiv:nucl-th/0108004](#).
- [18] T. Hirano, K. Morita, S. Muroya, and C. Nonaka, “Hydrodynamical analysis of hadronic spectra in the 130- GeV/nucleon Au + Au collisions,” *Phys. Rev.* **C65** (2002) 061902, [arXiv:nucl-th/0110009](#).
- [19] K. Morita, S. Muroya, C. Nonaka, and T. Hirano, “Comparison of space-time evolutions of hot/dense matter in $\sqrt{s_{NN}} = 17$ GeV and 130 GeV relativistic heavy ion collisions based on a hydrodynamical model,” *Phys. Rev.* **C66** (2002) 054904, [arXiv:nucl-th/0205040](#).
- [20] T. Hirano and K. Tsuda, “Collective flow and two pion correlations from a relativistic hydrodynamic model with early chemical freeze out,” *Phys. Rev.* **C66** (2002) 054905, [arXiv:nucl-th/0205043](#).
- [21] C. Nonaka and M. Asakawa, “Hydrodynamical evolution near the QCD critical end point,” *Phys. Rev.* **C71** (2005) 044904, [arXiv:nucl-th/0410078](#).
- [22] T. Hirano, U. W. Heinz, D. Kharzeev, R. Lacey, and Y. Nara, “Hadronic dissipative effects on elliptic flow in ultrarelativistic heavy-ion collisions,” *Phys. Lett.* **B636** (2006) 299–304, [arXiv:nucl-th/0511046](#).
- [23] C. Nonaka and S. A. Bass, “Space-time evolution of bulk QCD matter,” *Phys. Rev.* **C75** (2007) 014902, [arXiv:nucl-th/0607018](#).

- [24] P. Bozek and I. Wyskiel, “Rapid hydrodynamic expansion in relativistic heavy-ion collisions,” [arXiv:0902.4121 \[nucl-th\]](#).
- [25] U. W. Heinz, “Early collective expansion: Relativistic hydrodynamics and the transport properties of QCD matter,” [arXiv:0901.4355 \[nucl-th\]](#).
- [26] E. Shuryak, “A strongly coupled quark-gluon plasma,” *J. Phys.* **G30** (2004) S1221–S1224.
- [27] A. Kisiel, T. Taluc, W. Broniowski, and W. Florkowski, “THERMINATOR: Thermal heavy-ion generator,” *Comput. Phys. Commun.* **174** (2006) 669–687, [arXiv:nucl-th/0504047](#).
- [28] W. Florkowski, W. Broniowski, and M. Michalec, “Thermal analysis of particle ratios and p(T) spectra at RHIC,” *Acta Phys. Polon.* **B33** (2002) 761–769, [arXiv:nucl-th/0106009](#).
- [29] P. Braun-Munzinger, D. Magestro, K. Redlich, and J. Stachel, “Hadron production in Au Au collisions at RHIC,” *Phys. Lett.* **B518** (2001) 41–46, [arXiv:hep-ph/0105229](#).
- [30] A. Baran, W. Broniowski, and W. Florkowski, “Description of the particle ratios and transverse-momentum spectra for various centralities at RHIC in a single- freeze-out model,” *Acta Phys. Polon.* **B35** (2004) 779–798, [arXiv:nucl-th/0305075](#).
- [31] J. Cleymans, B. Kampfer, M. Kaneta, S. Wheaton, and N. Xu, “Centrality dependence of thermal parameters deduced from hadron multiplicities in Au + Au collisions at $\sqrt{s_{NN}} = 130$ GeV,” *Phys. Rev.* **C71** (2005) 054901, [arXiv:hep-ph/0409071](#).
- [32] B. Biedron and W. Broniowski, “Rapidity-dependent spectra from a single-freeze-out model of relativistic heavy-ion collisions,” *Phys. Rev.* **C75** (2007) 054905, [arXiv:nucl-th/0610083](#).
- [33] A. Andronic, P. Braun-Munzinger, and J. Stachel, “Hadron production in central nucleus nucleus collisions at chemical freeze-out,” *Nucl. Phys.* **A772** (2006) 167–199, [arXiv:nucl-th/0511071](#).
- [34] M. Chojnacki, W. Florkowski, and T. Csorgo, “On the formation of Hubble flow in Little Bangs,” *Phys. Rev.* **C71** (2005) 044902, [arXiv:nucl-th/0410036](#).
- [35] Y. Aoki, Z. Fodor, S. D. Katz, and K. K. Szabo, “The equation of state in lattice QCD: With physical quark masses towards the continuum limit,” *JHEP* **01** (2006) 089, [arXiv:hep-lat/0510084](#).

- [36] M. Chojnacki and W. Florkowski, “Temperature dependence of sound velocity and hydrodynamics of ultra-relativistic heavy-ion collisions,” *Acta Phys. Polon.* **B38** (2007) 3249–3262, [arXiv:nucl-th/0702030](#).
- [37] P. Huovinen, “Anisotropy of flow and the order of phase transition in relativistic heavy ion collisions,” *Nucl. Phys.* **A761** (2005) 296–312, [arXiv:nucl-th/0505036](#).
- [38] L. D. Landau and E. M. Lifshitz, “Statistical physics, part 1,” (Butterworth-Heinemann, Oxford, 2001).
- [39] L. P. Csernai, “Introduction to relativistic heavy ion collisions,” Chichester, UK: Wiley (1994) 310 p.
- [40] M. Michalec, “Thermal description of particle production in ultra-relativistic heavy-ion collisions,” [arXiv:nucl-th/0112044](#).
- [41] G. Torrieri *et al.*, “SHARE: Statistical hadronization with resonances,” *Comput. Phys. Commun.* **167** (2005) 229–251, [arXiv:nucl-th/0404083](#).
- [42] T. S. Biro and J. Zimanyi, “Entropy of expanding QCD matter,” *Phys. Lett.* **B650** (2007) 193–196, [arXiv:hep-ph/0607079](#).
- [43] W. Broniowski, “Distinct Hagedorn temperatures from particle spectra: A higher one for mesons, a lower one for baryons,” [arXiv:hep-ph/0008112](#).
- [44] M. Chojnacki, W. Florkowski, W. Broniowski, and A. Kisiel, “Soft heavy-ion physics from hydrodynamics with statistical hadronization: Predictions for collisions at $\sqrt{s_{NN}} = 5.5$ TeV,” *Phys. Rev.* **C78** (2008) 014905, [arXiv:0712.0947 \[nucl-th\]](#).
- [45] G. Baym, B. L. Friman, J. P. Blaizot, M. Soyeur, and W. Czyz, “Hydrodynamics of ultrarelativistic heavy ion collisions,” *Nucl. Phys.* **A407** (1983) 541–570.
- [46] **BRAHMS** Collaboration, I. G. Bearden *et al.*, “Charged meson rapidity distributions in central Au + Au collisions at $\sqrt{s_{NN}} = 200$ GeV,” *Phys. Rev. Lett.* **94** (2005) 162301, [arXiv:nucl-ex/0403050](#).
- [47] J. D. Bjorken, “Highly relativistic nucleus-nucleus collisions: The central rapidity region,” *Phys. Rev.* **D27** (1983) 140–151.
- [48] A. Dyrek and W. Florkowski, “Boost invariant motion of relativistic perfect fluid,” *Acta Phys. Polon.* **B15** (1984) 653–666.
- [49] **PHOBOS** Collaboration, B. B. Back *et al.*, “Centrality dependence of charged particle multiplicity at mid-rapidity in Au + Au collisions at $\sqrt{s_{NN}} = 130$ GeV,” *Phys. Rev.* **C65** (2002) 031901, [arXiv:nucl-ex/0105011](#).

- [50] **PHOBOS** Collaboration, B. B. Back *et al.*, “Collision geometry scaling of Au + Au pseudorapidity density from $\sqrt{s_{NN}} = 19.6$ GeV to 200 GeV,” *Phys. Rev.* **C70** (2004) 021902, [arXiv:nuc1-ex/0405027](#).
- [51] A. Bialas, M. Bleszynski, and W. Czyz, “Multiplicity distributions in nucleus-nucleus collisions at high-energies,” *Nucl. Phys.* **B111** (1976) 461.
- [52] M. L. Miller, K. Reygers, S. J. Sanders, and P. Steinberg, “Glauber modeling in high energy nuclear collisions,” *Ann. Rev. Nucl. Part. Sci.* **57** (2007) 205–243, [arXiv:nuc1-ex/0701025](#).
- [53] C. E. Aguiar, T. Kodama, T. Osada, and Y. Hama, “Smoothed particle hydrodynamics for relativistic heavy ion collisions,” *J. Phys.* **G27** (2001) 75–94, [arXiv:hep-ph/0006239](#).
- [54] C. E. Aguiar, Y. Hama, T. Kodama, and T. Osada, “Event-by-event fluctuations in hydrodynamical description of heavy-ion collisions,” *Nucl. Phys.* **A698** (2002) 639–642, [arXiv:hep-ph/0106266](#).
- [55] S. A. Voloshin, “Toward the energy and the system size dependence of elliptic flow: working on flow fluctuations,” [arXiv:nuc1-th/0606022](#).
- [56] W. Broniowski, P. Bozek, and M. Rybczynski, “Fluctuating initial conditions in heavy-ion collisions from the Glauber approach,” *Phys. Rev.* **C76** (2007) 054905, [arXiv:0706.4266 \[nuc1-th\]](#).
- [57] W. Broniowski, M. Rybczynski, and P. Bozek, “GLISSANDO: GLauber Initial-State Simulation AND mOre,” *Comput. Phys. Commun.* **180** (2009) 69–83, [arXiv:0710.5731 \[nuc1-th\]](#).
- [58] S. A. Voloshin, A. M. Poskanzer, A. Tang, and G. Wang, “Elliptic flow in the Gaussian model of eccentricity fluctuations,” *Phys. Lett.* **B659** (2008) 537–541, [arXiv:0708.0800 \[nuc1-th\]](#).
- [59] B. Alver *et al.*, “Importance of Correlations and Fluctuations on the Initial Source Eccentricity in High-Energy Nucleus-Nucleus Collisions,” *Phys. Rev.* **C77** (2008) 014906, [arXiv:0711.3724 \[nuc1-ex\]](#).
- [60] L. D. McLerran and R. Venugopalan, “Gluon distribution functions for very large nuclei at small transverse momentum,” *Phys. Rev.* **D49** (1994) 3352–3355, [arXiv:hep-ph/9311205](#).
- [61] L. D. McLerran and R. Venugopalan, “Computing quark and gluon distribution functions for very large nuclei,” *Phys. Rev.* **D49** (1994) 2233–2241, [arXiv:hep-ph/9309289](#).
- [62] Y. M. Sinyukov, “Matter evolution and soft physics in A + A collisions,” *Acta Phys. Polon.* **B37** (2006) 3343–3370.

- [63] M. Gyulassy, Y. M. Sinyukov, I. Karpenko, and A. V. Nazarenko, “HBT and initial conditions for hydrodynamic expansion in A + A collisions,” *Braz. J. Phys.* **37** (2007) 1031–1038.
- [64] W. Broniowski and W. Florkowski, “Explanation of the RHIC p_T -spectra in a thermal model with expansion,” *Phys. Rev. Lett.* **87** (2001) 272302, [arXiv:nucl-th/0106050](#).
- [65] W. Broniowski and W. Florkowski, “Strange particle production at RHIC in a single-freeze-out model,” *Phys. Rev.* **C65** (2002) 064905, [arXiv:nucl-th/0112043](#).
- [66] W. Broniowski, A. Baran, and W. Florkowski, “Thermal approach to RHIC,” *Acta Phys. Polon.* **B33** (2002) 4235–4258, [arXiv:hep-ph/0209286](#).
- [67] D. Prorok, “Thermal freeze-out versus chemical freeze-out revised,” [arXiv:nucl-th/0702042](#).
- [68] D. Prorok, “The statistical hadronization model approach to $\sqrt{s_{NN}} = 200$ GeV Au-Au collisions: p_T -spectra fits and global variable predictions,” *Phys. Rev.* **C75** (2007) 014903, [arXiv:nucl-th/0609041](#).
- [69] F. Cooper and G. Frye, “Comment on the single particle distribution in the hydrodynamic and statistical thermodynamic models of multiparticle production,” *Phys. Rev.* **D10** (1974) 186.
- [70] F. Cooper, G. Frye, and E. Schonberg, “Electron positron annihilation into hadrons and Landau’s hydrodynamic model,” *Phys. Rev. Lett.* **32** (1974) 862.
- [71] K. A. Bugaev, “Boundary Conditions of the Hydro-Cascade Model and Relativistic Kinetic Equations for Finite Domains,” *Phys. Rev.* **C70** (2004) 034903, [arXiv:nucl-th/0401060](#).
- [72] A. Kisiel, W. Florkowski, and W. Broniowski, “Femtoscopia in hydro-inspired models with resonances,” *Phys. Rev.* **C73** (2006) 064902, [arXiv:nucl-th/0602039](#).
- [73] A. Kisiel, “Non-identical particle femtoscopy in models with single freeze-out,” *Braz. J. Phys.* **37** (2007) 917–924, [arXiv:nucl-th/0612052](#).
- [74] M. G. Bowler, “Coulomb corrections to Bose-Einstein correlations have been greatly exaggerated,” *Phys. Lett.* **B270** (1991) 69–74.
- [75] Y. Sinyukov, R. Lednicky, S. V. Akkelin, J. Pluta, and B. Erazmus, “Coulomb corrections for interferometry analysis of expanding hadron systems,” *Phys. Lett.* **B432** (1998) 248–257.

- [76] **STAR** Collaboration, J. Adams *et al.*, “Pion interferometry in Au + Au collisions at $\sqrt{s_{NN}} = 200$ GeV,” *Phys. Rev.* **C71** (2005) 044906, [arXiv:nucl-ex/0411036](#).
- [77] **PHENIX** Collaboration, S. S. Adler *et al.*, “Identified charged particle spectra and yields in Au + Au collisions at $\sqrt{s_{NN}} = 200$ GeV,” *Phys. Rev.* **C69** (2004) 034909, [arXiv:nucl-ex/0307022](#).
- [78] **PHENIX** Collaboration, S. S. Adler *et al.*, “Elliptic flow of identified hadrons in Au + Au collisions at $\sqrt{s_{NN}} = 200$ GeV,” *Phys. Rev. Lett.* **91** (2003) 182301, [arXiv:nucl-ex/0305013](#).
- [79] W. Broniowski and W. Florkowski, “Geometric relation between centrality and the impact parameter in relativistic heavy ion collisions,” *Phys. Rev.* **C65** (2002) 024905, [arXiv:nucl-th/0110020](#).
- [80] K. J. Eskola, H. Honkanen, H. Niemi, P. V. Ruuskanen, and S. S. Rasanen, “RHIC-tested predictions for low- p_T and high- p_T hadron spectra in nearly central Pb + Pb collisions at the CERN LHC,” *Phys. Rev.* **C72** (2005) 044904, [arXiv:hep-ph/0506049](#).
- [81] J. Rafelski and J. Letessier, “Sudden hadronization in relativistic nuclear collisions,” *Phys. Rev. Lett.* **85** (2000) 4695–4698, [arXiv:hep-ph/0006200](#).
- [82] K. J. Eskola, H. Niemi, and P. V. Ruuskanen, “Dynamical freeze-out condition in ultrarelativistic heavy ion collisions,” *Phys. Rev.* **C77** (2008) 044907, [arXiv:0710.4476 \[hep-ph\]](#).
- [83] N. Armesto *et al.*, “Heavy Ion Collisions at the LHC - Last Call for Predictions,” *J. Phys.* **G35** (2008) 054001, [arXiv:0711.0974 \[hep-ph\]](#).
- [84] D. Kharzeev, E. Levin, and M. Nardi, “The onset of classical QCD dynamics in relativistic heavy ion collisions,” *Phys. Rev.* **C71** (2005) 054903, [arXiv:hep-ph/0111315](#).
- [85] S. Mrowczynski, “Plasma instability at the initial stage of ultrarelativistic heavy ion collisions,” *Phys. Lett.* **B314** (1993) 118–121.
- [86] B. Muller, “From Quark-Gluon Plasma to the Perfect Liquid,” *Acta Phys. Polon.* **B38** (2007) 3705–3730, [arXiv:0710.3366 \[nucl-th\]](#).
- [87] R. Andrade, F. Grassi, Y. Hama, T. Kodama, and J. Socolowski, O., “On the necessity to include event-by-event fluctuations in experimental evaluation of elliptical flow,” *Phys. Rev. Lett.* **97** (2006) 202302, [arXiv:nucl-th/0608067](#).
- [88] Y. Hama *et al.*, “NeXSPheRIO Results on Elliptic-Flow Fluctuations at RHIC,” *Phys. Atom. Nucl.* **71** (2008) 1558–1564, [arXiv:0711.4544 \[hep-ph\]](#).

- [89] E. Schnedermann, J. Sollfrank, and U. W. Heinz, “Thermal phenomenology of hadrons from 200-A/GeV S+S collisions,” *Phys. Rev.* **C48** (1993) 2462–2475, [arXiv:nucl-th/9307020](#).
- [90] K. A. Bugaev, “Shock-like Freeze-out in Relativistic Hydrodynamics,” *Nucl. Phys.* **A606** (1996) 559–567, [arXiv:nucl-th/9906047](#).
- [91] C. Anderlik *et al.*, “Freeze out in hydrodynamical models,” *Phys. Rev.* **C59** (1999) 3309–3316, [arXiv:nucl-th/9806004](#).
- [92] M. S. Borysova, Y. M. Sinyukov, S. V. Akkelin, B. Erazmus, and I. A. Karpenko, “Hydrodynamic source with continuous emission in Au + Au collisions at $\sqrt{s_{NN}} = 200$ -GeV,” *Phys. Rev.* **C73** (2006) 024903, [arXiv:nucl-th/0507057](#).
- [93] S. Pratt, “Resolving the HBT Puzzle in Relativistic Heavy Ion Collision,” [arXiv:0811.3363 \[nucl-th\]](#).